University of Nevada, Reno

Spectroscopic Modeling and Characterization of a Laser-ablated Li-Ag Plasma Plume

A dissertation submitted in partial fulfillment of the
requirements for the degree of Doctor of Philosophy
in Physics.

by

Manolo E. Sherrill

Dr. Roberto C. Mancini, Dissertation Advisor

May 2003

The dissertation of Manolo E. Sherrill is approved:

Dissertation Advisor

Department Chair

Dean, Graduate School

University of Nevada

Reno

May 2003

Abstract

In this dissertation, the modeling and spectroscopic analysis of optical line emission recorded during the laser ablation of plasma plumes from a solid Li-Ag alloy target is discussed. The spectral model considers the effects of multi-element collisional-radiative atomic kinetics, detailed Stark-broadened line profiles, and radiation transport. To compute the atomic data of neutrals and low-charge ions a semi-empirical procedure was implemented in a Hartree-Fock atomic structure code, that produces a set of wavefunctions consistent with measured energy levels. This procedure is critical to obtain spectroscopic quality atomic data for a transition element like silver. A large database of atomic cross sections and rates was computed to input the atomic kinetics calculations. Detailed line shapes were calculated for the Li and Ag line transitions observed in the experimental spectra taking into account the effects of natural, Doppler, Stark and resonance broadening. The radiation transport equation was solved to calculate the transport of the lines through the plasma and the emitted line intensity distribution. The final synthetic spectra self-consistently includes the Li and Ag line emissions. The temperature and density sensitivity of these spectra is discussed for the case of uniform and non-uniform plasmas.

The spectral model was implemented in a versatile and efficient parallel processing code, and applied to the analysis of data recorded in laser ablation experiments performed at Sandia National Laboratories. First, raw data images recorded with a gated, space-resolving spectrograph were corrected for instrument efficiency, and the wavelength and space axes calibrated. Then, a collection of time- and space-resolved spectra lineouts was extracted for analysis. The results of the analysis indicate that early in time and close to the target's surface a dense plasma is formed with electron

temperatures in the 1 eV to 2 eV range, and electron densities in the 1×10^{17} cm^{-3} to 1×10^{18} cm^{-3}. The impact of plasma non-uniformities and opacity on the formation of the spectra close to the surface is discussed. Late in time and away from the surface the spectra are characteristic of a plasma undergoing a time-dependent (i.e. non-steady-state) recombination driven by thermal cooling and fast expansion. These results are important for testing hydrodynamic models of laser ablation and understanding the dynamics of plasma plumes.

Dedication

To my loving family

Acknowledgments

I would like to thank Professor Roberto C. Mancini, my advisor, for his patience, guidance and encouragement throughout my education, and I would like to acknowledge the useful suggestions and efforts by my dissertation committee members: Drs. F. Harris Jr., V. Kwong, R. Phaneuf and P. Winkler. I would also like to thank Drs. J. Bailey and T. Melhorn (Sandia National Laboratories, SNL) for providing the experimental data, VIDA software and training needed to prepare the data for analysis; J. Abdallah Jr. and Dr. R. Cowan (Los Alamos National Laboratory, LANL) for their assistance and guidance in the implementation of the RCE semi-empirical procedure into CATS and for their help with the Los Alamos atomic structure and scattering codes; Dr. D. Phillion (Lawrence Livermore National Laboratory, LLNL) for his efforts in accomodating PDShrink specifically for use with the SNL data; Dr. J.D. Johnson (LANL) for providing customized equations of state used in the analysis of the SNL data; and B. Lucchesi who's conversations inspired the development of the new software scheme developed in this work.

I would also like to extend my thanks to my wife, Barbara; brother, Oscar; mother, Nora and my father Gayle Sherrill for their patience, help and support during this work. I would further like to thank my friends and co-workers in the Physics Department.

Support from the National Science Foundation EPSCoR Chemical Physics program, the US DOE NNSA and NLUF programs, and UCCSN is gratefully acknowledged.

Contents

List of Figures

List of Tables

Chapter 1

Introduction

Laser ablation refers to the process of ablating material from a solid or liquid target, with a low intensity laser ranging from 1×10^{7} W/cm^2 to 1×10^{10} W/cm^2. Typically, a pulsed laser is used to irradiate the target. It deposits the bulk of its energy in the skin depth region of the target where this volume of material is heated and then undergoes melting, evaporation, and possibly plasma formation. The material in the gaseous state then forms a plume that expands away from the target's surface with normal to the surface velocities of a few 10 μm/nsec. When a series of ablation events are performed, where the duration of the irradiation of the target is allowed to stay constant (that is the full width at half maximum (FWHM) of the temporal pulse shape is fixed) while the fluence is allowed to increase, a transition between evaporative plume to plasma plume formation can be observed [1].

Laser ablation is commonly used in both experimental physics as ion sources, and in industry for the generation of thin films. In fact, laser ablation has proven to be the most consistent method of producing high quality thin films, in particular, for stoichiometrically complex material. This technique has been used in the manufactur-

ing of electronic and optical films, super-conductors, ferroelectrics, piezoelectric and photoelectric materials as well as tribological coatings such as diamond like thin films [2]. In the last 4 years, more exotic systems have entered this application arena. Pico- and femto-second lasers have found their place in the thin film synthesis and annealing. A further exotic ablation process is matrix-assisted laser desorption ionization (MALDI), used to place large biomolecules, such as proteins, in a free environment for use in mass-spectroscopy and other studies [3].

From the early to mid 1960's, after the availability of the first ruby lasers, a substantial effort toward the understanding of laser matter interaction from both the theoretical and the experimental perspective was under way. Solid, liquid, and gas targets interactions were all investigated. These investigations lead researchers to think of possible applications; and by 1965, the laser was successfully shown to be a useful tool in producing thin films on a substrate [4]. For the generation of thin films, lasers driven ablation waned.

Laser ablation acquired new interest during the late 1980's for a series of work done on the synthesis, in particular, of high quality stoichiometrically complex high temperature superconductor ($YBa_2Cu_3O_{7-x}$) [5] through the use of pulsed laser deposition. Pulse laser deposition (PLD) produced a greater congruent ablation than other deposition techniques. The shorter pulse durations allowed for the thermalization of a shallower volume of target material. This preserves the stoichiometric properties during the transfer of the material to the subtrate where the thin film is grown. With the accessibility of higher frequency lasers (Nd: YAG 1.06 μm), the target volume accessed directly by the laser energy was also reduced. This added to a greater congruent ablation, as well as a reduced effect of subsurface heating - the main cause of splashing: the ejection of molten globules from the surface of the target.

By 1992, Saenger, K. [2] reported over 180 thin films synthesized with PLD. These materials included metals, inorganic and organic compounds as well as polymer films; and in the last few years, PLD has been used in the development of nano-materials such as the synthesis of carbon nanotubes [6].

Though there has been a large body of experimental work dedicated to the characterization of ablation plumes produced under various experimental parameters and targets, little attention had been paid toward a fundamental understanding of simple systems. This is primarily the outcome of the ablation communities' desire to have information on specific systems for the synthesis of particular materials. It is also recognized that the complexity of even the simplest systems can elude theoretical characterization; due in part, to the myriad of possible plume constituents such as atoms, atomic and molecular ions, clusters, and micron size particles, whose abundances may change with a small change in laser fluence.

Work that has attempted to describe ablation physics, in general, has resided either in the detailed modeling of laser target interactions [7] or the modeling of the expanded plume through gas dynamic simulations [8], [9], [10] or hybrid models [11]. Interestingly, detailed study of the plasma in the region between the target and a few millimeters from the target has not been undertaken [12]; although it is this region of the plasma that defines the level populations and the ionization abundances of the plasma far away and later in time (in the absence of background gases).

This dissertation focuses on the modeling and analysis of a laser ablation plume for the region from tens of microns to a few millimeters away from the target surface and early in time (20-100 nsec after the end of the laser pulse). This work attempts to provide detailed quantitative information of laser ablation in this spatial and tem-

poral regime for a modest stoichometrically complex target. To this end, a series of theoretical and modeling techniques have been developed to deal with specific issues that arise in the modeling of atomic kinetics and line emission formation in multi-component ablation plasmas.

Due to the non-intrusive aspects of emission spectroscopy and the possible sensitivity of line spectra to reveal the state of the plasma, spectroscopic modeling in conjunction with experimental data has been chosen as the technique for this undertaking. We note that in the regime of high temperature plasmas, this technique has been very successful in quantitatively describing the detailed state of plasmas [13].

At the heart of this work is a detailed comparison with experimental data provided by Dr. J. E. Bailey from Sandia National Laboratories (SNL). Based on an innovative technique to reduce plasma gradients in order to simplify the interpretation and spectroscopic analysis, this experiment provided us with time- and spatially-resolved visible spectra for our comparisons. It must be emphasized here that time- and spatially- resolved spectral data for ablated plasmas is extremely rare. These data also provided us with insight and directed us in the design of the physics model needed to construct synthetic spectra appropriate for this regime.

In Chapter 2, the SNL experiment is discussed. This work begins with the processing of the raw data. The calibration of the wavelength, displacement, and efficiency are described. Smoothing is performed to reduce the amount of noise in the data. Further corrections are employed to remove artifacts resulting from scattering within the spectrometer. During the experiment, a virtual image was recorded arising from the reflection of the plasma plume off of the mirror-like Pt surface. The position of the target's surface had to be determined. Three alternative procedures were devised and compared to determine the target surface location. With a final proper

base line for the spectra, the data are processed and spectral lineouts were extracted for the analysis.

In Chapter 3, the difficulties of generating spectroscopic quality data for transition-elements such as Ag are discussed. Various approximations within Cowan's atomic structure code are shown to produce little improvement. The introduction of a semi-empirical procedure and its implementation into the Los Alamos National Laboratory's suite of atomic structure and scattering codes are discussed. In addition, a comparison of the wavefunctions before and after the semi-empirical corrections, their effect on the collision rates, and the pros and cons of numerical procedures for determining rates are also discussed. Finally, comparisons between generic and ab initio calculated rates are shown.

Chapter 4 is dedicated to the formal development of the atomic kinetic models used in this work. Before beginning the discussion of the atomic kinetics, the impracticality of calculating the number of collisional cross sections for Ag II and Ag III in a j-level representation (fine structure) must be overcome. Level representation is needed to simulate the Ag I contributions that are seen in the experimental data. The enormous multiplicity of states that arise from an open d-shell ions and atoms is due to the angular momentum coupling. The solution requires a multi-representational atomic kinetic model. From this point, the single-element collisional-radiative atomic kinetic models needed for the analysis of the experimental data is introduced. Two different models were developed. First, a steady state model was used to analyze the high density spectra close to the target's surface; and secondly, a time dependent model was developed to study the expanded plasma far from the target. Due to the Li-Ag binary alloy used as target, a multi-element atomic kinetic model had to be developed. To properly account for the interplay between Li and Ag in the plasma

environment, the population kinetics of Li and Ag had to be solved self-consistently. In our case, the atomic kinetics of Li and Ag ions are coupled through the common pool of free electrons of the plasma. The interesting interplay between these vastly different elements as a function of plasma temperature is shown.

To generate the number of synthetic spectra needed for the comparison with the experimental data, a parallel spectral model had to be developed. In Chapter 5, the challenges in developing a multi-element atomic kinetic model that has the capabilities of distributed execution across several networked computers are discussed. Modifications to a preexisting single-element atomic kinetic model into a parallel multi-element model produced a code that was, from a practical standpoint, unmanageable. To solve this problem, a new programming methodology robust enough to meet the demands involved in this project had to be developed: This included the production of an efficient parallel implementation, the ability to add and remove physics modules for testing purposes with relative ease, and a standard procedure for implementing modules independent of the overall scale of the model. These software development requirements were similar to those found in the distributed operating systems (DOS) community. Patterned after the work done in DOS, a set of tools was developed to deal with this projects needs and they also appear to have broader applicability to the general scientific research community who deal with large scale simulation projects.

In Chapter 6, the other elements of the synthetic model are discussed. The generation of detailed line profiles and the effects of plasma micro-field mixing of energy levels are shown. Furthermore, the formalism for our radiation transport code, capable of computing high opacity spectra, is developed. With all the synthetic spectral tools in place, a uniform plasma model survey was performed to study various

aspects of the Li-Ag plasma and spectra. In particular, the presence of large opacities and their effects on both the level population atomic kinetics and transport of the line radiation is discussed.

In Chapter 7, the analysis of the experimental data close to the target surface is discussed. Multi-zone spatial profiles were used to approximate the effects of the presence of gradients in the plasma. Comparisons between the model and the data are presented. From this set of comparisons, the effects of boundary and core spatial zones on individual the spectra discussed. For the plasma plume occurring later in time and far away from the target's surface, hydro-simulation results were used to approximate density and temperature time histories. Time-dependent and steady state models computed with the same density and temperature time histories revealed diverging solutions. Two distinct regimes, an ionization phase and a recombination phase, was observed. Spectral evidence of the time-dependent nature of the plume due to cascading populations in the Li I 3d-2p and 2p-2s line features is also discussed.

Chapter 2

Laser Ablation: Experimental Results

2.1 Introduction

A common concern in developing spectroscopy experiments for moderately dense plasmas is the ability to produce homogeneous plasmas with regards to limiting gradients in temperature and density, at least along the line-of-sight of the spectrometer. This desire to reduce inhomogeneities in the plasma stems from the difficulty in analyzing the spectra composed of the convolved contributions of characteristically different emission/absorbtion regions. This chapter describes the configuration, calibration and results of a spectroscopic experiment which includes a technique to reduce plasma inhomogeneities.

2.2 Experimental Design

In a series of experiments performed at Sandia National Laboratories, a binary alloy target composed of 47% Li and 53% Ag was irradiated using a Nd YAG laser with a Gaussian pulse of 10 ns, at an angle of incidence of 30 ° to the target's normal and a

fluence of 0.7 J/cm^2 which corresponds to an intensity of 1×10^8 W/cm^2. Time- and spatially-resolved (along the direction normal to the target's surface) optical spectra in the 4000 – 7000 Å range were recorded with a framing spectrograph. In order to limit the effects of plasma gradients on the spectra due to lateral expansion along a direction perpendicular to the target's normal, a novel target design and instrument was implemented. Several 1.5 mm wide, 0.5 μm thick thin film strips of Li-Ag were coated on top of a 0.2 μm thick Pt coated substrate. The 6×6 mm^2 square focal spot of the laser illuminated both the Li-Ag strip and the surrounding Pt base, as illustrated in Figure 2.1. During the expansion of the metallic plume, the Pt plasma collisionally confined the Li-Ag core thus reducing the Li-Ag lateral expansion as seen in Figure 2.2. This technique represents a variation on the microdot spectroscopy method commonly employed in X-ray spectroscopy of high-temperature laser-produced plasmas [14], and it permitted a more accurate characterization of the Li-Ag plasma plume by reducing plasma gradients along the line-of-sight of the spectrometer. A package of laser-beam smoothing optics, based on a diffuser and homogenizer, was used to improve the laser irradiation uniformity on the target. A gated spectrograph equipped with a f5.6 Nikon lens and a 159 g/mm diffraction grating coupled to a charged coupled device (CCD) was set up to record a time-resolved 1D image along the target normal direction, i.e. a single time snapshot with a 1D spatial image. Each data image is integrated over a 2 ns time interval, and multiple shots with the spectrometer triggered at 10, 20, 30, 40, 50, 75, 100 ns after the end of the laser pulse were recorded to construct the spectral time-history as seen in Figure 2.3. Spatial resolution was approximately 60 μm while the spectral resolution power was 600 ($\lambda/\Delta\lambda$).

As illustrated in Figure 2.3, the horizontal axis of each CCD image represents the

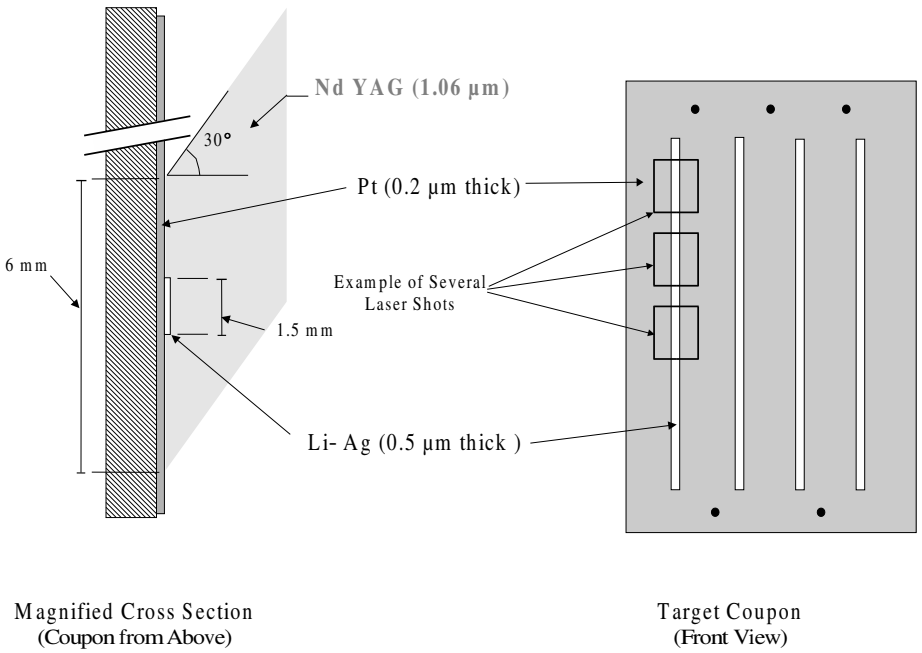

Figure 2.1: Target Design.

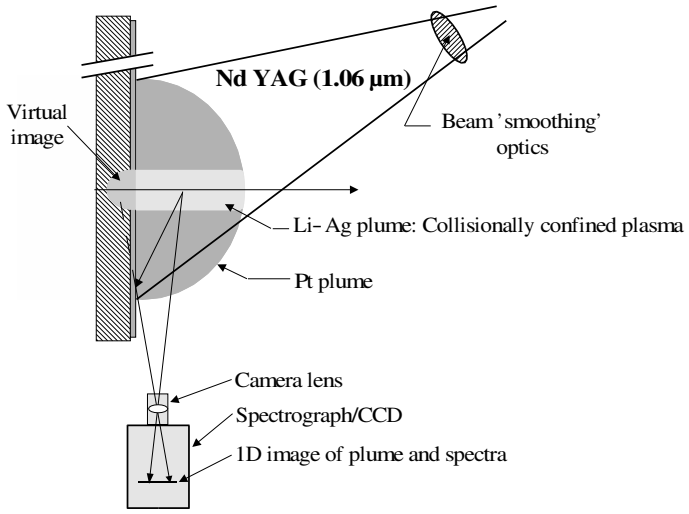

Figure 2.2: Experimental Configuration.

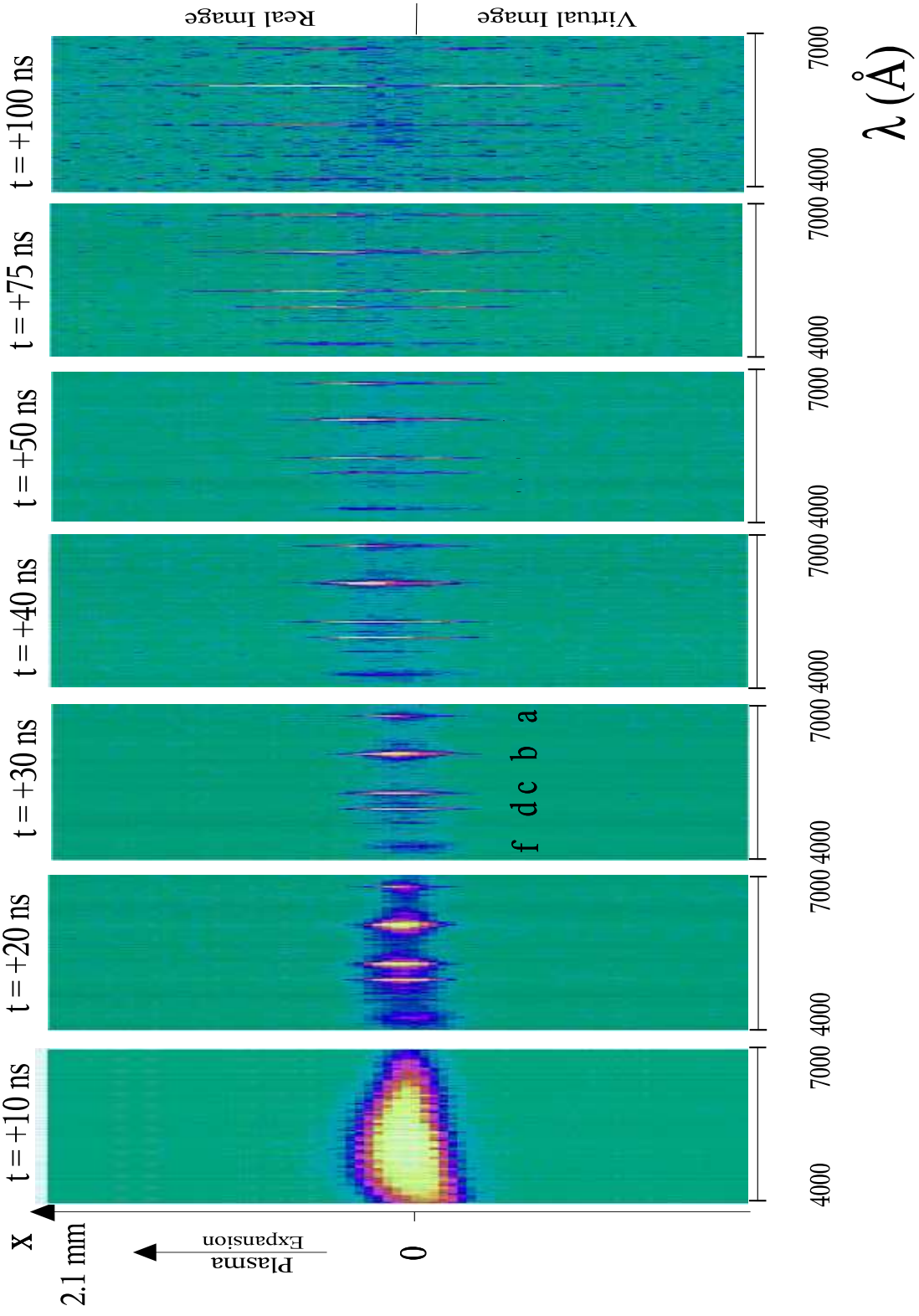

Figure 2.3: Experimental CCD images recorded at 10, 20, 30, 40, 50, 75 and 100 nsec after the end of the laser pulse. Vertical axis represents the spatial expansion of the plasma perpendicular to the target's surface.

wavelength from 4000 – 7000 Å while the vertical axis represents the distance from and normal to the surface of the target from -2100 μm to $+2100$ μm, i.e. $x = 0$ characterizes the location of the target's surface. The instrument records the real as well as the virtual image due to the reflection of the plume emission from the mirror-like surface of the target (See diagram in Figure 2.2). Early in time, only continuum emission is observed. Later, the images display the characteristic line emissions from transitions in Li and Ag atoms. First, the line emissions are localized close to the surface and the lines are broad. This suggests the formation of a dense surface plasma. For later times, the spatial intensity distributions move away from the surface and the lines become narrower. This is a clear indication of the plasma plume expansion.

2.3 Determining the Target Surface Location

Three procedures were used to determine the target surface locations in the CCD images. The surface location was not expected to stay at the same pixel location for each trial since the target coupon had to be moved to provide a clean surface for each consecutive laser shot. Each procedure required spatial lineouts which describe the plasma expansion along a direction normal to the target's surface. These lineouts show both the real and virtual light emission of the expanding plasma as discussed in the section above. Lineouts taken through either continuum or line emission for the early CCD images (i.e. 20, 30 and 40 ns) show that both the virtual and real images are blended into a single feature. In later images, two distinct features are present where the virtual intensity is consistently less than the real intensity. This inequality displays the reflective losses of the platinum target coupon. A specific study comparing the surface estimation by measuring the centroid of lineouts taken

Table 2.1: Target surface location based on the analysis of spatial lineouts of Ag I line at 5465.5 Å.

Time delay (ns)	Image #	Surface pixel
20	22	492.6
30	21	495.5
40	20	NA
50	19	496.9
75	18	498.1
100	17	500.0

through continuum, Table(2.1), and line emission, Table(2.2), revealed that the two early images of 20 and 30 ns were consistent within a pixel value while the later trials of 50, 75 and 100 nsec showed a much greater discrepancy in their determinations. For the 40 nsec trial line-based estimation was not possible: A third deconvolution procedure was developed and compared against previous procedures. This procedure deconvolves the plasma features into two Gaussian contributions. For early images of 20 and 30 ns the procedure was incapable of producing a unique deconvolution of the slightly asymmetric single feature of these lineouts. This technique compared well, however with the centroid line emission estimates within one pixel value. This procedure was also capable to estimating the 40 ns surface location – see Table 2.3.

2.4 Intensity and Spatial Calibration

To calibrate both the intensity and spatial dimension of the imaging spectrograph, a well characterized light source smaller than the spectrograph's field of view had to be created. The end of a 100 μm diameter light emitting fiber-optic line was chosen as

Table 2.2: Target surface location based on analysis of three spatial lineouts through the continuum.

Time delay (ns)	Image #	Continuum region #	Lower bound Å	Upper bound Å	Surface pixel
20	22	1	4687.1	4867.4	491.8
		2	5596.6	5928.9	492.7
		3	6310.3	6562.8	492.0
30	21	1	4688.0	4863.2	494.8
		2	5512.5	6002.0	495.3
		3	6300.9	6651.3	494.9
40	20	1	4646.5	4955.7	496.2
		2	5501.9	6001.7	496.9
		3	6192.4	6651.3	496.4
50	19	1	4630.5	4960.3	498.9
		2	5491.1	6052.8	499.1
		3	6150.7	6681.4	498.6
75	18	1	4634.9	4959.5	499.9
		2	5482.6	6054.6	501.2
		3	6152.5	6631.7	500.9
100	17	1	4623.5	4948.1	502.1
		2	5489.2	6076.6	502.2
		3	6133.3	6679.5	501.9

Table 2.3: Target surface location based on deconvolution of three spatial lineout through emission lines: 1. Ag I: 5207 Å, 2. Ag I: 5465.6 Å and 3. Li I: 6054 Å

Time delay (ns)	Image #	Line Type	Surface pixel
20	22	1	NA
		2	NA
		3	NA
30	21	1	NA
		2	NA
		3	NA
40	20	1	494.5
		2	494.9
		3	494.7
50	19	1	497.3
		2	497.8
		3	497.1
75	18	1	498.9
		2	499.6
		3	499.1
100	17	1	500.8
		2	501.2
		3	500.3

the light source. A bright 500 W Xe arc lamp with collecting optics fed the optical fiber. The goal of the experiment was to record absolute spectra of the plasma. To accomplish this, two separate measurements was needed to characterize this light source.

The first step toward characterization constituted measuring the output of the source with an absolutely calibrated photodiode in conjunction with seven separate 100 Å wide bandpass filters. Though the data recorded from these measurements were absolute, they were of coarse spectral resolution. A second set of relative measurement were performed with a much higher spectral resolution. A NIST traceable lamp was used to calibrate the relative spectral sensitivity of a line spectrograph. Following this calibration, light from the fiberoptic source was then recorded. This output as a function of wavelength would then be scaled with the calibrated photodiode data to produce absolute power as a function of wavelength.

To calibrate the framed spectrograph, including the effect of collection optics, the end of the fiberoptic source was placed at the location where the plasma would be generated. From the gated time images (2-500 nsec) of the fiber source, the CCD pixel to spatial scale factor was determined (57.6 μm/pixel) as well as the total system efficiency which is displayed in Figure 2.4. Later on the data obtained from lineouts taken along the spectral axis of the CCD images would be divided by the total system efficiency. Though a calibrated source was produced and the efficiency of the framing spectrograph was determined, differences still exist between the absolutely experimental spectra and synthetic spectra. These difference can be attributed, in part, to uncertainties in the collection angles.

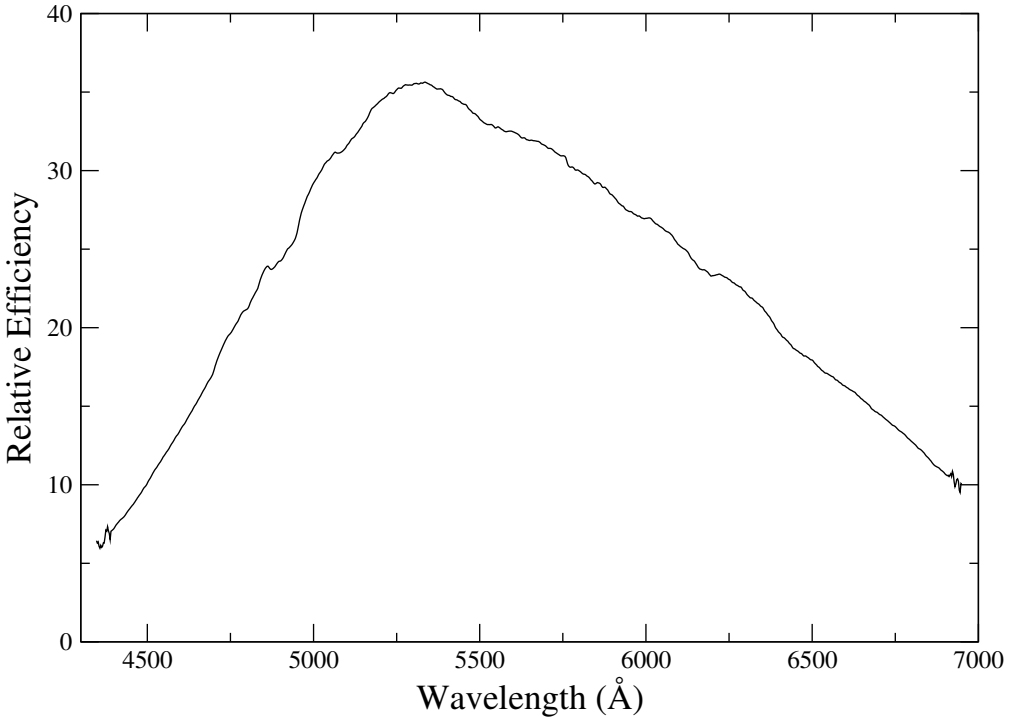

Figure 2.4: Total system efficiency including collection optics and detector.

2.5 Wavelength Calibration

A Ne ORIEL spectral lamp was used in the wavelength calibration of the framing spectrograph. This lamp provided several well defined lines within the region of spectral interest (4000 - 7000 Å). The recorded Ne spectrum lies on a line neither parallel to the x nor the y axis of the CCD image. The Ne spectrum was rotated by $\theta = -0.989^\circ$ such that the data was aligned to the x-axis. This was the first step in the wavelength calibration of the spectrograph. After the rotation, a wavelength to pixel dispersion relation was performed. This was accomplished by measuring the centroids of selected emission lines through horizontal and vertical lineouts. Once the centers of the emission features were obtained, the proper rotation angle could be determined to rotate the CCD image. This rotation would be employed on all other

subsequent data images. After the rotation, line identification was performed with wavelength tables provided by the lamp manufacturer. The vertical and horizontal centroid were again measured for each individual neon line and an ideal fractional pixel value could be associated with the identified wavelengths. The dispersion was obtained by calculating the ratio of the difference of the adjacent wavelengths to pixel values. The mean of the collection of ratios produced the 2.5765 Å/pixel scaling factor needed to calibrate the wavelength axis for all subsequent data images.

2.6 Data Processing

To process the CCD plasma data images, the images were first rotated by $\theta = -0.989\,^{\circ}$ and then the x-axis was scale by a factor of 2.576 Å/pixel to convert from pixel value to wavelength. Both the angle of rotation and the scale factor were obtained during the calibration procedure with the neon lamp. To set the zero value of the wavelength axis, a centroid of the Ag I: $4d^{10}5d(^2D_{5/2})$–$4d^{10}5p(^2P_{3/2})$ parallel to the wavelength axis was measured and the proper shift was employed to place this line at 5465.6Å as described in the literature [15],[16]. With the wavelength axis calibrated, the target surface pixel as determined by the procedure discussed in Section 2.3, is set to zero and the scaling factor of 57.6 μm/pixel is employed in the spatial dimension.

During the experiment, light from the regions of the plasma that is not within the depth of field of the Nikon lens tends to enter and scatter within the spectrograph. This scattered light adds extraneous features in the data. Since the scattering occurs within the spectrograph its effect must be removed before the efficiency function is applied to the CCD images. The emission data occupies a very small region ($< 14\%$) of the entire CCD image. Two lineouts taken above and below the data parallel to

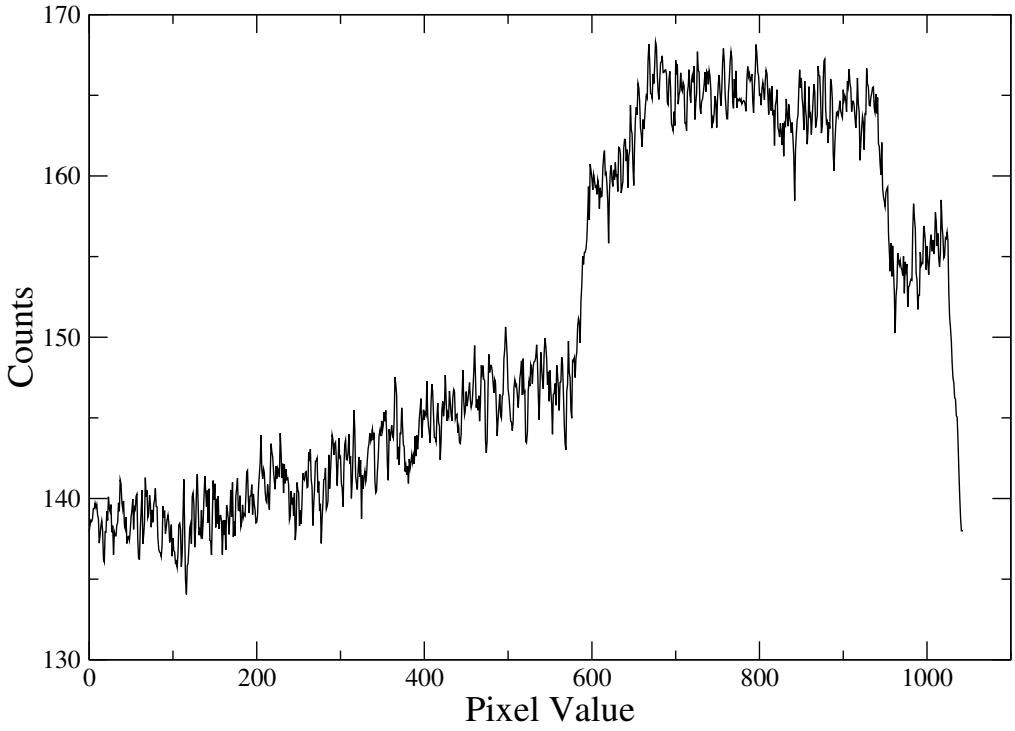

Figure 2.5: Average of lineouts taken above and below spectral data region showing the effects of anomalous scattering within the spectrograph

the wavelength axis are averaged to obtain a representation of this anomalous effect in the region of the data. See Figure 2.5. A polynomial fit taken through this data is then used to subtract off the anomalous contribution to the entire CCD image. The use of a polynomial function prevents the magnification of high frequency noise that would otherwise occur when subtracting the raw data of Figure 2.5.

At this point in the processing of the data, each CCD image is then divided by the efficiency function to correct for the intensity. This correction lead to another problem, however. Due to a lack of precision in the efficiency function the intensity calibration produced a small distortion in the spectrum data. We correct for the distortion when we determine the new baseline for the spectral data. A series of points is taken in close proximity to the spectral baseline. With a parabola capturing

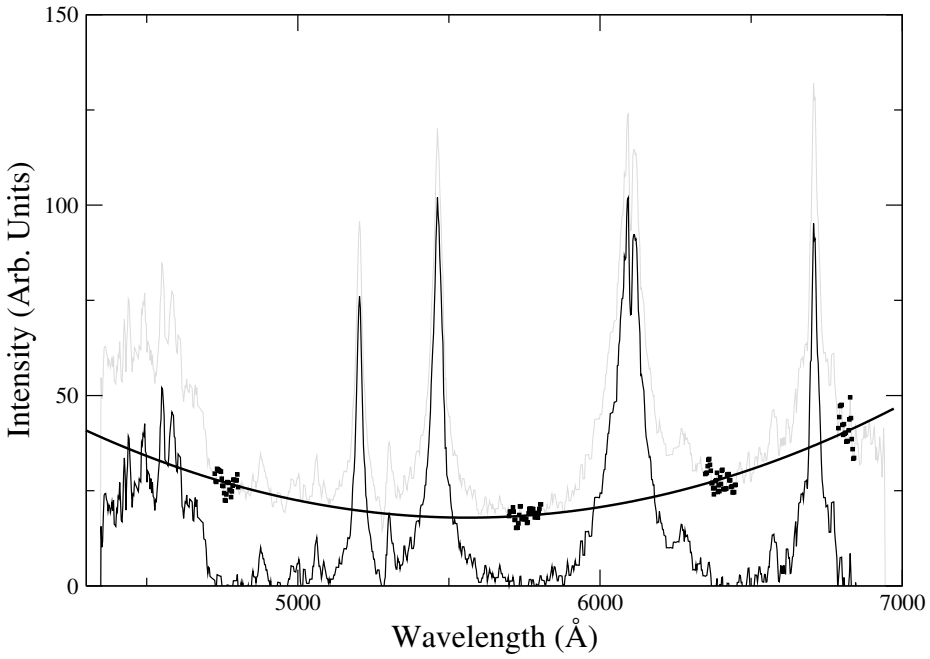

Figure 2.6: A series of selected points for a parabolic least squares minimization determination of a new spectral baseline.

the main behavior of the distortion, a parabolic least squares minimization is used to obtain the new spectral baseline and the final experimental spectra is obtained after subtracting the parabola (see Figure 2.6).

2.7 Time- and Space- Resolved Lineouts

Spatially-resolved spectral lineouts can be extracted from the data images. Early in time and close to the surface (Figure 2.7), lineshapes are broadened by Stark, resonance and opacity broadening (see Table 2.4 for line identification). Furthermore, the Li 3d-2p line feature undergoes a self-reversal due to opacity effects which lends evidence that a slight gradient in the density still exists after collisional confinement by the platinum. In this figure we also see the signal of hydrogen - a contaminant.

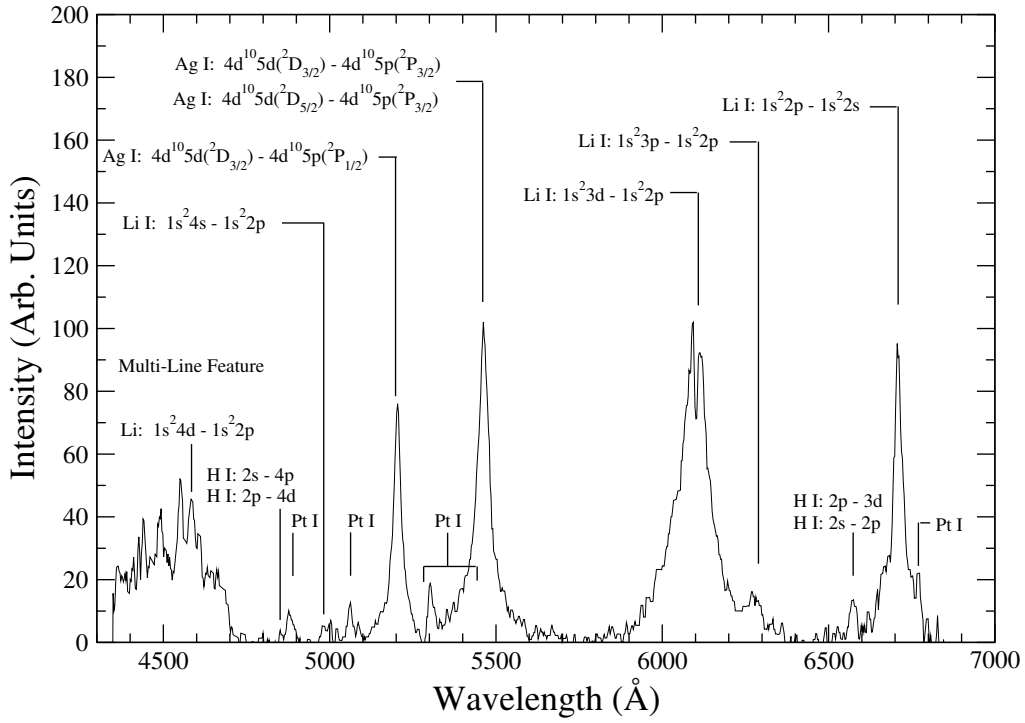

Figure 2.7: Early in time and close to the target surface, this lineout (x=28.8 μm, t=+20 nsec) displays the high density characteristics of Stark broadened line shapes.

Later in time and away form the surface (Figure 2.8), the broadening of the lines does not change, and the line shapes are dominated by the characteristic instrumental function. From the 100 ns spectral lineouts, the average FWHM of the Li I: $1s^2 3d$–$1s^2 2p$ was measured to be 0.00411 eV and this value is used as an estimate of the instrumental resolution function.

Though the non-platinum core of the plasma was imaged, platinum lines are still observed in the Li-Ag spectrum (Figure 2.9). A pure platinum target was irradiated and its spectrum recorded. Since a large number of Pt lines reside in the **f** spectral feature this region does not lend itself for use in diagnosing the state of the core plasma. Also, platinum contributions to both the silver 5d-5p (**c**) and the lithium 2s-2p (**a**) lines are present. A comparison between the two spectra can only be used for

Table 2.4: Li, Ag, and Pt lines observed in the experiment.

Label	Atom	λ (Å)		Transition
a	Li	6709		$1s^2 2p$–$1s^2 2s$
g	Li	6243		$1s^2 3p$–$1s^2 2p$, forbidden line
b	Li	6104		$1s^2 3d$–$1s^2 2p$
c	Ag	5470		$4d^{10}5d(^2D_{3/2})$–$4d^{10}5p(^2P_{3/2})$
				$4d^{10}5d(^2D_{5/2})$–$4d^{10}5p(^2P_{3/2})$
d	Ag	5211		$4d^{10}5d(^2D_{3/2})$–$4d^{10}5p(^2P_{1/2})$
e	Li	4972		$1s^2 4s$–$1s^2 2p$
f	Li/Ag/Pt	∼4600	Li:	$1s^2 4d$–$1s^2 2p$
			Ag:	$4d^{10}7s$–$4d^{10}5p$, $4d^{10}8p$–$4d^9 5s^2$,
				$4d^{10}5f$–$4d^9 5s^2$
			Pt:	$5d^8 6s^1 6p^1$–$5d^9 6s^1$

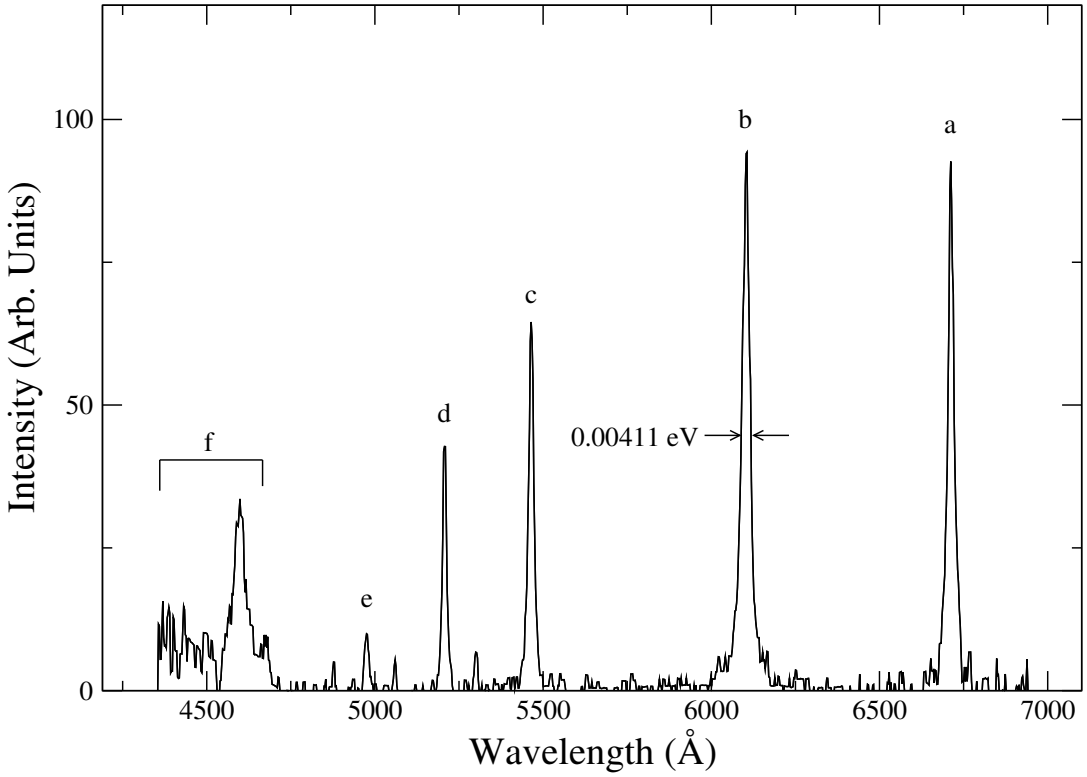

Figure 2.8: Lineout at x=231.6 μ m from surface, t=+50 nsec.

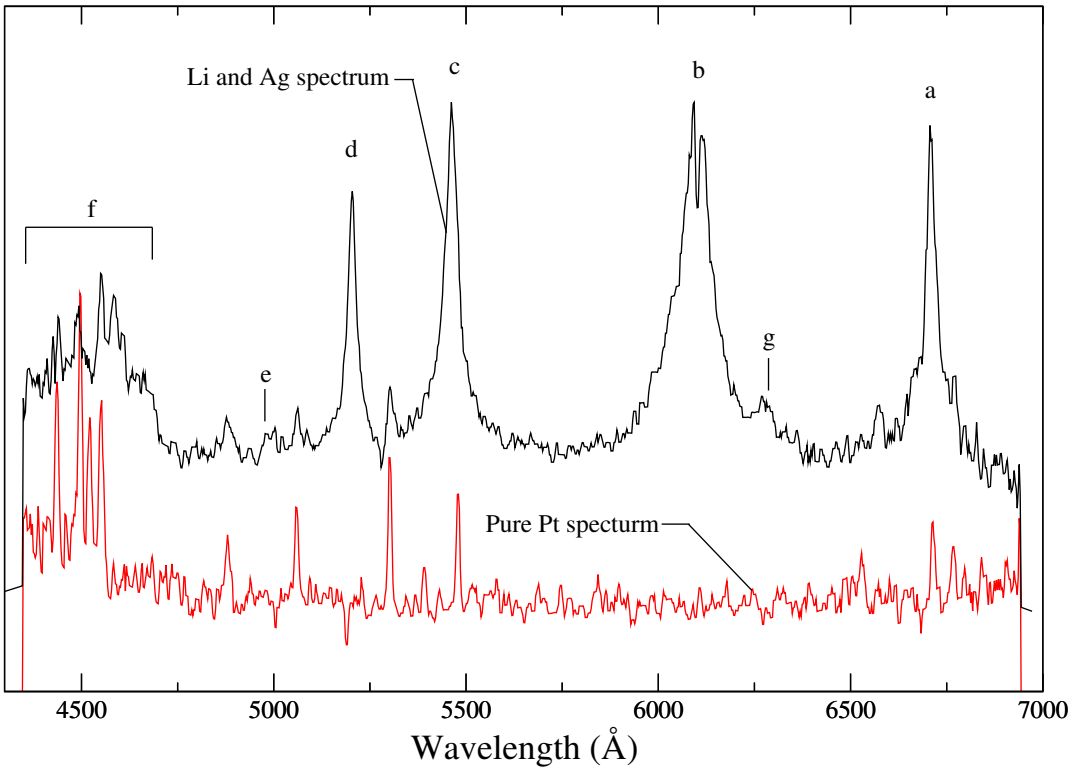

Figure 2.9: The superposition of two lineouts shows the location of platinum lines in the x=28.8 μ m, t=+20 nsec spectrum. The spectrum of a pure platinum target was recorded during the Li-Ag trails at t=+50 nsec, x=56.7 μm from the surface with a 10 ns gate time.

determining the location of some Pt lines. Plasma conditions differ greatly between the two systems making it difficult to predict the amount of Pt contributions in the above mentioned lines. Pt line identification is unknown at this time since nearly all energy levels in neutral platinum remain unidentified.

Chapter 3

Atomic Data for Neutrals and Low-charge Ions of Li and Ag

3.1 Introduction

Spectroscopic modeling was the primary approach chosen to interpret the Li-Ag ablation data. With such a model, a large number of synthetic spectra are generated for various plasma conditions; and then compared with spectral lineouts obtained from the experiment. Once a good match is obtained, the plasma conditions associated with the synthetic spectrum are assigned to those of the spectral lineout.

A synthetic spectrum is usually very sensitivite to the atomic structure and collision cross sections when the plasma is far from thermal equilibrium. A great deal of effort was dedicated to develop techniques to improve their accuracy. Due to the nature of the laser ablation with respect to their use in industrial applications, targets are often composed of compounds containing transition elements with $3d^w$, $4d^w$, $4f^w$ and $5f^w$ outer spin-orbitals for the ground state configuration. Elements such as these pose a considerable challenge in calculating accurate neutral atomic energy levels as well as wavefunctions needed in collisional cross sections and line profile calculations. This chapter will describe the discrepancies between experimentally determined en-

ergy levels and theoretically calculated values by Cowan's atomic structure code [17] for Ag as well as the semi-empirical technique employed to correct the discrepancies.

3.2 Atomic Structure of Transition Elements

Producing a high quality atomic structure calculation of transition-elements ($_{21}$Sc - $_{30}$Zn, $_{39}$Y - $_{48}$Cd, $_{57}$La - $_{80}$Hg) can be difficult. This difficulty arises from the complexity of these atoms can be illustrated in a comparison in the Grotrian diagram for Li and Ag (Figure A.1, A.2). In the case of neutral lithium only a singly excited state series exist below the ionization potential and a relatively weak dependency on the orbital angular-momentum-quantum number l of the last spin-orbital: to such an extent there are no configurations of a particular principal quantum number n found amongst the energies of a configuration of n+k where k=1, 2, 3 .... In comparison, the neutral Ag Grotrain diagram shows a strong dependence on l such as the $4d^{10}5d$ configuration amongst n=6 configurations. We also observed the beginning of the doubly excited state series amongst the first excited state configuration - $4d^{10}5p$. The strong dependence on l and the existence of low lying doubly excited states indicates the sensitivity of the atomic structure to the outer electrons penetrating through the core electrons and interacting with the positive charge of the nucleus. This is much more apparent with transition elements in general due to the large number of inner electons which shield the nucleus. This phenomenon can be qualitatively described by the aid of the non-relativistic Bohr-Sommerfeld model for the hydrogen atom [18], where the electron is limited to travel in an elliptical orbit with a focus centered at the nucleus. Orbitals with the same principal quantum number, in the case of hydrogen, are degenerate; which corresponds to the same semi-major axis having increasing

eccentricity with decreasing l. Small orbital angular momentum is associated with orbits that have a small perihelion. This is consistent with an increased binding energy of configurations with the same n of the upper spin-orbital and decreasing l. For the doubly excited states,a similar decrease in the energy of the configuration when a 4d electron is promoted to a 5s or to a 5p spin-orbital is seen. The effect of the core electron penetration is even more evident here, since atoms with a few core electrons have all their doubly excited states above the ionization potential.

3.3 Atomic Structure Calculations

Los Alamos National Laboratories T-4 group's CATS (Cowan's Atomic Structure Code) [19] was used to generate the energy eigenvalues and eigenfunctions needed in the spectroscopic model. CATS is a user friendly version of Robert Cowan's original suite of codes: RCN, RCN2 and RCG. A fourth code, RCE, belonging to Cowan's original suite of codes was implemented into CATS for this research to correct for inaccuracies in the calculated energy eigenvalues. The following is a summary of the function of each of Cowan's programs[17].

1.) RCN calculates the single-configuration radial wavefunction $P_{nl}(r)$ assuming a central-field model of the atom where electron i moves independently of the other electrons in a static electric field of the nucleus and time averaged spherically symmetric field of the n-1 electrons. RCN uses either Hartree-Fock (HF) or several other approximations for calculating the radial wavefunction. RCN produces the center-of-gravity energy (E_{av}) of the configuration and the Slater integrals F^k(i,j) and G^k(i,j), where F^k(i,j) and G^k(i,j) are the integrals found in the exchange and direct contributions to the electron-electron Coulomb energy term. In addition, the spin-orbit

integrals ζ are calculated. All these integrals are needed to calculate the energy levels of the configuration.

2.) RCN2 takes wavefunctions from RCN and generates configuration interaction Coulomb integrals R_k between interacting configurations of the same J and parity).

3.) RCG sets up and solves for each total angular momentum J, the energy matrices for the eigenvalues and multiconfigurational eigenvectors for various desired coupling schemes. RCG also generates many of the spectral transition data such as wavelength, radiative transition probabilities, etc.

Table 3.1 and table 3.2 show a comparison between experimentally obtained Ag energy levels[15],[16] and various HF calculations with inclusion of several energy correction terms. The HF option was chosen since it does not suffer from self-interaction in the potential and contains the appropriate exchange term in the potential. Table 3.1 and 3.2 shows the typical compression in the computed atomic structure of Ag as compared to the experimental values. Notice also that although both electron-electron correlation and relativistic corrections decrease the general discrepancy between the experimental and theoretical values the overall disparity is still high. In addition, a closer inspection of the tables shows an inconsistent ordering of calculated energy levels with respect to experimental values. Both the compression and the incorrect ordering of calculated energy levels makes the calculated data from CATS inappropriate for spectroscopic quality modeling.

To correct the energy levels structure and in turn their associated wavefunctions, Cowan's RCE procedure was used. After executing RCN to obtain the values of the radial energy parameters (Eav, Fk, Gk, zeta and Rk) and RCG to obtain the eigenvalues, the RCE procedure varies the above radial energy parameters in an iterative and interactive procedure with a least-square fit to experimentally obtained

Table 3.1: Comparison of experimentally obtained even parity energy levels and results from Cowan's atomic structure code – including various corrections.

J	CONFIG	(2S+1)L	EXP (cm^{-1})	NO CRCT (cm^{-1})	CORREL[a] (cm^{-1})	REL[b] (cm^{-1})	COR+REL[c] (cm^{-1})
0.5	5s	(1S) 2S	0.000	0.000	0.000	0.000	0.000
0.5	6s	(1S) 2S	42556.15	37923.600	38193.900	38511.800	38548.200
0.5	7s	(1S) 2S	51886.98	46740.200	47047.700	47389.200	47443.400
0.5	8s	(1S) 2S	55581.29	50293.200	50604.900	50955.900	51011.200
0.5	9s	(1S) 2S	57425.11	52082.600	52395.000	52750.300	52804.700
0.5	10s	(1S) 2S	58478.13	53110.100	53422.800	53780.200	53834.700
0.5	11s	(1S) 2S	59135.99	53754.500	54067.100	54425.900	54480.300
1.5	4d9 5s2	(2D) 2D	34714.16	35183.319	35159.851	34811.711	34820.321
1.5	5d	(1S) 2D	48744.00	43297.188	43567.792	43944.639	43955.155
1.5	6d	(1S) 2D	54203.13	48781.905	49083.727	49444.932	49488.484
1.5	7d	(1S) 2D	56699.79	51287.628	51595.625	51955.192	52005.904
1.5	8d	(1S) 2D	58050.01	52640.499	52950.775	53311.056	53363.389
1.5	9d	(1S) 2D	58862.46	53454.398	53765.821	54125.973	54178.901
1.5	10d	(1S) 2D	59388.97	53981.813	54293.359	54653.897	54707.446
2.5	4d9 5s2	(2D) 2D	30242.26	30766.707	30741.625	30441.580	30448.624
2.5	5d	(1S) 2D	48764.22	43304.191	43577.892	43952.759	43966.593
2.5	6d	(1S) 2D	54213.60	48786.527	49089.709	49449.895	49494.797
2.5	7d	(1S) 2D	56705.54	51290.124	51598.823	51957.969	52009.378
2.5	8d	(1S) 2D	58053.48	52642.118	52952.620	53312.690	53365.498
2.5	9d	(1S) 2D	58864.66	53455.320	53766.980	54126.904	54180.067
2.5	10d	(1S) 2D	59390.72	53982.513	54294.051	54654.602	54708.142
3.5	5g	(1S) 2G	56711.11	51309.500	51622.300	51979.400	52033.900
4.5	5g	(1S) 2G	56711.10	51309.500	51622.300	51979.400	52033.900

[a]Correlation energy per electron based on a zero-temperature free-electron-gas model with high density semi-empirical correction[20].

[b]First-order relativistic correction to the Schrodinger equation: mass-velocity, Darwin and spin-orbit terms [21].

[c]Includes both correlation energy and first-order relativistic correction.

Table 3.2: Comparison of experimentally obtained odd parity energy levels and results from Cowan's atomic structure code for Ag – including various corrections.

J	CONFIG	(2S+1)L	EXP (cm^{-1})	NO CRCT (cm^{-1})	CORREL[a] (cm^{-1})	REL[b] (cm^{-1})	COR+REL[c] (cm^{-1})
0.5	5p	(1S) 2P	29552.05	25749.958	25626.304	26107.298	25815.211
0.5	7p	(1S) 2P	54040.99	48789.900	49105.118	49438.535	49498.593
0.5	8p	(1S) 2P	56620.72	51287.101	51601.001	51946.368	52003.544
0.5	4d9 5s 5p	(3D) 4P	60537.50	53338.420	53162.636	53457.764	53068.787
0.5	9p	(1S) 2P	58005.20	52633.268	52929.392	53274.586	53378.278
0.5	10p	(1S) 2P	58834.25	53490.570	53773.670	54127.219	54180.513
1.5	5p	(1S) 2P	30472.71	26227.513	26223.201	26667.597	26510.215
1.5	6p	(1S) 2P	48500.77	43429.491	43750.255	44063.347	44136.019
1.5	7p	(1S) 2P	54121.16	48846.027	49164.504	49501.292	49564.529
1.5	8p	(1S) 2P	56660.57	51304.696	51655.141	51997.949	52049.702
1.5	4d9 5s 5p	(3D) 4P	58504.70	49871.907	51350.853	51623.595	51243.855
1.5	10p	(1S) 2P	58849.83	53467.188	53782.242	54136.941	54192.661
2.5	4f	(1S) 2F	54204.73	48805.240	49116.071	49469.825	49523.130
2.5	4d9 5s 5p	(3D) 4P	56223.30	49871.907	49527.083	49754.447	49295.259
2.5	5f	(1S) 2F	56691.40	51283.578	51592.724	51950.139	52015.747
2.5	4d9 5s 5p	(3D) 4F	59321.10	52196.933	51952.373	52253.358	51882.577
2.5	6f	(1S) 2F	58055.56	52636.526	52947.140	53305.237	53358.825
3.5	4f	(1S) 2F	54204.73	48805.433	49116.338	49470.074	49523.459
3.5	4d9 5s 5p	(3D) 4F	58789.70	51622.968	51381.621	51609.162	51265.543
3.5	5f	(1S) 2F	56691.40	51283.621	51598.194	51954.662	52007.057
3.5	6f	(1S) 2F	58055.56	52635.064	52946.468	53304.654	53358.133
4.5	4d9 5s 5p	(3D) 4F	58901.90	51461.056	51260.216	51465.872	51167.882

[a]Correlation energy per electron based on a zero-temperature free-electron-gas model with high density semi-empirical correction[20].

[b]First-order relativistic correction to the Schrodinger equation: mass-velocity, Darwin and spin-orbit terms [21].

[c]Includes both correlation energy and first-order relativistic correction.

energy levels. The newly obtained radial energy parameters are then used in a new RCG calculation to obtain the corrected wavefunctions.

To correct the energy level structure, Cowan's RCE [22] procedure was implemented into CATS. The code development contained a significant number of technical challenges due to incompatibility issues. The only existing version of RCE was associated with the latest versions of the RCN, RCN2 and RCG programs. Since CATS is based on a very early version of Cowan's code and has undergone fifteen years of separate development, data, data structures and file formats had to be modified for interoperability. All modifications were introduced in an interface module inserted into RCG to replace the original RCE interface tool. With a new set of conditionals (flags) placed into CATS, the RCE module could be executed after the proper experimental energy levels data was provided. A secondary conditional allowed CATS to access the new radial energy parameters to produce the associated wavefunctions. These wavefunctions are then used in ACE (a program for calculating electron impact excitation (ECE) [23])and GIPPER (a program for calculating electron impact ionization (ECI) cross sections) both developed by members of T-4 Los Alamos National Laboratory. It should be noted that both ACE and GIPPER programs allow for several different collisional models to be invoked to produce cross sections. In the early stages of this work, a large study was undertaken to determine the best collisional models within ACE and GIPPER for generating neutral atoms cross sections. Over 600 sets of ACE generated carbon cross sections were compared. Each set contained results from a distorted-wave (DW) calculation where the free-electron wave function (FEWF) was obtained through either the distorted wave equations themselves or by Coulomb functions and first-order many-body theory calculation.

The fully DW calculations produced a high number of pathological cross sections,

even with additional terms included in the partial wave expansion. For this reason, Coulomb FEWF cross sections were chosen.

Due to the high number of pathological cross sections, even with additional terms included in the partial wave expansion for the fully DW calculations, the DW calculations with Coulomb FEWF cross sections were chosen. In the case of GIPPER, automated smoothing and cross section correction prevented the appearence of pathological cases. From the advice of members of T-4, the cross sections generated with the fully DW technique were chosen. A similar, though smaller, survey was done with Ag and similar results were found.

The RCE procedure produced energy eigenvalues to five significant figures of the experimental data found for silver. The comparisons between ACE excitation cross sections with and without RCE improved wavefunctions varied. The largest cross sections underwent a reduction as great as 13% as seen in the Ag I $4d^{10}5s^2S_{1/2} - 4d^{10}5p^2P_{1/2}$ transition, while others produce only minor changes as seen in the Ag I $4d^{10}5p^2P_{1/2} - 4d^{10}5p^2P_{1/2}$ transition of figure 3.1. In a similar manner, some small cross sections underwent a more drastic change with some values increasing. Though these changes in cross sections may not appear significant, they do lead to significant changes in the corresponding rate as seen in figure 3.2, in particular, for the low electron temperatures found in ablation plasmas.

It has been observed by members of T-4 that when experimental data has become available, the ECE cross sections for neutral systems were overestimated by ACE calculations. In a comparative study of Ba I, several techniques for the calculation of excitation cross sections were compared with experimental data. The ACE calculations with the non-RCE corrected wavefunctions overestimated the cross sections for strong transition by 10%. ACE calculations employing the RCE correction showed an

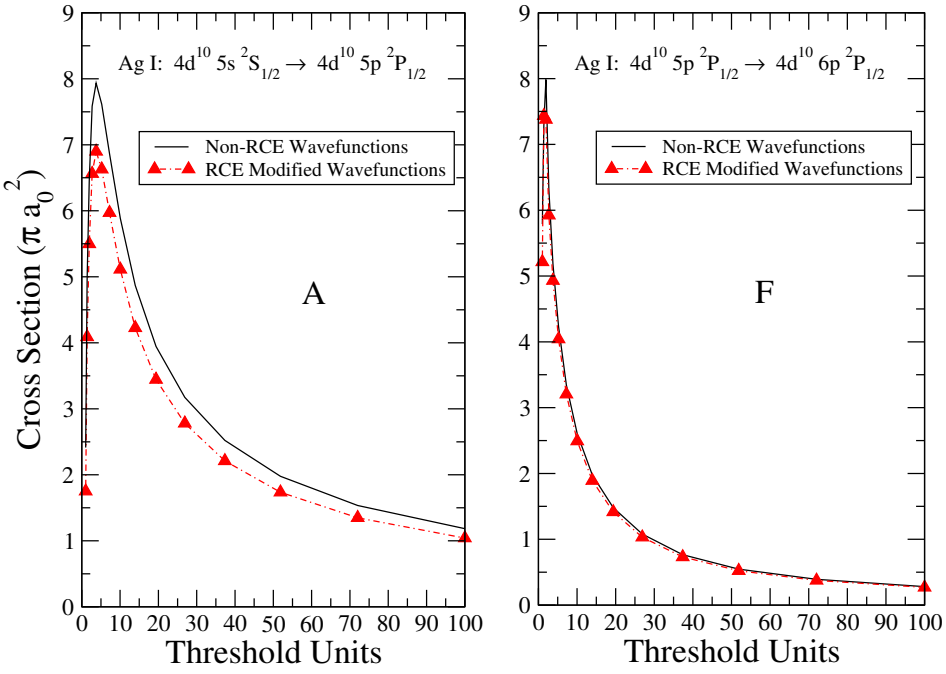

Figure 3.1: Comparison of electron impact excitation cross sections generated with and with RCE modifications of the wavefunctions. The two figures correspond to an allowed **A** (left) and forbidden **F** (right) transitions.

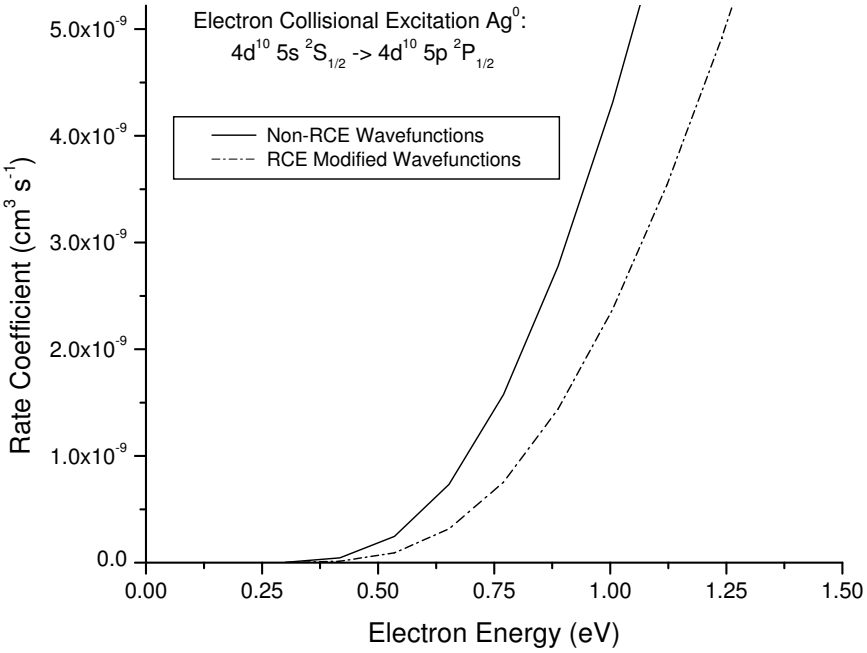

Figure 3.2: A comparison of an electron impact excitation rate for silver generated with and without wavefunction modifications by the RCE procedure.

improvement in the cross sections and produced values comparable to those produced by more elaborate methods.

3.4 Obtaining Rate Coefficients

The need to produce a database of synthetic spectra for comparison against experimental lineouts, or the need to calculate a single synthetic spectrum which takes into account continuum lowering in the atomic kinetics (i.e. requiring a re-calculation of the ionizing rate coefficients for each iteration in the self-consistent population calculation), demands a quick and robust technique for generating the large number of rate coefficients from their corresponding cross sections. Furthermore, due to the large number of generated cross sections, an automated procedure is required to check and survey the data to insure its quality. This is particularly important for neutral and near neutral ionic species, since programs such CAT, ACE and GIPPER were designed predominantly for generating atomic structure and collision data. In turn, hand tuning is required far more frequently for these neutral and near-neutral species.

Assuming a Maxwellian distribution for the free electrons, equation (3.1) must be solved to determine the electron collisional excitation or ionization rate coefficients. In this equation, $\sigma_{i,j}$ is the collisional cross section, u is the energy of the projectile electron and u_o is the threshold energy of the transition:

$$q_{i,j} = \pi {a_o}^2 \left(\frac{8k}{\pi m}\right)^2 \int_{u_o}^{\infty} \sigma_{i,j}(u)\ u e^{-u}\, du\ . \tag{3.1}$$

To solve for the spontaneous radiative recombination rate, a similar integral equation (3.2) must be solved where $\alpha_{i,j}(\nu)$ is the photoionization cross section at frequency

ν and ν_0 is the threshold frequency of the transition.

$$R_{j,i} \equiv 4\pi \int_{\nu_o}^{\infty} \alpha_{i,j}(\nu) (h\nu)^{-1} \left[\left(2h\nu^3/c^2 \right) \right] e^{-h\nu/kT} d\nu \ . \tag{3.2}$$

Two techniques were investigated to solve the integrals in these equations.

3.4.1 Semi-Analytical Method

The first technique involved obtaining a generalized fitting function for the cross sections. With the fitting function, an analytical solution for the integral was obtained as a function of the fitting coefficients, the ratio of the electron temperature and the threshold energy of the transition. This technique had the advantage of producing a fast solution to the evaluation of the integral due to the use of an analytic solution. For electron-impact ionization, a fitting function reported by Sampson [24] was originally used. Later, however, through comparisons of the fitted analytical expression to the GIPPER generated cross sections, the fitting functions where modified to improve their accuracy. The consistency of the form of GIPPER's ionization cross sections lead to a very efficient evaluation of the integral and in turn the rate coefficients.

A similar procedure was implemented for electron impact excitation cross sections. Due to the nature of these cross sections, two distinct forms exist: ECI transitions that corresponding to allowed radiative transitions are characterized by a thick, $\ln(x)/x$ dominated tail, and transitions that corresponding to forbidden radiative transition are characterized by a thin $1/x^n$ tail, where x is the energy of the projectile electron. Examples of these predominant forms are found in figure 3.1. Not all the strong cross sections fell into these two forms, and in particular, cross sections corresponding to double-electron excitation did not. These pathological cases had to be handled on an individual basis, and prevented a fully automated procedure for

determining the rates thus requiring an inspection of each fitted cross section.

When the same semi-analytic procedure was employed to determine the spontaneous radiative recombination rate, the large variation in the form of the GIPPER generated photoionization cross sections prevented any single fitting function to approximate the cross section data well. After several attempts with more complex fitting functions, the procedure was later abandoned for obtaining this rate.

3.4.2 Numerical Method

The lack of success in determining the radiative recombination rates required a new technique less sensitive to the shape of the cross sections. The Gauss-Laguerre quadrature integration method was implemented in the following form:

$$\int_0^\infty x^\alpha e^{-x} f(x)\, dx = \sum_{j=1}^{N} w_j f(x) \quad , \tag{3.3}$$

were the x_i's and w_j's are the quadrature abscissa and weights respectively [25]. In the quadrature method, the function $f(x)$ must be evaluated at each abscissas x_i. For our applications, after employing the proper substitutions to change the lower limit from the threshold values found in equations (3.1) and (3.2) to 0, the $f(x)$ represents either the photoionization, collisional excitation or ionization cross sections with some additional constants. The need to evaluate the cross sections at each abscissa value inferred the use of an interpolation routine to evaluate the cross sections at those specific points. At times, the abscissas would go beyond the range of the TAPS generated projectile energy values or photon energy values of the collisional and radiative cross sections respectively, requiring an extrapolation of the tail. Such an extrapolation was performed on the logarithm of the cross sections to prevent the extrapolation to negative values. Though the Gauss-Laguerre integration method was

able to overcome the difficulties associated with various forms of the cross sections produced by TAPS, a considerable performance cost came from the time required to interpolate and extrapolate the cross sections.

3.4.3 Cross-Section Survey

As mentioned above, the extent of the collision data needed for our Li-Ag atomic kinetic modeling required an automated way of analyzing and selecting out poor cross sections. To accomplish this, a procedure was implemented to compare each TAPS generated cross section to the expected behavior of a total cross section; maximum value between 1 and 3 threshold units; no more than one maximum; and a monotonically decreasing tail. Data not consistent with these qualities were separated for hand inspection.

3.5 Ab initio Calculated vs Generic Excitation Rates

This chapter concludes with a comparative study of collisional excitation rates obtained by two different techniques. Early in the development of this work, before the access to the TAPS suite of collision codes, an atomic kinetic model based on generic rates described in the work by Epstein [26] was developed to model synthetic spectra and various other plasma parameters. Generic rates try to approximate both electron collisional as well as radiative rates found in plasmas without the need of complex and computationally costly collision codes. Many rely on, including collisional excitation, the typical high electron energy behavior of cross sections found in electric dipole allowed transitions [27]. Details at and leading down to threshold are

corrected by the use of multiplicative factors (g Gaunt factors), often a function of $E/\Delta E$ where E is the energy of the incoming electron and ΔE is the energy of the transition. Approximations to the collisions employed in these rates require specific target information. This information is obtained through energy eigevalues and oscillator strengths between allowed initial and final target states. Though no stringent selection rules exist for collisional processes, these rates only provide information between allowed transitions. Even with this limitation, models based on these rates have produced reasonable results in moderate to highly ionized systems. This previous development allows us here to compare the results obtained from both generic and ab initio calculations for at least collisional excitation. For both techniques, the RCE procedure was used in the case of Ag to have a consistent set of eigenvalues and eigenfunctions with which to make the comparison. Figures 3.3, 3.4, 3.5, 3.6 show a consistent overestimation by the generic rates in both the region of high energy and near threshold portions of the cross sections for both Li and Ag targets. These generic rates appear to be inappropriate in non-LTE (local thermodynamic equlibrium) low temperature plasmas with a large number of neutral constituents, and would greatly underestimate the electron density needed to establish a plasma in LTE conditions [28].

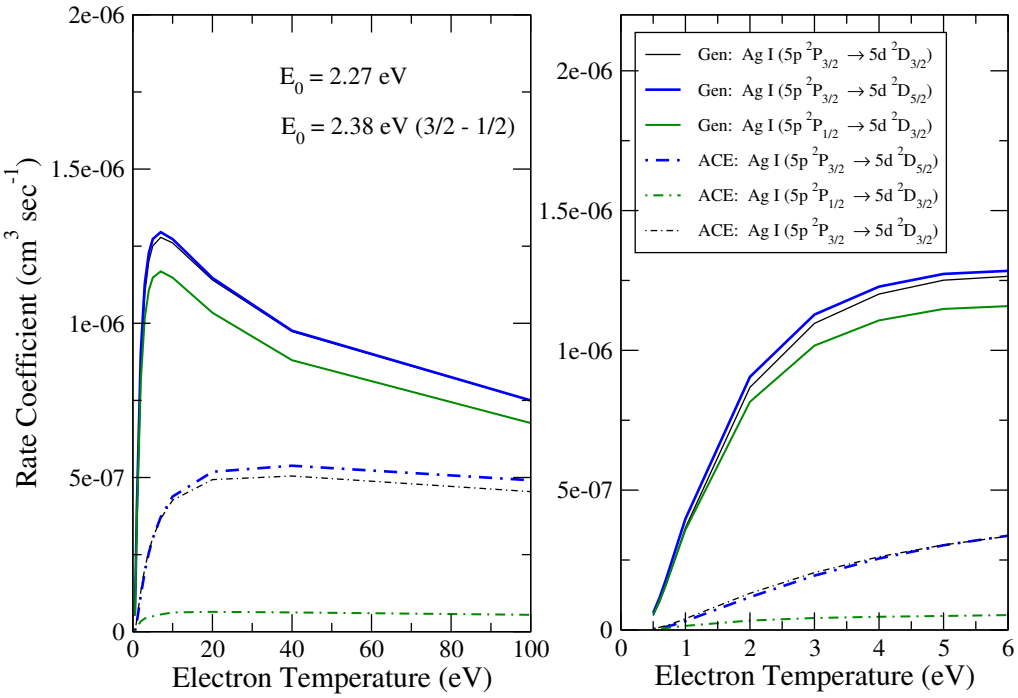

Figure 3.3: Comparison of collisional excitation rate transitions for Ag I: 5p - 5d transitions for generic and ab initio calculations (ACE).

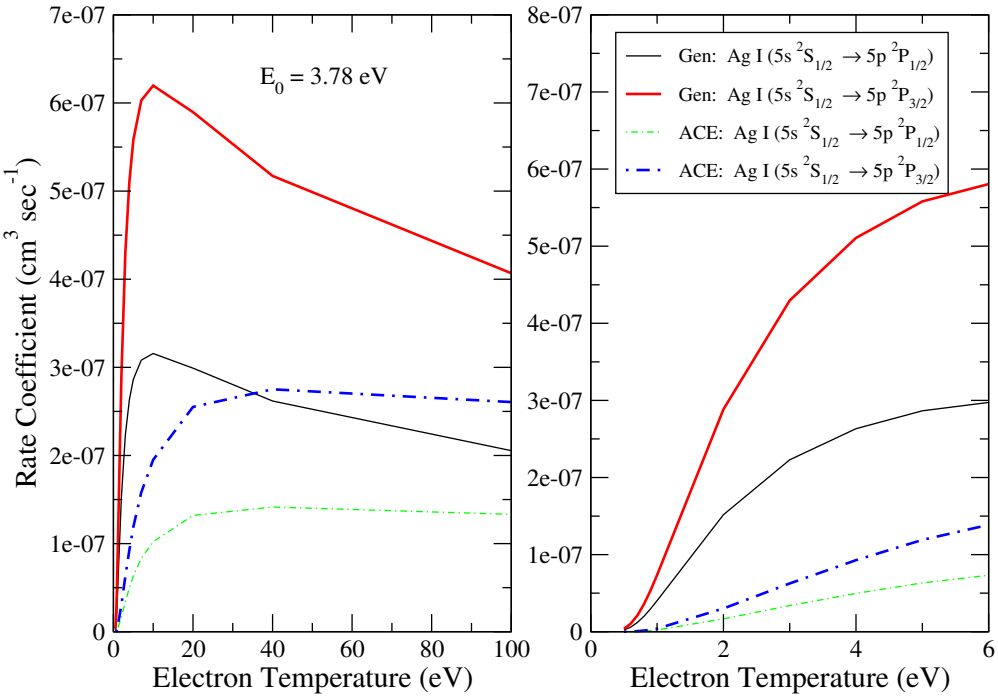

Figure 3.4: Comparison of collisional excitation rate transitions for Ag I: 5s - 5p transitions for generic and ab initio calculations (ACE).

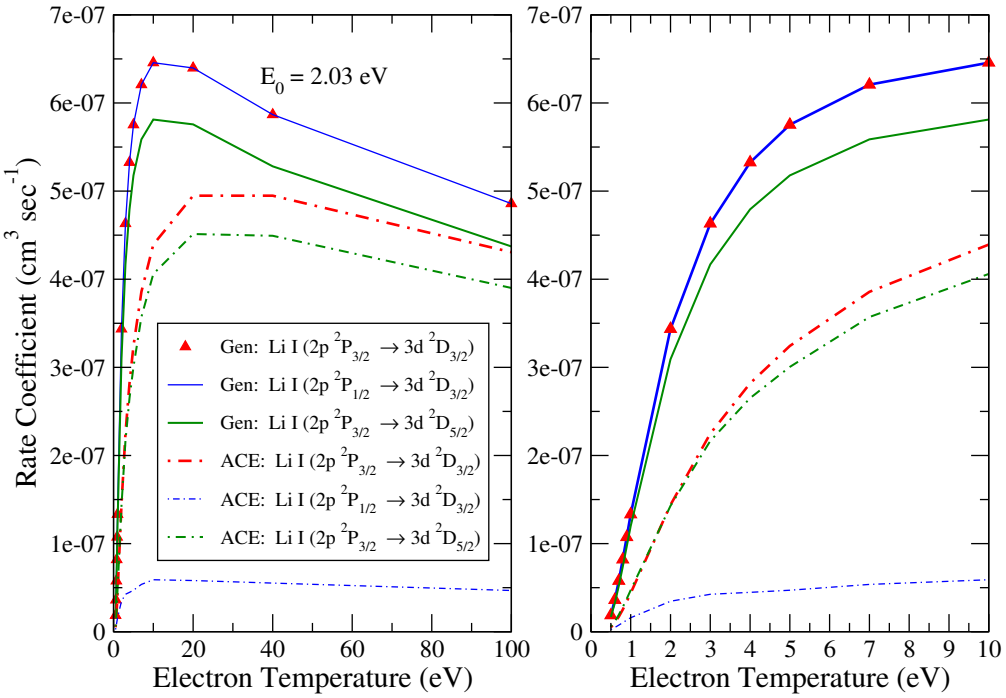

Figure 3.5: Comparison of collisional excitation rate transitions for Li I: 2p - 3d transitions for generic and ab initio calculations (ACE).

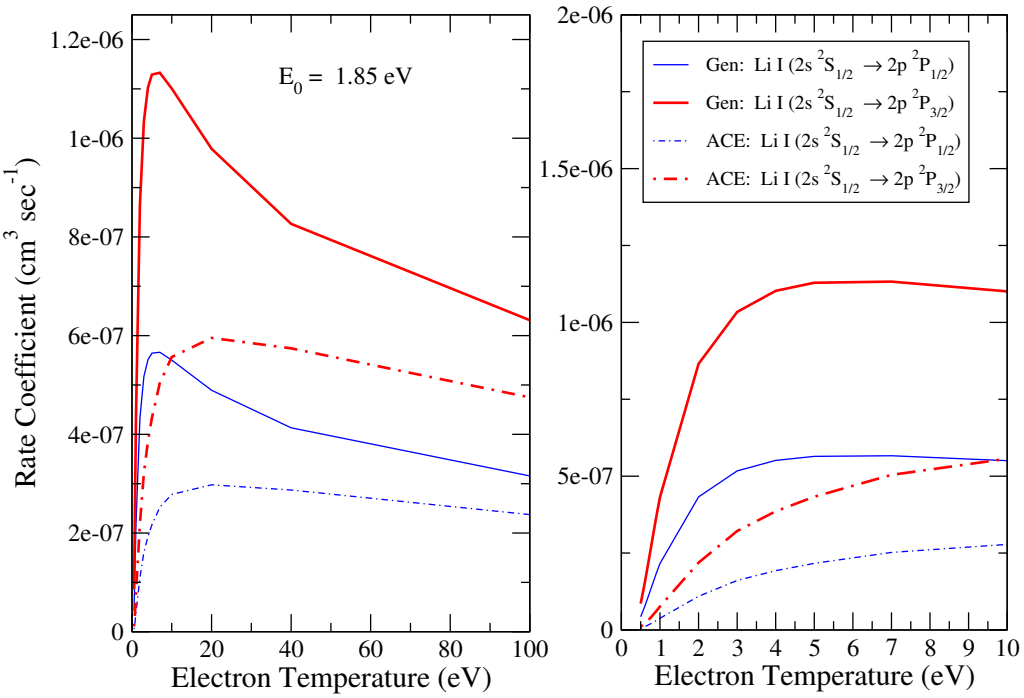

Figure 3.6: Comparison of collisional excitation rate transitions for Li I: 2s - 2p transitions for generic and ab initio calculations (ACE).

Chapter 4

Atomic Kinetics of Li-Ag Plasma Plumes

4.1 Introduction

Due to the complexity of the materials of modern microelectronics, one commonly finds multi-element laser ablation targets with nearly equal abundances of each element. This implies that the atomic kinetics of this type of plasma can not be modeled by assuming that the level populations and ionization balance for each element in the plasma are weakly influenced by the other elemental species. For this research, a new algorithm was developed to calculate level populations in ablation plasmas by including the effects between several species through their interaction with the common free electron pool.

It should be emphasized that multi-element ablation plasmas contrast sharply with the common multi-element, high intensity laser driven plasmas, in which a trace amount of high Z material is added for use as a plasma diagnostic. Care is taken in the high intensity laser driven experiment to choose an amount of tracer material (e.g. Ar) that is small enough not to affect the dynamics of the main plasma material (e.g. D_2) – which is often fully ionized – yet large enough to produce a sufficiently

strong signal for detection by diagnostic instruments. If these two criteria are met, only the atomic kinetics of the tracer element has to be addressed in detail.

Similar to the common laser ablation target mentioned above, the SNL target contained nearly equal abundances of Ag and Li, 57% and 43% respectively in the ablation plume, where both elements contribute significantly to the free electron pool for the expected densities and temperatures for this experiment. Due to their contrasting atomic structure, each element's fractional contribution to the total electron pool is strongly correlated to the temperature and density found for these ablation plasmas. At low temperatures (less than 1 eV), Li is more ionized than Ag since the ionization potential of Li ($I_p = 5.392$ eV) is smaller than that for Ag ($I_p = 7.574$ eV). To illustrate this idea, Figure 4.1 displays the effect of the temperature on the fractional populations of Ag and Li energy levels for an electron density of $1x10^{17}$ cm^{-3}. As the temperature increases from 1 eV to 3 eV, Ag atoms ionize and effectively populate states in Ag^{+1} and Ag^{+2}, while the population distribution of the Li states remains relatively unchanged and mainly accumulates in the Li^{+1} ion ground state due to the 60.9 eV transition energy needed for an excitation to the first excited state.

4.2 Atomic Kinetic Model

The atomic kinetics model considers the neutral Ag atom and its first three ionization stages; and the neutral Li atom and its first two ionization stages. Since the second ionization potential of Li is 75.6 eV (compared to 5.392 eV for the first ionization potential) and the range of relevant temperatures is between 0.5 eV and 2.0 eV, very little population is expected to reside in the higher ionization stages of

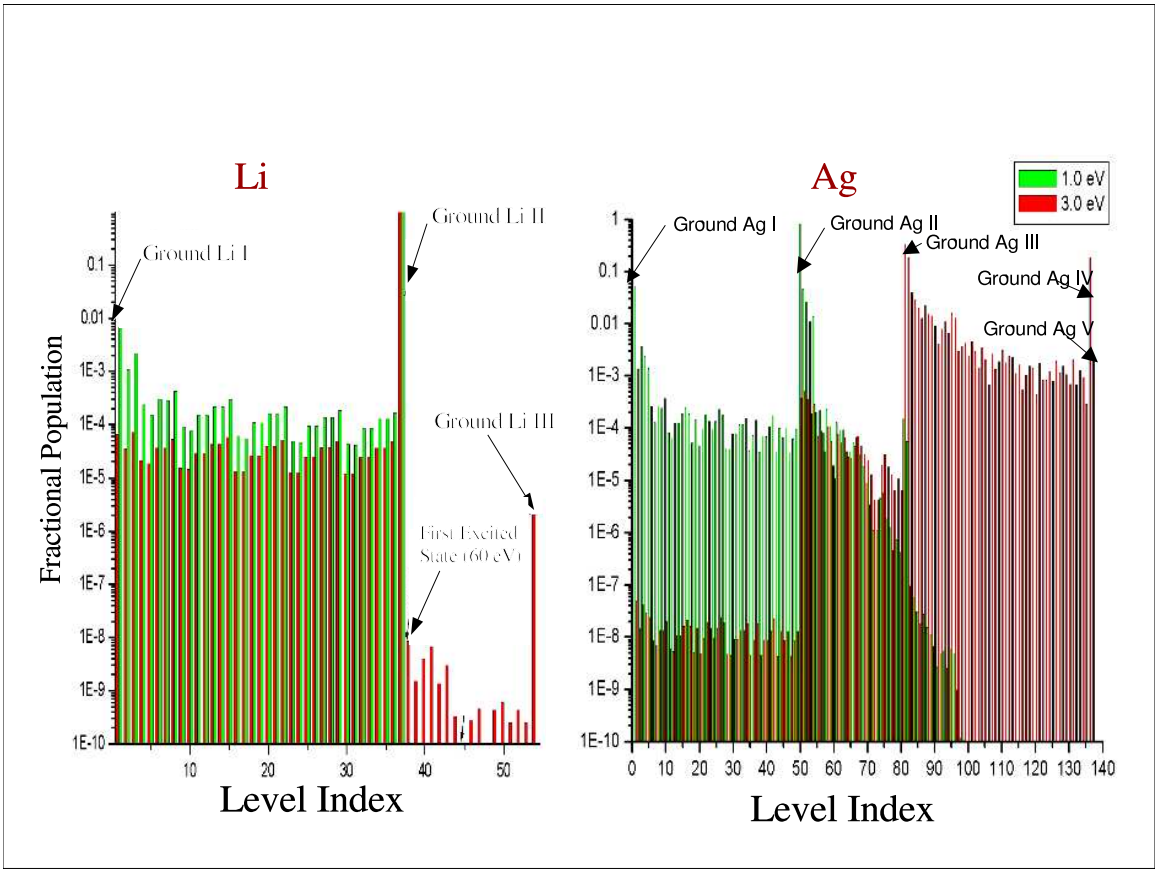

Figure 4.1: The effect of temperature on fractional level populations for three ionization stages in Li and five in Ag atoms, for an electron density of 1x10^{17} cm^{-3}.

Li. In each atom/ion, ground and several excited states are considered, including some autoionization states. Fine-structure energy levels are used to describe excited states in dominant line transitions identified in the recorded spectra for the analysis. Configuration average energies are used for the first and second ionization stages of Ag, respectively. This use of coarser grain atomic structure representations for non-spectroscopically significant ionization stages in Ag arises from the compromise between having to include these ionization stages in the determination of the appropriate ionization balance, and overcoming the technical difficulty of representing the atomic stages of partially-filled d-shell ions. Ions such as Ag^{+2} would require 1100 levels to properly describe 90% of its energy level structure below the ionization potential, not including autoionizing states. Hence, representing Ag^{+2} at the fine structure level of description would require the calculation of 605,000 electron collisional cross sections; while in the configuration average representation, only 512 electron collisional excitation cross sections are needed (Table 4.1). To implement an aggregate of energy level representations, one must determine from a calculated ionization rate coefficient (IRC) the labels for the initial and final states in the coarse grain representation and the value of the corresponding IRC labels for the in-ital and final states in the fine and coarse grain representation respectively. The inverse rate is then obtained by detailed balance arguments [29]. It can be shown that the rate coefficient linking initial and final states in the fine and coarse grain representation, respectively, is equal to the rate coefficient with both initial and final states in the coarse grain representation. The level-term to term-term rate relationship is given by

$$R_{JL'S'} = R_{LSL'S'} \ . \tag{4.1}$$

Table 4.1: Detailed ionization and energy level structure of lithium and silver included in atomic kinetic model.

Element	Ionization stage	Number of levels	Largest principal quantum number	Representation
Li	I	36	7	levels
Li	II	22	7	levels
Li	III	1	1	levels
Ag	I	44	10	levels
Ag	II	32	10	configurations
Ag	III	32	10	configurations
Ag	IV	1	1	configurations

In this equation, primed variables represent the upper final energy group. Similarly, the term-configuration to configuration-configuration rate relationship is given by

$$R_{LSC} = R_{CC'} \ . \tag{4.2}$$

Though this procedure, from an analytical point of view, appears straightforward, the technique requires four re-mappings of cross section labels for its implementation in a computer code. Due to the complexity of the bookkeeping of labels, a data structure was produced to handle the mappings for the general multi-representational case.

4.3 Single Element Atomic Kinetic Model

In a single element plasma, the atomic kinetic model constitutes N rate equations that describes the rate of change of population for each level, where N is the total number of energy levels included in the kinetic model.

$$\frac{df_n}{dt} = A_{n,1}f_1 + A_{n,2}f_2 + \ldots + A_{n,n-1}f_{n-1} + A_{n,n}f_n + A_{n,n+1}f_{n+1} + \\ + \ldots + A_{n,N-1}f_{N-1} + A_{n,N}f_N \tag{4.3}$$

Equation 4.3 describes the rate of change of population of level n. Each $A_{n,m}$ term, where n $\neq$ m is equal to the sum of all collisional and radiative rates that transfer population from level m to level n. Correspondingly, $A_{n,n}$ represents the rate of depopulation from level n to all other levels, and in turn, it is given a negative value to represent a reduction in population of level n. The $A_{n,n}$ term is equal to the sum of all collisional and radiative rates that transfer population from level n to all other levels. Each level included in the model has a corresponding equation. The set of equations may be represented in a matrix form Eq. 4.4

$$\begin{pmatrix} \frac{df_1}{dt} \\ \frac{df_2}{dt} \\ \vdots \\ \frac{df_N}{dt} \end{pmatrix} = \begin{pmatrix} A_{11} & A_{12} & \ldots & A_{1N} \\ A_{21} & A_{22} & \ldots & A_{2N} \\ \vdots & \vdots & \ddots & \vdots \\ A_{N,1} & A_{N,2} & \ldots & A_{N,N} \end{pmatrix} \begin{pmatrix} f_1 \\ f_2 \\ \vdots \\ f_N \end{pmatrix} \tag{4.4}$$

or as Eq. 4.5

$$\frac{d\boldsymbol{f}}{dt} = A\boldsymbol{f} \tag{4.5}$$

For the special case of a plasma in steady state, the population of the levels remain constant or more precisely $df_n/dt = 0$ for all n. Unfortunately, the equations represented by Eq. (4.4) are not linearly independent, or in other words, A is singular: $det|A| = 0$. To circumvent this difficulty the fractional population normalization condition $\sum_{n=1}^{N} f_n = 1$ is substituted for one of the df_n/dt rate equations. By substituting the last rate equation for the normalization condition and by taking the inverse of both sides of Eq. (4.4) we obtain for the steady state solution Eq. (4.6)

$$\begin{pmatrix} f_1 \\ f_2 \\ \vdots \\ f_{N-1} \\ f_N \end{pmatrix} = \begin{pmatrix} A_{11} & A_{12} & \dots & A_{1,N-1} & A_{1N} \\ A_{21} & A_{22} & \dots & A_{2,N-1} & A_{2N} \\ \vdots & \vdots & \ddots & \vdots & \vdots \\ A_{N-1,1} & A_{N-1,2} & \dots & A_{N-1,N-1} & A_{N-1,N} \\ 1 & 1 & \dots & 1 & 1 \end{pmatrix}^{-1} \begin{pmatrix} 0 \\ 0 \\ \vdots \\ 0 \\ 1 \end{pmatrix} \tag{4.6}$$

or as Eq. (4.7)

$$\boldsymbol{f} = \left[A^{'}\right]^{-1} \boldsymbol{b} \tag{4.7}$$

Several collisional and radiative atomic processes are included in the atomic kinetic model discussed above, namely, electron collisional excitation and de-excitation, electron collisional ionization and recombination, dielectronic recombination [30], spontaneous radiative decay and photo-excitation, radiative recombination and photo-ionization and multi-photon ionization [31]. Atomic rates associated with these processes are used to compute the matrix elements of of the matrix **A** in the set of equations Eq.(4.3). Ground and excited states of adjacent ionization stages are fully coupled through these atomic processes (see Figure 4.2).

4.3.1 Time-dependent Atomic Kinetics

For the case of a time dependent system, the time derivative of the fractional population in Eq. (4.5) may be discretized in several ways. Because of its numerical stability, the one chosen in this work was the fully implicit scheme,

$$\frac{\boldsymbol{f}^t - \boldsymbol{f}^{t-1}}{\Delta\tau^{t-1/2}} = A\boldsymbol{f}^t \ . \tag{4.8}$$

In this equation, $\boldsymbol{f}^t$ and $\boldsymbol{f}^{t-1}$ are the fractional population vectors of the current and previous time step, respectively. Due to the finite difference approximation to the time derivative in Eq. (4.8), numerical error can, after several $\Delta\tau$ time steps, destroy

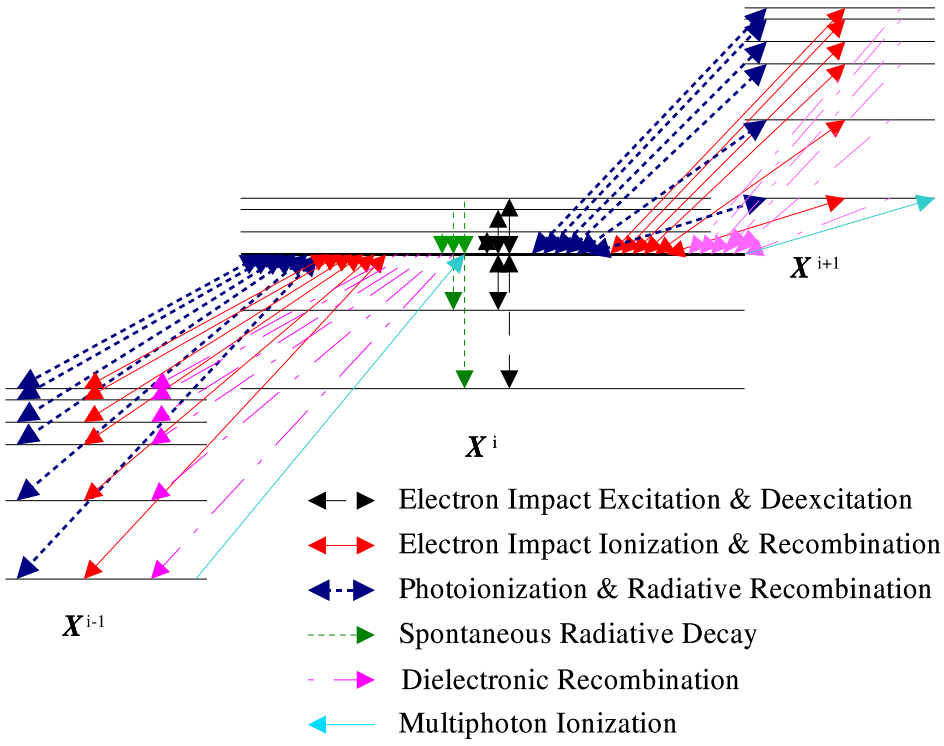

Figure 4.2: Collisional and radiative processes included in the atomic kinetic model.

the fractional population normalization condition, $\sum_{n=1}^{N} f_n = 1$, required by $\boldsymbol{f}^t$. To insure this condition is maintained, we may, as seen in the steady state case, replace one of the rate equations with the normalization conditions. After expanding and rearranging, we obtain the set of Eqs.,

$$\begin{array}{rcccccccc} {f_1}^t - {f_1}^{t-1} & = & A_{11}\Delta\tau^{t-1/2}{f_1}^t & + & \ldots & + & A_{1N}\Delta\tau^{t-1/2}{f_N}^t \\ f_{N-1}^t - f_{N-1}^{t-1} & = & A_{N-11}\Delta\tau^{t-1/2}{f_1}^t & + & \ldots & + & A_{N-1N}\Delta\tau^{t-1/2}{f_N}^t \\ \vdots & \vdots & \vdots & \vdots & \vdots & \vdots & \vdots \\ 1 & = & {f_1}^t & + & \ldots & + & {f_N}^t \end{array} \tag{4.9}$$

gathering like terms and solving in each equation for the fractional population of the previous time step we obtain,

$$\begin{array}{rcccc} {f_1}^{t-1} & = & (1 - A_{11}\Delta\tau^{t-1/2}){f_1}^t + & \ldots & -A_{1N-1}\Delta\tau^{t-1/2}f_{N-1}^t + \\ & & -A_{1N}\Delta\tau^{t-1/2}{f_N}^t & & \\ \vdots & \vdots & & \vdots & \\ f_{N-1}^{t-1} & = & -A_{N-11}\Delta\tau^{t-1/2}{f_1}^t + & \ldots & +(1 - A_{N-1N-1}\Delta\tau^{t-1/2})f_{N-1}^t + \\ & & -A_{N-1N}\Delta\tau^{t-1/2}{f_N}^t & & \\ 1 & = & {f_1}^t + & \ldots & +f_{N-1}^t + {f_N}^t \end{array} \tag{4.10}$$

We now may write the set of Eqs. (4.10) in matrix form,

$$\boldsymbol{r}^{t-1} = T\boldsymbol{s}^t \tag{4.11}$$

where,

$$\boldsymbol{r}^{t-1} = \begin{pmatrix} {f_1}^{t-1} \\ \vdots \\ f_{N-1}^{t-1} \\ 1 \end{pmatrix}$$

$$\boldsymbol{s}^t = \begin{pmatrix} {f_1}^t \\ \vdots \\ f_{N-1}^t \\ f_N^t \end{pmatrix} \tag{4.12}$$

$$T = \begin{pmatrix} (1 - A_{11}\Delta\tau^{t-1/2}) & \dots & -A_{1N-1}\Delta\tau^{t-1/2} & -A_{1N}\Delta\tau^{t-1/2} \\ \vdots & \ddots & \vdots & \vdots \\ -A_{N-11}\Delta\tau^{t-1/2} & \dots & (1 - A_{N-1N-1}\Delta\tau^{t-1/2}) & -A_{N-1N}\Delta\tau^{t-1/2} \end{pmatrix}$$

then operating on both sides of the equation by T^{-1}, we obtain the factional population of the current time from the previous time,

$$\boldsymbol{s}^t = T^{-1}\boldsymbol{r}^{t-1}. \tag{4.13}$$

It should be noted that an initial population is needed to calculate the population of the next time step as described in Eq. (4.13). This population is taken from the plasma in a steady state regime with density and temperature extracted from spectroscopic measurements. In our case, this condition is satisfied when the plasma is dense (early in time and close to the ablation surface).

4.4 Multi-Element Atomic Kinetic Model

Now we turn our attention to the multi-element atomic kinetic model. As mentioned in the introduction of this chapter, a new algorithm had to be developed for this case. We assumed that the rate of electron collisions with neutrals and ions exceeds those between ion-ion and ion-neutral collisions due to the electron's higher average speed, and thereby will overshadow the effects of ion-ion and ion-neutral collisions on the atom/ion populations. For more intense laser driven plasmas, this assumption is further supported by a larger number of free electron to ion ratio due to

those plasmas having a high average ionization. One additional assumption requires that the electron number density remain large enough such that the electron pool is thermalized, or in other words, it can be described by a Maxwellian distribution. Similarly, the absence of laser irradiation during the plasma expansion phase (recall the spectrum is recorded after the end of the laser pulse) simplifies the analysis of the SNL Li-Ag plasma. Laser energy is predominantly transfered to the free electrons which would require a non-zero thermalization time to equilibrate with the electrons in lower free-electron densities.

Since interactions between species are limited to those that occur through the pool of free electrons, the calculation of each species level populations is predominately independent of the others. For the steady state plasma, the calculations begin with the input of the total atom number density, N_a and electron temperature, T_e. From an initial estimate of $\bar{Z}^{Li}$ and $\bar{Z}^{Ag}$ and the atom number density, the electron number density, N_e is determined. T_e and N_e are then used to determine the rates for the individual rate matrices of each species. After solving for the populations of each species, $\bar{Z}^i$ of each individual species are obtained. The $\bar{Z}^i$'s of each element in conjunction with the abundances of each element and the total atom number density N_a a new N_e is computed and sent back to the singe element atomic kinetic models for the production of new $\bar{Z}^i$'s. This process continues until all the fractional populations of each level of each element varies no more than a set tolerance from the previous self-consistent iteration (see Figure 4.3). The time-dependent calculations proceed in a similar self-consistent manner, however, the initial level population for both T_e and N_a time-histories must be provided to perform the calculations. These time histories are usually provided through hydro-simulations.

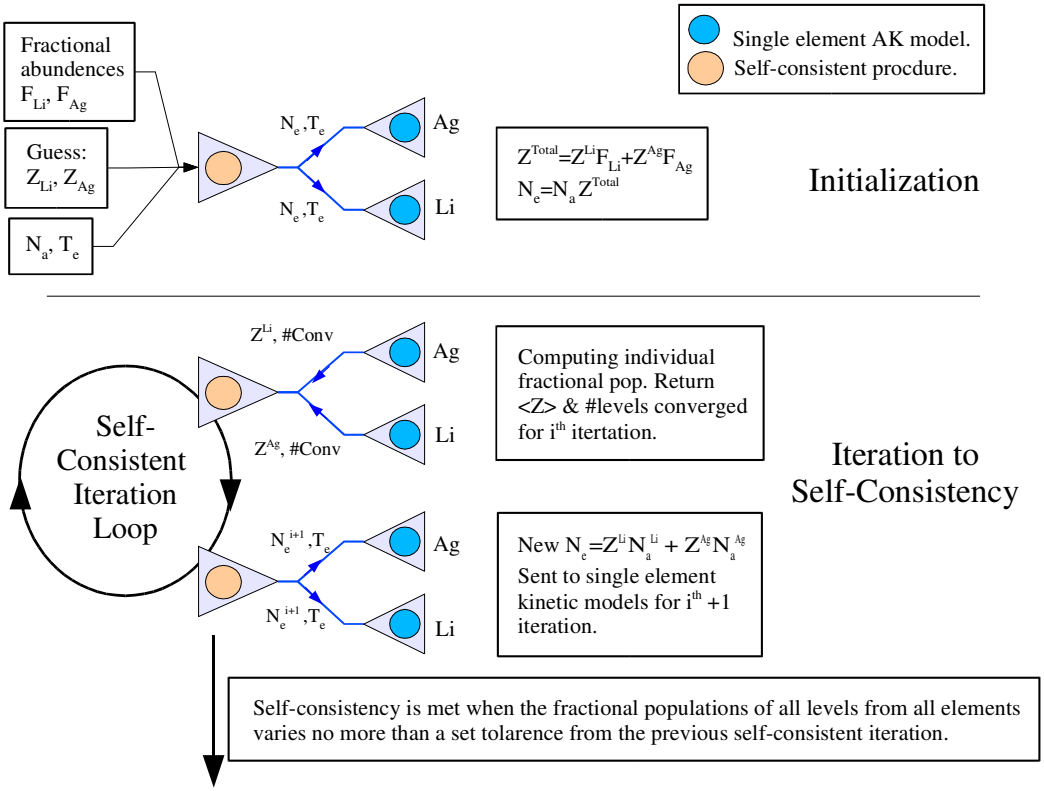

Figure 4.3: Multi-element atomic kinetic model schematic diagram.

4.4.1 Continuum Lowering

To account for non-ideal plasma effects on the atomic kinetics, an additional correction was included to determine the degree of continuum lowering, i.e. the lowering of the ionization potential due to the plasma environment and in turn the removal of bound excited states from the energy level structure. This effect of was approximated by the Stewart and Pyatt model [32]. The reduction in the ionization potential as a function of temperature and density requires an independent estimate of the average ionization stage. This was provided by an algorithm based on fitted and scaled results of the Thomas-Fermi model [33].

The removal of energy levels while in the process of calculating, self-consistently, fractional populations often leads to convergence issues[34]. This difficulty is avoided with the gradual removal of the energy level last affected by continuum lowering. This was done by multiplying the statistical weight of that level by a weight factor ranging from 1 to 0.

To account for the levels that are fully removed in the kinetic rate matrix, two methods were devised. The simplest procedure required replacing the rows and columns of the corresponding removed levels with zeros and replacing the diagonal element with unity. A second method required the actual removal and compression of the rate matrix. This technique led to a considerable increase in performance when a moderate number of levels were removed from a large model. This was due to the time gained in inverting a smaller matrix. However, when a small number of levels was removed, the zeroing procedure was found to perform faster due to its lack of overhead.

Chapter 5

Code Development and Parallel Implementation

5.1 Introduction

During the development of the multi-element and multi-spatial zone spectroscopic model, timings recorded for several execution trials indicated that a this computer program written in a serial form required an unacceptable amount of time to execute. Due to this fact a parallel implementation of the simulation code was pursed. For various technical reasons the program became too cumbersome to confidently perform modifications to include new physical effects though good programming practices were employed. This condition is unfortunately not uncommon when dealing with complex simulation programs. The solution would lead in a new direction of software development for this project. This chapter discusses the specific difficulties in dealing with complex simulation codes and draws from work done by the system developers community to describe a new methodology for constructing and implementing research simulation programs. As an example, this method is applied in the new spectroscopic code developed for this work . However, the underlining ideas are general and can be applied to other research codes as well.

5.2 Difficulties in Scientific Code Development

Several difficulties affect code development in scientific programming. The often short lived nature and highly changing aspect of most scientific programs produce a dilemma for the developer. Small programs are crafted in a temporary manner to test algorithms and methods to solve specific computational problems. In cases where a code's "lifetime" exceeds expectations, it becomes very difficult to incorporate it into larger simulation programs due to variable name conflicts, poor organization, non-robust implementation and a lack of consistent style. In regards to a pre-existing simulation program, additional complications arise when new projects are undertaken that require large modifications to the execution topology. It is impractical in most cases to place various options into a program in anticipation of future project requirements. Older simulation programs have the added difficulty of being overburdened with obsolete or unnecessary functionality for the project at hand and thereby complicating the adaptation procedure. Unfortunately, the removal of un-needed routines leads to a high probability of introducing errors into the program.

5.3 Microkernel implementation paradigm

For several years operating system developers have dealt with similar problems as those faced by computational physicists in regard to engineering software. From their work two predominant paradigms for operating system architectures or kernel architectures have emerged. The traditional monolithic kernels (typical of most UNIX operating systems and similar in form to most physics codes) are characterized as a collection of procedures typically compiled separately and linked into a single large

executable code. They are often implemented in a small number of layers. Protection, however, from the corruption of data (encapsulation) by other layers or procedures is non-existent. Interestingly, monolithic operating systems have noted examples were the complexity of the program grew to such an extent that the modifications needed to remove bugs led to the introduction of new bugs and to the eventual abandonment of the operating system [35].

The other kernel architecture is exemplified by the design of the microkernel. Here only a very small set of functions are included in the kernel. The remaining functionality needed by the operating system is included (i.e. memory management, file system services, etc.) as separate modules and are run as separate processes as needed. Interprocess communication between modules occurs through message passing. Though modules can communicate with each other, often for many operations the microkernel acts predominately as a centralized point of connection and communication[36].

To clarify the meaning of a modular implementation we must describe the qualities of a module. A module is allowed to depend only on the interfaces of other modules and not on their implementations. This quality immediately precludes the use of global variables between modules. Modules are designed to encompass a large element of functionality such as a memory subsystem. A purely modular implementation allows modules to interconnect freely with each other. This is in contrast to a layered model were connectivity is limited to elements "above" an "below" a given element [36].

Though operating systems based on a microkernel design are usually slower than the monolithic ones due to increased overhead of message passing they do possess many advantages that may be enlisted in dealing with software engineering problems

found in simulation codes. The microkernel structure forces system developers to employ functional components in a modularized manner since they are ran as separate processes. This will be one of the most important qualities exploited for this new method. Communication between processes only occurs through well-defined and clean software interfaces - requiring all transferring variables to be listed at the interface. This makes it easy to maintain, develop and replace modules without affecting the rest of the system. Moreover, message passing facilitates the creation of software where tasks can be distributed among several computers to lower overall execution times. One other positive feature of microkernel operating systems is their tendency to use random access memory (RAM) more efficiently than monolithic ones, since they have the capability to create or destroy processes (functionality) as the need arises. This is in contrast to the monolithic implementation where executable instructions and data of various functions remain in memory - even after they are needed - until execution is completed [37].

5.4 Implementing a Microkernel strategy.

Though the low level message passing primitive used in the microkernel design is not appropriate for scientific applications, the technique provides motivation for exploring the use of parallel message passing (PMP) libraries as a means of implementing a microkernel like strategy. In using a PMP libraries, application modules like the microkernel case run as separate processes and in turn separate memory address spaces - each processes is controlled and protected by the operating system. Pathological modules that access memory outside of their specified spaces cannot corrupt variables in other modules. This quality thereby reduces the time needed for diagnosing problems. Furthermore, in using PMP libraries, the execution of processes

is no longer limited to one machine. Inherently, two desirable conditions have been obtained - true modularity and parallel capability.

At this point the most drastic deviation from the microkernel design is made - the elimination of the central program from which modules are typically mounted (the microkernel itself). The removal of this hub like structure alleviated two technical difficulties: First was the need for adding variables and complexity to the central program simply to transport data from one module to another and secondly, in regard to a parallel implementation, to prevent a network bottleneck from occurring at the computer node that contained the central program. This modification facilitated a more peer style implementation where modules are connected to each other like Tinker-Toys and the program topology resembles the natural interconnections of the subject being modeled.

With the removal of a centralized data transferring module went a convenient process control center - Recall that the microkernel added and removed processes as needed to improve efficiency. To retain this feature a new hierarchical program structure was needed - An ordered multi-layer model was chosen where a process communicates only directly with members of its own layer or adjacent layers. Processes are spawned by the next higher-order parental layer. The removal of a process is signaled typically by its parent, or more rarely, by a module within its own layer.

In this structure constraints on the interconnectivity of a given module have led to an implementation that has characteristics of both modular and layered schemes. Though the implementation is far from ideal in regards to either scheme an important benefit has been gained: the employment of layers prevents overly complex program topologies that may have otherwise occurred in a purely modular design. As in any layered model, signals and to a lesser extent data must be passed through to target

modules residing deeper within the structure. Though this relaying of information from layer to layer may seem contrary to the original removal of the microkernel, it is noted that within each layer many modules are usually involved in the transporting of information and with modules deployed across many computer nodes the probability of a bottleneck is severely reduced.

As mentioned earlier PMP libraries are used to communicate between processes. Specifically, the Parallel Virtual Machine (PVM) libraries developed at Oak Ridge National Laboratories were used. To implement the layered structure of modules a new set of libraries referred to as the Workbench libraries was developed on top of the PVM libraries to assist in common tasks used in spawning and communicating between layer processes. The use of the Workbench libraries circumvents the main problem of using PMP libraries directly - Often, coding becomes tedious and programs become too cumbersome, in particular for a multi-layered program, when PMP libraries function calls are used directly in source code, thereby destroying the original intention for this development.

The Workbench library acts as a set of utilities built on the virtual machine presented by PVM much like UNIX utilities are built on top of the virtual machine presented by the UNIX kernel. These utilities transport data between modules without the requirement of specifying data type and in regards to arrays reduces significantly the number function calls to initialize a transfer. Furthermore these libraries maintain data structures for accessing processes, tasks and processes locations (computer node). In addition, functionality has been added to send information directly to layers for file I/O, thereby reducing the amount of data that must be relayed through

Table 5.1: Public module procedures of the multi-layer library.

Procedure	Arguments	Description
initp_info		Initializes parental information structure.
get_me		Returns label from an ordered list of the current process.
get_cmytid		Returns the PVM process id.
myinit		Receives parent level information for communication.
x_cque_c		Parallel queue send and received data from lower level processes.
x_rdat_c		Receives data from the adjacent child level.
x_rdat_p		Receives data from adjacent parental level.
x_rflg_p		Receives flag from parental processes.
x_rtids_p		Receives task id's from parental processes.
x_riflg_c		Receives flag from child processes.
x_riflg_p		Receives flag from parental processes.
x_sdat_c		Sends data to child adjacent processes.
x_sdat_p		Sends data to parental adjacent processes.
x_stids		Sends task id's to adjacent processes.
x_sflg_c		Sends flag to child level processes.
x_siflg_p		Sends initialization flag to parent processes.
x_skflg_c		Sends kill flag to child level processes.
openf		This is a driver routine used to open files in a location defined by a given system environment variable (envstring) with a given unit number (unitnum) with a file name (ctemp).
x_sp_c		Spawn child processes.
pk		Pack data and send to adjacent level.
upk		Unpack data from adjacent level.
destin		Sends data by direct or broadcast to target processes.
recv		Receives data from processes.

higher order layers. Table 5.1 lists multi-layer library procedures.

5.5 Application to Multi-element Atomic Kinetic Modeling.

The techniques of the above development scheme are applied to the spectroscopic model discussed in Chapter 4, in particular, to the highest density case - occurring early in time and close to the target surface. Included in this model is the capability of calculating a gradient in the direction along the line-of-sight of the spectrometer. The existence of this gradient was discussed in Chapter 2, in regards to the experimentally observed self-reversal feature in the Li: 3d-2p lineshape. To accommodate a gradient, the theoretical plasma is divided into zones - each containing the same abundances of each species but each described by a unique temperature and atom number density. For this plasma environment, optical depths are large, thereby requiring a separate calculation for the radiation transported through the different zones. The radiation from one zone does not, in this plasma, affect the population of another - the justification for this assumption will be discussed in a Chapter 6. From this assumption the atomic kinetics of each zone is left uncoupled and can be calculated independently. From these qualities a three layer model can effectively be constructed.

It should be re-emphasized here before going any further that the modular framework is simply a framework. Except for the amount of data transferred between processes and for the the topology of the implementation, the modules are independent from the physics codes embedded into them. Or in other words the modular framework constitutes a software network that the physics codes communicate through.

The lowest layer modules (Layer IV) contains a set of single element kinetic models (SEKM) that compute the populations of each element found in a particular

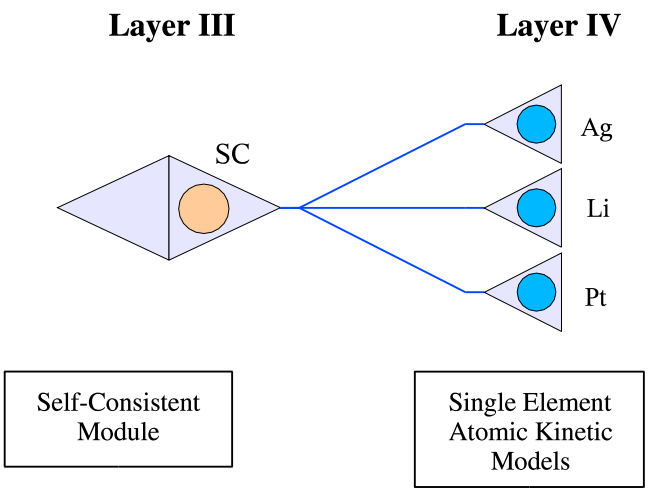

Figure 5.1: Single plasma zone multi-element atomic kinetic object [Layers III and IV] are shown. In this diagram, the circles represents the physics models while the triangles represent the communication interface of the Workshop libraries. Triangles pointing to the right have spawning capabilities and have spawned the processes to their right.

zone of the plasma. The next higher layer of modules, the parental layer (Layer III) of the lowest layers, contains the self-consistency routines (SC) that check the multi-element kinetic calculation for completion (see Figure 5.1).

Once a self-consistent solution is obtained, the SC layer then signals the SEKM for emissivity and opacity data that is then relayed to the next higher layer - the radiation transport layer (Layer II). Here, data from each zone is accumulated and used to generate the synthetic spectra for one complete plasma. It is also here where experimental lineouts and the theoretically created spectra are compared (see Figure 5.2). Layers II-IV represent the synthetic spectral object (SSO).

The comparison of the experimental data to synthetic spectra is done in an au-

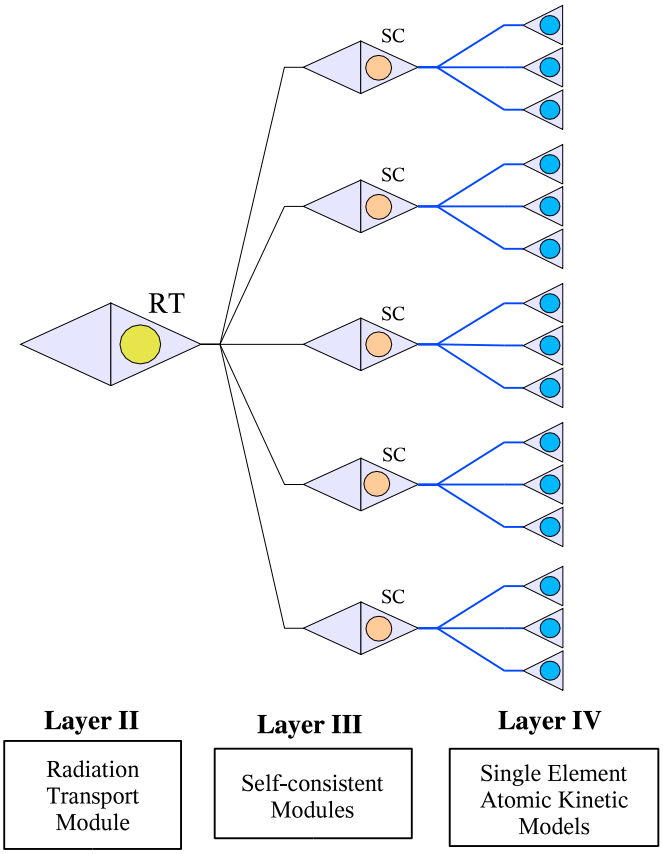

Figure 5.2: Synthetic spectral object involving five plasma zones [Layers II, III and IV] are shown. In this diagram, the circles represents the physics models while the triangles represent the communication interface of the Workshop libraries. Triangles pointing to the right have spawning capabilities and have spawned the processes to their right.

tomated manner by the use of a search engine. The search engine typically generates a large number of temperature and density profiles for which the physics model must produce a quantitative comparison between theoretical and experimental spectra. The temperature and density profile generated by the search engine is stored in a parallel queue (PQ). Initially, PQ spawns several synthetic spectral objects that load atomic and spectral data and then wait ready to generate synthetic spectra from the profiles dispensed from the PQ. The search engine, in search for the best synthetic to experimental spectral fit, generates thousands of profiles. Once the search is complete, PQ sends termination signals to each SSO. In each SSO a signal is related to the deepest layer where termination first begins. Termination continues to propagate up until all the SSOs are destroyed Figure 5.3.

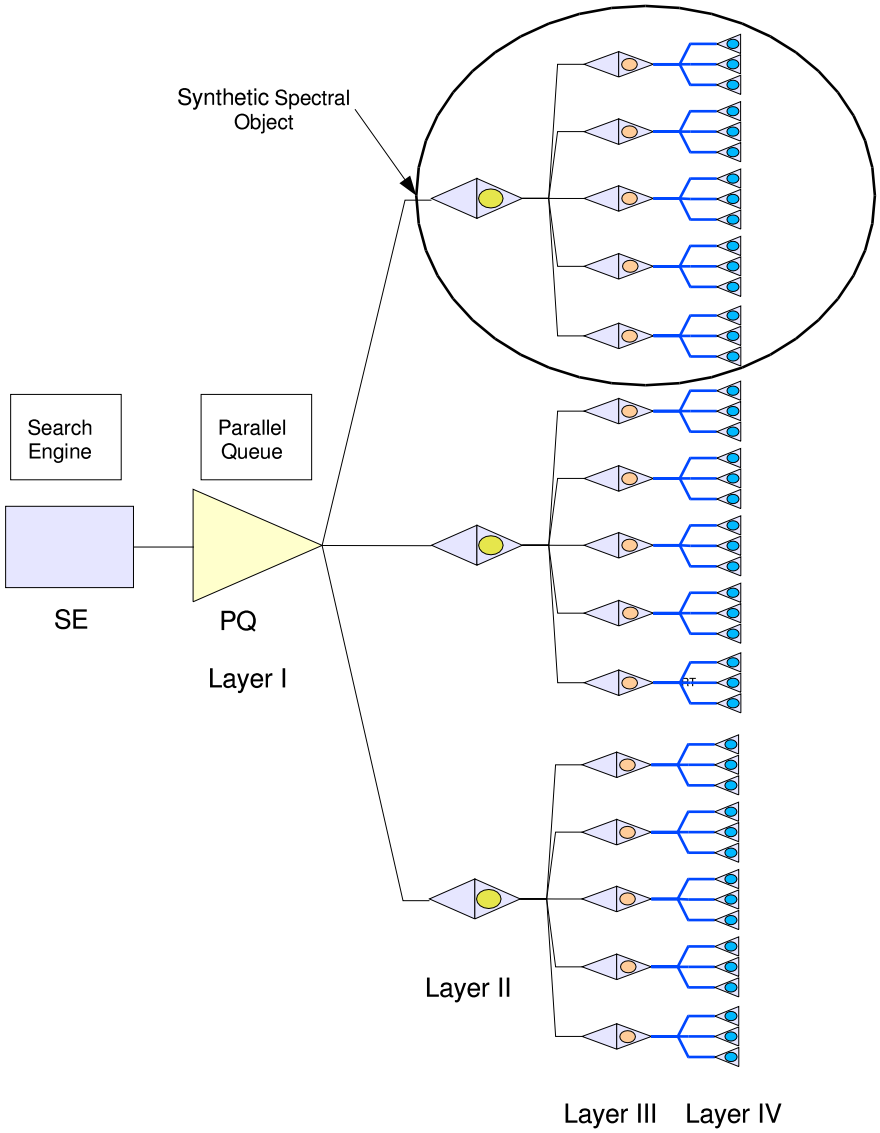

Figure 5.3: Diagram showing the communication of the parallel queue with three concurrent plasma spectral models (synthetic spectral objects). Layers I-IV are shown. The plasma executables remain in memory processing jobs until the parallel queue (PQ) is empty.

Chapter 6

Synthetic Spectra Calculations

6.1 Introduction

Line emission produced in an ablation plasma is altered from the ideal by two distinct mechanisms: first, by the influence of the plasma microfield on the radiator, i.e. charged and neutral particles distort the radiator's atomic potential, and in turn, shifts its energy levels, leading to the characteristic broadening of the line profile; secondly, by the influence of the plasma opacity (line emission produced deep in a plasma must propagate through many plasma layers before escaping). Since photons at the center of the line emission are more efficiently absorbed than those in the wings, the line intensity distribution is distorted by the effects of radiation transport. These two effects must be taken into account when calculating synthetic spectra.

6.2 Line Profile Calculations

In this section, the line profile calculations of Li and Ag lines observed in the experimental spectra are discussed. Figures 6.1 and 6.2 display Stark-broadened line profiles for the Li 3d-2p and two main Ag lines observed in the experimental spectra. The effect of the ions was calculated in the static ion approximation while that of the electrons was computed using a quantum-mechanical second-order relaxation theory [38],[39]. The ion microfield distribution function was computed (and cross-checked for consistency) using both the APEX [40] and Tighe and Hooper models [41]. Since the energy separation between upper and lower energy level manifolds associated with these line transitions is not very large compared with the spread in energy within the manifolds, the usual non-quenching approximation was removed and full mixing between upper and lower manifolds by plasma microfields was included. Thus, for the Li line shapes mixing between fine structure levels associated with $1s^2 2l$, $1s^2 3l$, $1s^2 4l$ and $1s^2 5l$ configuration was taken into account, and for the Ag line profiles $4d^{10}7s$, $4d^{10}6s$, $4d^{10}5s$, $4d^{10}7p$, $4d^{10}6p$, $4d^{10}5p$, $4d^{10}6d$, $4d^{10}5d$, $4d^{9}5s^2$, and $4d^{10}4f$ were included.

6.3 Detailed Line Profiles

The appearence of weak forbidden lines in the computed profiles is the result of plasma micro-field mixing of energy levels. Like configuration interaction, field mixing affects those energy levels that lie closest together. However, unlike configuration interaction plasma micro-field mixes energy levels of opposite parity, in turn eliminating the total angular momentum and parity as a good quantum numbers. Though these features are often small, they have the potential of being observed since they often reside on the wings of larger spectral features and are not diminished by opacity effects of the

bulk plasma (see Figure 6.3).

An asymmetry in the series of profiles from low to high electron density may develop as seen in the lithium 3d-2p profiles (Figure 6.1). The effect of this quality can be seen in the final synthetic spectrum. In figure 6.2 the two $5d-5p$ fine structure splitting spectral features of neutral silver are shown. These two are folded into a single profile. Included in the relative heights of this profile is an assumption of the relative populations of the upper levels. Due to the proximity in energy of the two upper levels to each other and the effect of collisions to thermalize these levels, we have assumed for the sake of generating this lineshape that the ratio of their populations should follow from the ratio of their statistical weights.

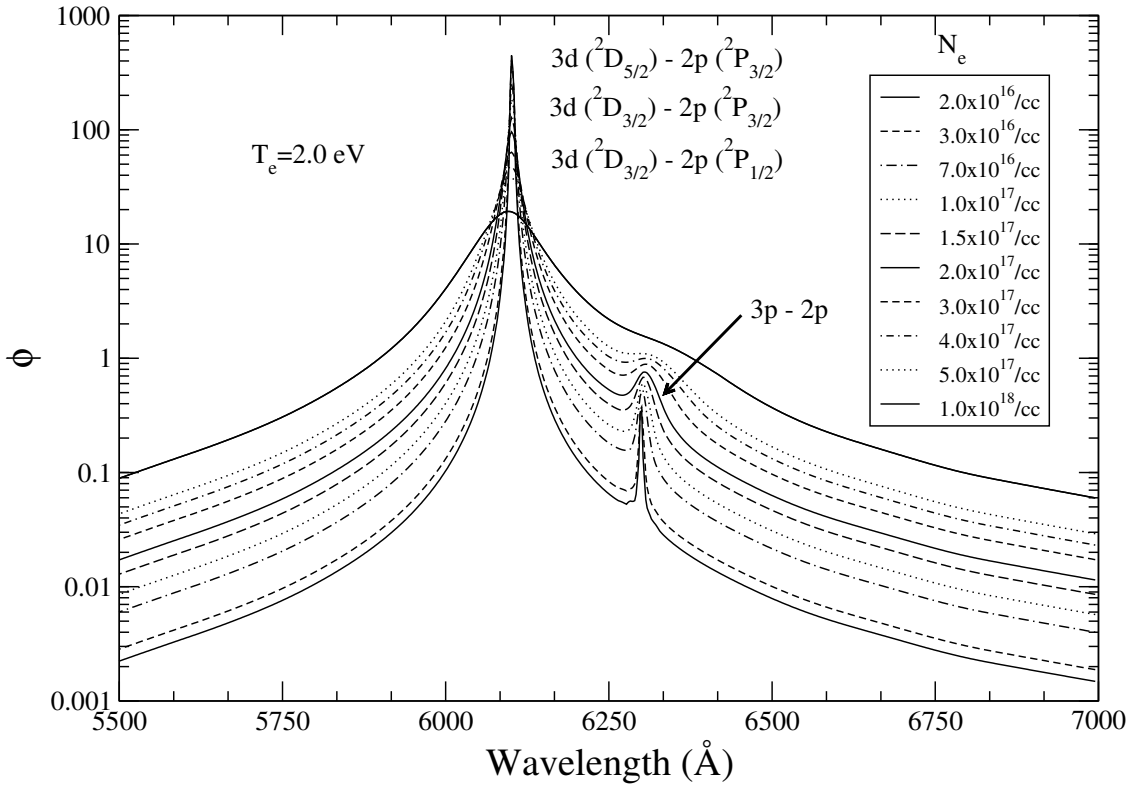

Figure 6.1: Neutral lithium line profiles at various plasma electron densities for the dominant $3d - 2p$ transition . Plasma microfield mixing of $1s^2 3p$ with $1s^2 3d$ energy level wavefunctions enhances the $1s^2 3p$ transition probablity to the $1s^2 2p$ state thereby producing the otherwise forbidden feature. Electron densities N_e are in cm^{-3}.

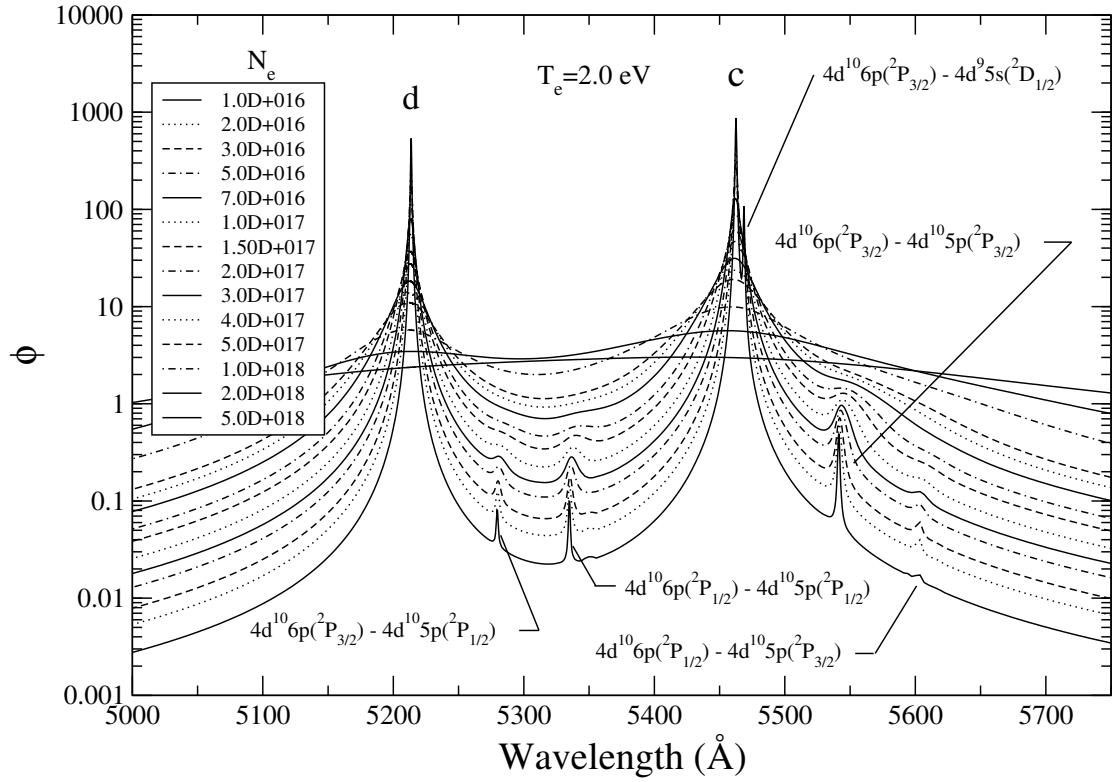

Figure 6.2: Neutral silver line profiles for various plasma electron densities with the two dominant $5d - 5p$ fine structure transition. Plasma microfield mixing of $4d^{10}6p$ with $4d^{10}5d$ energy level wavefunctions enhances the $4d^{10}6p$ transition probablity to the $4d^{10}5p$ states, thereby producing the four small forbidden features. Also the low probablity $4d^{10}6p$-$4d^{9}5s$; $2e^{-}$ transition is present on the low energy side of line **c**. Electron densities N_e are in cm^{-3}.

6.4 Solving the Radiation Transport Equation

In the ablation plasma under study, early in time and close to the surface, the optical depth at the center of the emission line can be quite large ($\tau \backsimeq 400$). This type of opacity requires a numerically stable solution to the radiation transport equation.

The transport of radiation in slab geometry is described by the following equation:

$$\mu \frac{dI_{\nu\mu}}{dz} = -k_\nu(z) I_{\nu\mu}(z) + j_\nu(z), \quad \mu = cos\theta, \tag{6.1}$$

where the spectral intensity I_ν between ν and $d\nu$ is measured in units of [ergs $\cdot$ sec$^{-1}\cdot$ cm$^{-2}\cdot$ steradians$^{-1}\cdot$ Hz^{-1}]; j_ν in units of [ergs $\cdot$ sec$^{-1}\cdot$ cm$^{-3}\cdot$ steradians$^{-1}\cdot$ Hz^{-1}] and k_ν in units of [cm^{-1}]; j_ν and k_ν are the spectral emission coefficient and spectral linear absorption coefficient (opacity), respectively. Consider a transition between an upper level i and a lower level k. Then, the spectral emissivity may be written as,

$$j_\nu = \sum_{i=1}^{n_l} \sum_{k<i} n_i A_{ik} \{\phi_{ik}\}_\nu \frac{h\nu_{ik}^0}{4\pi} \tag{6.2}$$

where A_{ik} is the spontaneous radiative decay in units of [sec^{-1}], n_i particle number density [cm^{-3}] and ϕ_{ik} [Hz^{-1}] is the line profile associated with the i to j transition and satisfies the normalization condition $\int \phi_{ik}\ \mathrm{d}\nu = 1$. The opacity maybe written as,

$$k_\nu = \sum_{i=1}^{n_l} \sum_{k>i} (n_i B_{ik} - n_k B_{ki}) \{\phi_{ik}\}_\nu \frac{h\nu_{ik}^0}{4\pi} \tag{6.3}$$

where both B_{ik} the stimulated emission coefficient, and B_{ki} the photo-absorption coefficent have units of [cm$^2\cdot$ ergs$^{-1}\cdot$ Hz]. To simplify the radiation transport equation the following substitutions are made, $z' = z/\mu$, $dz' = dz/\mu$. Then Eq.(6.1) may be written as

$$\frac{dI_{\nu\mu}}{dz'} = -k_\nu(z') I_{\nu\mu}(z') + j_\nu(z') \tag{6.4}$$

Eq.(6.4) is a first order ordinary differential equation of the form

$$\frac{dy}{dx} = -p(x)y + q(x) \tag{6.5}$$

Whose general solution can be written as follows [42],

$$y(x) = y(x_o)\exp\left(-\int_{x_o}^{x} p(t)dt\right) + \frac{\exp\left(-\int_{x_o}^{x} p(t)dt\right)}{\alpha(x_o)} \cdot \\ \cdot \int_{x_o}^{x} \alpha(t_o)\exp\left(\int_{t_o}^{t} p(t')dt'\right) q(t)dt. \tag{6.6}$$

Where $\alpha(x)$ is a suitable integrating factor. Setting $x_o = 0$ and in turn $t_o = 0$, i.e. beginning the integration for the radiation transport equation from the far end boundary of the plasma

$$y(x) = y(0)\exp\left(-\int_{0}^{x} p(t)dt\right) + \frac{\exp\left(-\int_{0}^{x} p(t)dt\right)}{\alpha(0)} \cdot \\ \cdot \int_{0}^{x} \alpha(0)\exp\left(\int_{0}^{t} p(t')dt'\right) q(t)dt. \tag{6.7}$$

Note that the $\alpha(0)$ cancel each other in the second term thus resulting in

$$y(x) = y(0)\exp\left(-\int_{0}^{x} p(t)dt\right) + \exp\left(-\int_{0}^{x} p(t)dt\right) \cdot \\ \cdot \int_{0}^{x} \exp\left(\int_{0}^{t} p(t')dt'\right) q(t)dt. \tag{6.8}$$

Finally, substituting the physical quantities into Eq. (6.8)

$$I_{\nu\mu}(z') = I(0)\exp\left(-\int_{0}^{z'} k_\nu(t)dt\right) + \exp\left(-\int_{0}^{z'} k_\nu(t)dt\right) \cdot \\ \cdot \int_{0}^{z'} \exp\left(\int_{0}^{t} k_\nu(t')dt'\right) j_\nu(t)dt. \tag{6.9}$$

For a non-backlit plasma $I_{\nu\mu}(0) = 0$. Substituting this condition into Eq.(6.9), only the second term in the equation remains,

$$I_{\nu\mu}(z') = \exp\left(-\int_{0}^{z'} k_\nu(t)dt\right) \cdot \int_{0}^{z'} \exp\left(\int_{0}^{t} k_\nu(t')dt'\right) j_\nu(t)dt. \tag{6.10}$$

This form of the solution of the radiation transport equation is not easy to interpret; however, with a small amount of manipulation a simpler form can be obtained. Though the solution of the intensity $I_{\nu\mu}$ is currently general with respect to z', the spectrum recorded by a spectrometer would correspond to the solution at the plasma boundary $z' = L$,

$$I_{\nu\mu}(L) = \exp\left(-\int_0^L k_\nu(t)dt\right) \cdot \int_0^L \exp\left(\int_0^t k_\nu(t')dt'\right) j_\nu(t)dt. \tag{6.11}$$

Next, consider

$$\int_0^L f(x)dx = \int_0^t f(x)dx + \int_t^L f(x)dx \tag{6.12}$$

and

$$\int_0^t f(x)dx = \int_0^L f(x)dx - \int_t^L f(x)dx \tag{6.13}$$

and employ the relation $\int_0^t k_\nu(t')dt'$ to obtain

$$I_{\nu\mu}(L) = \exp\left(-\int_0^L k_\nu(t)dt\right) \cdot \int_0^L \exp\left(\underbrace{\int_0^L k_\nu(t')dt'}_{\zeta} - \int_t^L k_\nu(t')dt'\right) \cdot$$
$$\cdot\, j_\nu(t)dt. \tag{6.14}$$

The value of the integral maked by ζ is independent of t so $\exp(\zeta)$ can be moved outside of the integral to cancel with the first term in the product; leaving

$$I_{\nu\mu}(L) = \int_0^L \exp\left(-\int_t^L k_\nu(t')dt'\right) j_\nu(t)dt. \tag{6.15}$$

Finally, define the optical depth $\tau(t) = \int_t^L k_\nu(t')dt'$ to obtain

$$I_{\nu\mu}(L) = \int_0^L \exp\left(-\tau(t)\right) j_\nu(t)dt. \tag{6.16}$$

The integrand of Eq.(6.15) states that the contribution of the intensity seen outside of the plasma at L, for a spectral frequency between ν and $\nu + d\nu$, produced in the region of the plasma between t and $t + dt$; is equal to the attenuation

$(\exp\left(-\int_t^L k_\nu(t')dt'\right))$ by the plasma from t to L of radiation produced in that region $(j_\nu(t))$. The total intensity is simply the sum of all these contributions. The temptation at this point is to calculate this integral with a Gaussian quadrature technique such as Gauss-Legendre integration. This type of integrand, in general, is not appropriate for such a method since the integrand is not in the form of a polynomial but an infinite series. The exception, however, occurs when the absolute value of the argument of the exponent is less than unity, then the exponential function may be approximated by a polynomial. This occurs when the optical depth τ of the plasma is low. This unfortunately is not the case.

To solve for $I_{\nu\mu}(L)$, we propose discretizing the outer integral of Eq. (6.16) as follows

$$I_{\nu\mu}(L) = \sum_{i=1}^{N} \int_{t_i}^{t_{i+1}} \exp\left(-\tau_i(t)\right) j_{\nu i}(t)dt \tag{6.17}$$

If the spatial discretization is fine enough, both the emissivity and the optical depth may be considered linear within a particular discretization zone. Recall, a discretization of the plasma has already been performed to generate gradients in temperature and density along the line-of-sight of the spectrometer. Therefore, a natural grid already exists, and Eq. (6.17) can be written as

$$I_{\nu\mu}(L) = \sum_{i=1}^{N} \int_{t_i}^{t_{i+1}} \exp\left(-\left(\alpha_i' + \beta_i' t\right)_{\tau,\nu}\right) \left(a_i + b_i t\right)_{j,\nu} dt \tag{6.18}$$

Caution, however, must be used since the values given for $j_\nu' s$ and $k_\nu' s$ from the kinetic model should be considered at zone center. The zone center $k_\nu' s$ are conveniently located for the integration needed to determination of the optical depth (τ). This will produce a solution for τ at the zone boundaries. Then, the evaluations of the slope (β) and y-intercept (α) of each zone are performed. To determine the slope

(a) and y-intercept (b) from the $j'_\nu s$, the value of j_ν at the zone boundaries must be determined first by interpolation. At this point, the integrals of Eq.(6.18) can be evaluated analytically (we also let $\alpha = -\alpha'$ and $\beta = -\beta'$) to obtain,

$$I_{\nu\mu}(L) = \sum_{i=1}^{N} \left[\frac{a_i \exp(\alpha_i)}{\beta_i} \cdot (\exp(\beta_i x_i) - \exp(\beta_i x_{i+1})) \right] +$$
$$+ \sum_{i=1}^{N} \left[\frac{b_i \exp(\alpha_i)}{\beta_i} \cdot \left(\exp(\beta_i x_{i+1}) \left(x_{i+1} - \frac{1}{\beta_i} \right) - \right. \right.$$
$$\left. \left. - \exp(\beta_i x_i) \left(x_i - \frac{1}{\beta_i} \right) \right) \right]. \tag{6.19}$$

Due to problems in evaluating the terms $\exp(\beta_i x_{i+1})$ and $\exp(\beta_i x_i)$ numerically, Eq.(6.19) should be rewritten in a more benign form,

$$I_{\nu\mu}(L) = \sum_{i=1}^{N} \left[\frac{a_i \exp(\alpha_i + \beta_i x_i)}{\beta_i} \cdot (1 - \exp(\beta_i (x_{i-1} - x_i)) \right] +$$
$$+ \sum_{i=1}^{N} \left[\frac{b_i \exp(\alpha_i + \beta_i x_i)}{\beta_i^2} \cdot ((\beta_i x_i - 1) - \right.$$
$$\left. - (\beta_i x_{i-1} - 1) \exp(\beta_i (x_{i-1} - x_i))) \right]. \tag{6.20}$$

Finally, in this development for the numerical solution of the radiation transport equation, the $\lim_{\beta \to 0} \{I_{\nu\mu}\}_i$ of Eq.(6.20) must be examined. For small values of the argument, the exponential function can be expanded in a power series to first order thus resulting in the following two terms:

$$\lim_{\beta \to 0} \sum_{i=1}^{N} \left[\frac{a_i e^{(\alpha_i + \beta_i x_i)}}{\beta_i} \cdot \left(1 - e^{(\beta_i (x_{i-1} - x_i))} \right) \right] = (x_i - x_{i-1}) \tag{6.21}$$

$$\lim_{\beta \to 0} \sum_{i=1}^{N} \left[\frac{b_i e^{(\alpha_i + \beta_i x_i)}}{\beta_i^2} \cdot \left((\beta_i x_i - 1) - (\beta_i x_{i-1} - 1) e^{(\beta_i (x_{i-1} - x_i))} \right) \right] = 0. \tag{6.22}$$

To maintain numerical stability, a conditional is employed to calculate the partial contribution of zone i to the total intensity for the specific case $\beta = 0$,

$$\int_{t_{i-1}}^{t_i} (a_i + b_i t) \cdot \exp(\alpha_i + \beta_i t) dt = a_i (x_i - x_{i-1}) \cdot \exp(\alpha_i) \tag{6.23}$$

This development represents a robust numerical solution for the radiation transport equation.

6.5 Results of the Radiation Transport Equation

This section discusses the results of the solution to the radiation transport equation for the case of a uniform slab. Figure 6.3 shows the results of a ten zone calculation where each zone has been assigned T_e=0.7 eV and a N_a= 1.0×10^{17} cm^3. The corresponding analytical solution is

$$I = \frac{j_\mu}{k_\mu}(1 - \exp(-k_\mu \cdot L)), \tag{6.24}$$

where L is the thickness of the plasma. Comparison of the two solutions are identical, even to the largest optical depths at line center of τ=10,000-100,000 as seen in Figure 6.4. We should note, that a spectral feature of optical depth $\tau < 1$ is considered optically thin. Figure 6.3 describes the evolution of spectral lines undergoing self-absorption as their line centers become more optical thick due to an increasing slab thickness. At the largest optical thickness, individual line features are no longer present and the intensity approximates the Planck functions. Note that since the density and temperature remain constant the line profiles are constant as well.

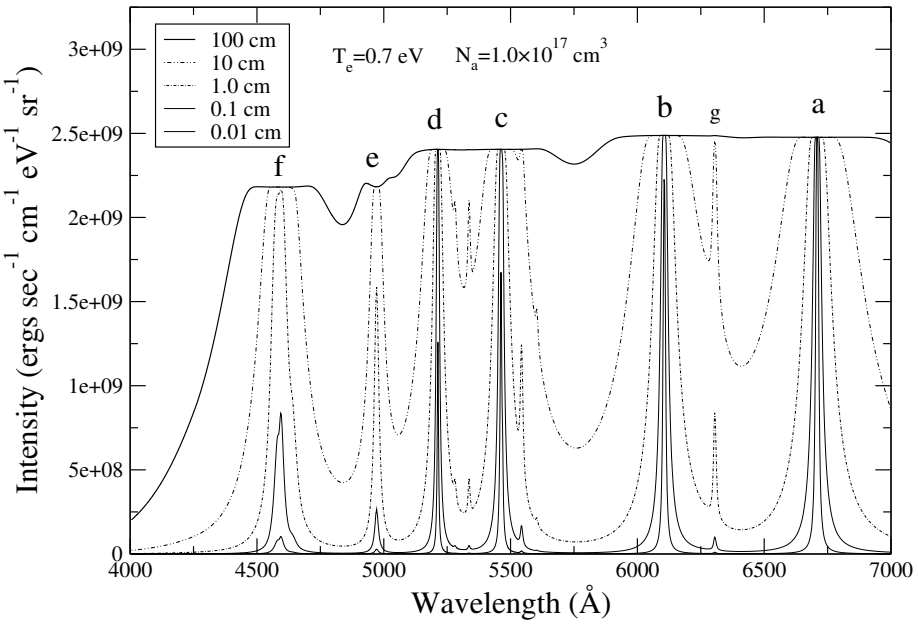

Figure 6.3: A series of synthetic spectra generated for various plasma thicknesses. Ten identical zones of the same electron temperature and atom number density were used and compared with the analytic solution to the homogenous slab problem. The results are indistinguishable in the graph.

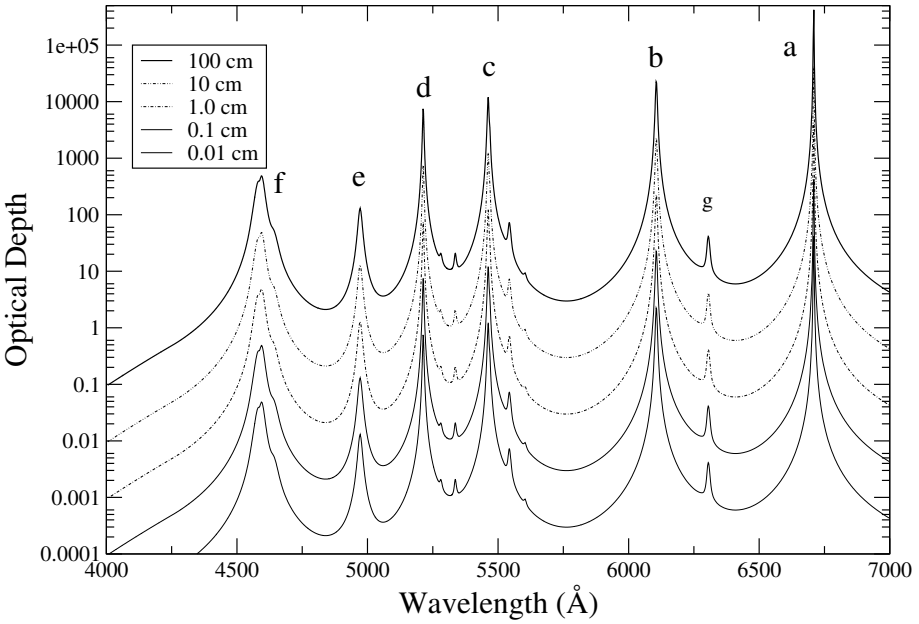

Figure 6.4: Corresponding optical depths for the above series of uniform, ten zone calculations.

6.5.1 Non-Homogenous Spectral Grid

In order to resolve the peaks of the sharpest line profiles, profile calculations are performed on their own unique grid. A series of ever narrower, regions with increasing mesh densities about the peak of the line profile, are produced until the desired resolution is met. This insures the proper characterization, as well as normalization for the sharpest line profiles. Line profiles must span the full spectral range of interest. The overlaping of lines is to be expected, and a common high resolution grid across the entire spectral range for all the spectral features (for the purpose of calculating the radiation transport) would be very computationally inefficient. Therefore a non-uniform grid was implemented. It was defined by the densest profile grid found at each point along the spectral range Figure 6.5. This grid cannot be determined a priori, but is determined by adding one lineshape at a time. Once the grid points have been determined, every member of the set of line profiles for each line feature must be interpolated to adhere to the new custom mesh. Any improvement in resolution or the inclusion of any line profile requires a new regeneration of the common mesh and reinterpolation of all the profiles. Currently, 4023 points are used to describe the spectra where 1000 points are used soley to describe the 5d-5p line features.

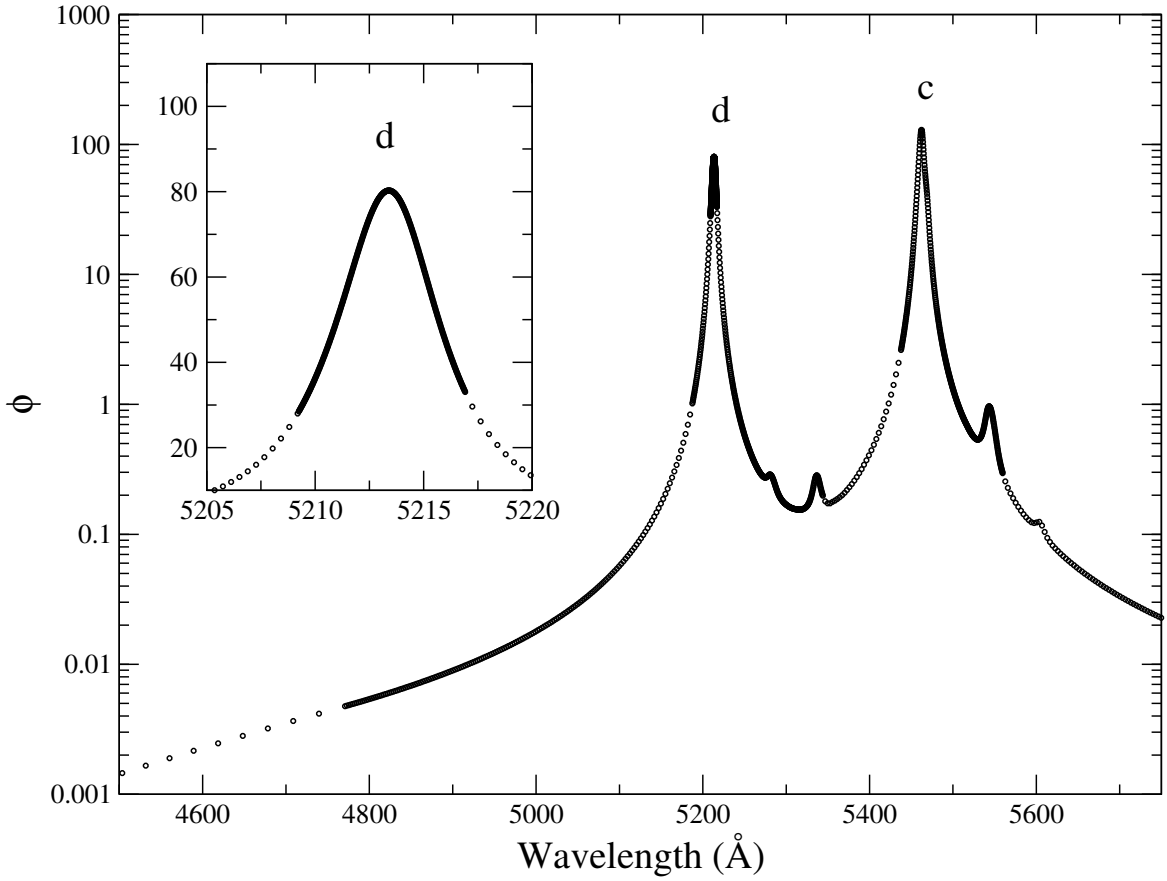

Figure 6.5: A non-uniform grid provides resolution of rapidly changing features and insures proper normalization of the line profile for this neutral silver line shape. Such a grid, though more complicated to employ, saves on valuable execution time during the radiation transport phase of the simulation.

6.5.2 Instrumental Broadening

To predict the temperature and density of the Li-Ag plasma, a final comparison between the synthetic spectra and experimental spectra are required. The effect of the finite resolution of a spectrometer is the broadening of spectral features. Typically, this is accounted for by the convolution of each point in the spectra and its vicinity with a normalized Gaussian profile where the width corresponds to the spectral resolution of the instrument. From Figure 6.6, the typical effect of the instrumental broadening (IB) on the synthetic spectra is shown. The sharp features and structures on the top of the narrowest lines are broadened and reduced. The self-reversal feature of the Li I: 3d-2p line has nearly been removed altogether, while small broader features, such as feature **f** and the small Li I: 2p-3p transition (**g**), show little effect. The diminishment of features, such as the self-reversal and broadening of peaks, desensitizes the spectra to opacity and non-uniformity, making the comparison and therefore the determination of plasma conditions more ambiguous.

A least squares minimization procedure was used to quantitatively compare the experimental spectra to the synthetic spectra. In an early attempt to reduce computational overhead all experimental data was interpolated to the theoretical spectral mesh. This was done only once for experimental lineouts. Unfortunately, due to the inhomogeneity of the theoretical mesh and the least squares method to naturally emphasize data points and not features, spectral lines such as the Ag I: 5d-5p were disproportionally fitted at the cost of the other spectral lines (see previous section). The final solution required that each theoretical spectral feature be interpolated to the experimental grid. As a practical note, a uniform grid may not always be ideal in the interpretation of an experimental lineout. It may be known a priori that the

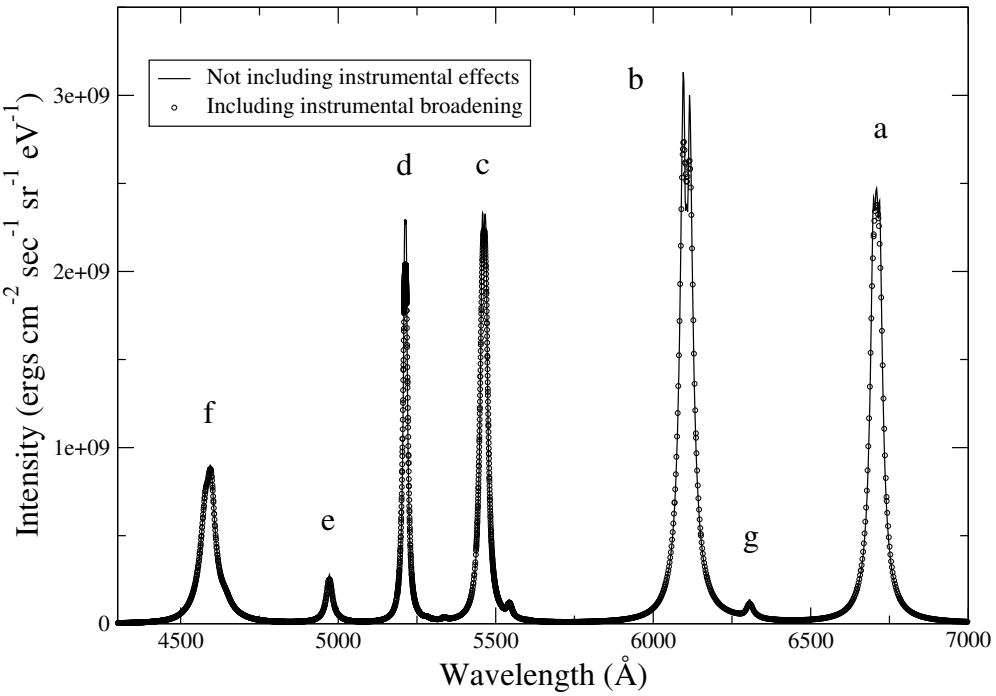

Figure 6.6: Effects of Instrumental Broading on Synthetic Spectra

ratio of intensities of particular lines may be a sensitive diagnostic for temperature. Broader lines with more points will be weighted more than narrower lines, thereby reducing the emphasis given to the temperature sensitive lines. Along a similar line, a large number of points may exist between line features that may be noisy and provide very little information about the spectra as in our case. Points in the noise dominated regions between main features have been removed in the evaluation of the least squares minimization procedure to improve the comparison for the diagnostic.

6.6 Synthetic Spectra Sensitivity in the Uniform Steady State High Density Regime.

This section describes the sensitivity of the synthetic spectra for a plasma uniform in temperature and density. For this section, and for the rest of this work, uniform is understood as strictly uniform: a plasma where the level populations are identical throughout its spatial extent. This is an approximation to a plasma in slab geometry, where a plasma with a uniform electron density T_e and atom number density N_a may have varying level populations due to the effect of a non-uniform radiation field that occurs near the slab boundaries.

To characterize the state of the plasma, a useful spectral region, or for that matter, a dopant added to a plasma as a diagnostic must have spectral features sensitive to both density and temperature. Often a spectral range is chosen to include multiple ionization stages to improve, in particular, the temperature sensitivity, since an increase in temperature drives both population shifts within atoms and in the ionization balance. Here unfortunately, the line emission of only one ionization stage of either Li or Ag can be clearly discerned. We should note that some Ag II lines do have their transition energy within the visible range; however, these lines occur in high n-states with very little population in the upper level of the transition. This produces very weak lines that cannot be confidently discerned from the background noise. For the case of Li II, the high transition energy from ground to the first excited state prevents any subtantial population to energy levels whose transitions to lower states can be seen in the visible range. See Chapter 4 for a compete description.

6.6.1 Spectral sensitivity under constant electron density.

Figure 6.7 contains a series of spectra generated with a fixed electron number density of $N_e = 2.0 \times 10^{17} cm^3$ and a decreasing series of temperatures - beginning with $T_e = 2.0$ eV and gradually reduced by $\Delta T_e = 0.2$ eV. A constant electron density N_e was chosen to eliminate the variations of the emission lines due to changing profiles. Furthermore, a constant N_e reduces the variation in the atomic rates, and in turn, the fractional populations by allowing the rates to vary only by temperature through the rate coefficients. Variation in the atom number density, an outcome of leaving the electron density constant, only affects the absolute and not the relative intensity of an ideal optically thin plasma. The predominant quality seen in these series of plots is the evolution of the heights of Ag lines to a nearly stationary set of Li lines. These spectral characteristics are the effect of both atomic kinetics and opacity.

The behavior of the spectral lines can in part be explained as the effect of the interplay of the two vastly different atomic structures of Li and Ag. The decrease in the magnitude, relative to the Li lines, of the Ag I: ($4d^{10}5d^2$–$4d^{10}5p^2$) lines is the effect of the increase in temperature driving a shift in population to the higher ionization stages of Ag. The persistence of the Li I: ($1s_2 3d$–$1s_2 2p$) and ($1s_2 2p$–$1s_2 2s$) lines arises from the high (60.9 eV) transition energy to the first excited state of Li^{1+}.

Due to sharp spectral features of Figure 6.7, the presence of opacity is not obvious. Figure 6.8 describes the optical depth associated with each synthetic spectrum of Figure 6.7. An overall increase in optical depth is seen to be correlated with a decrease in temperature. This is due to the increase in the total number of absorbers N_a needed to maintain a constant N_e. See Eq.(6.25) for the functional dependencies of the optical depth τ, where F_i is the fractional population of the lower level, ΔR is

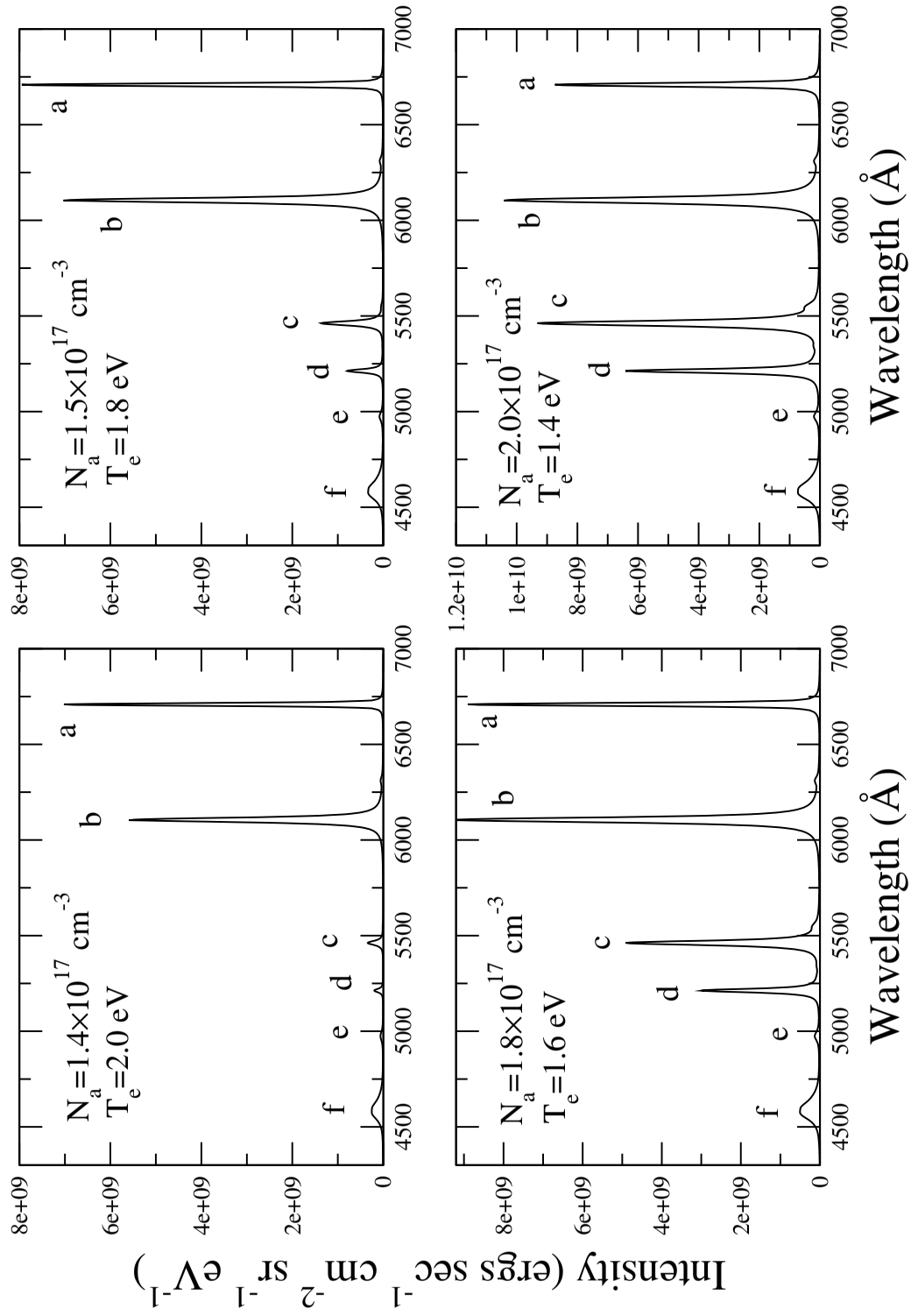

Figure 6.7: The effects of temperature on spectra under constant electron density $N_e = 2.0 \times 10^{17}$ cm^{-3}. Labels indentifying spectral lines are defined in Table 2.4.

a characteristic length, and $f_{i,j}$ is the oscillator strength between the lower level i to the upper level j.

$$\tau_\nu = \frac{\pi e^2}{mc}\phi_\nu f_{i,j} F_i N_a \Delta R \tag{6.25}$$

Furthermore, an obvious lack of uniformity in optical depth is seen across the spectrum with a variation of depths as large $\Delta\tau$=10 between the Li and Ag lines in the spectrum. The effects of opacity on the spectrum can readily be seen in Figure 6.9. Spectra of Figure 6.7 are superimposed on spectra generated with the same T_e and N_e, but with the effects of opacity removed.

Opacity reduces the sensitivity of a spectral feature to plasma conditions. This is readily seen in the case of the Li I 2p-2s and 3d-2p transitions. A large relative change between the two lines occurs from the T_e=2.0 - 1.4 eV plots for the optically thin spectra, while the optically thick spectra remain relatively unchanged, thus rendering the lithium lines by themselves useless as a diagnostic. The opacity effects in the case of the Li I 2p-2s line are so extreme in fact that it becomes less dominant than the 3d-2p. Ironically, the weaker Ag lines with their low opacity show the greatest sensitivity for the optically thick system; however, they alone cannot be used as a diagnostic since their relative intensities (ignoring the effects of opacity) are fixed. This is due to the very small difference in energy of the two upper 5d fine structure split levels where the ratio of their populations is simply the ratio of their statistical weights. However, with the Li lines as a reference in conjunction with the Ag lines, a good diagnostic is available at least for temperature. One final note, interestingly, is that the Ag lines in the T_e=1.4 eV plot begin to loose sensitivity due to opacity as their intensity grows.

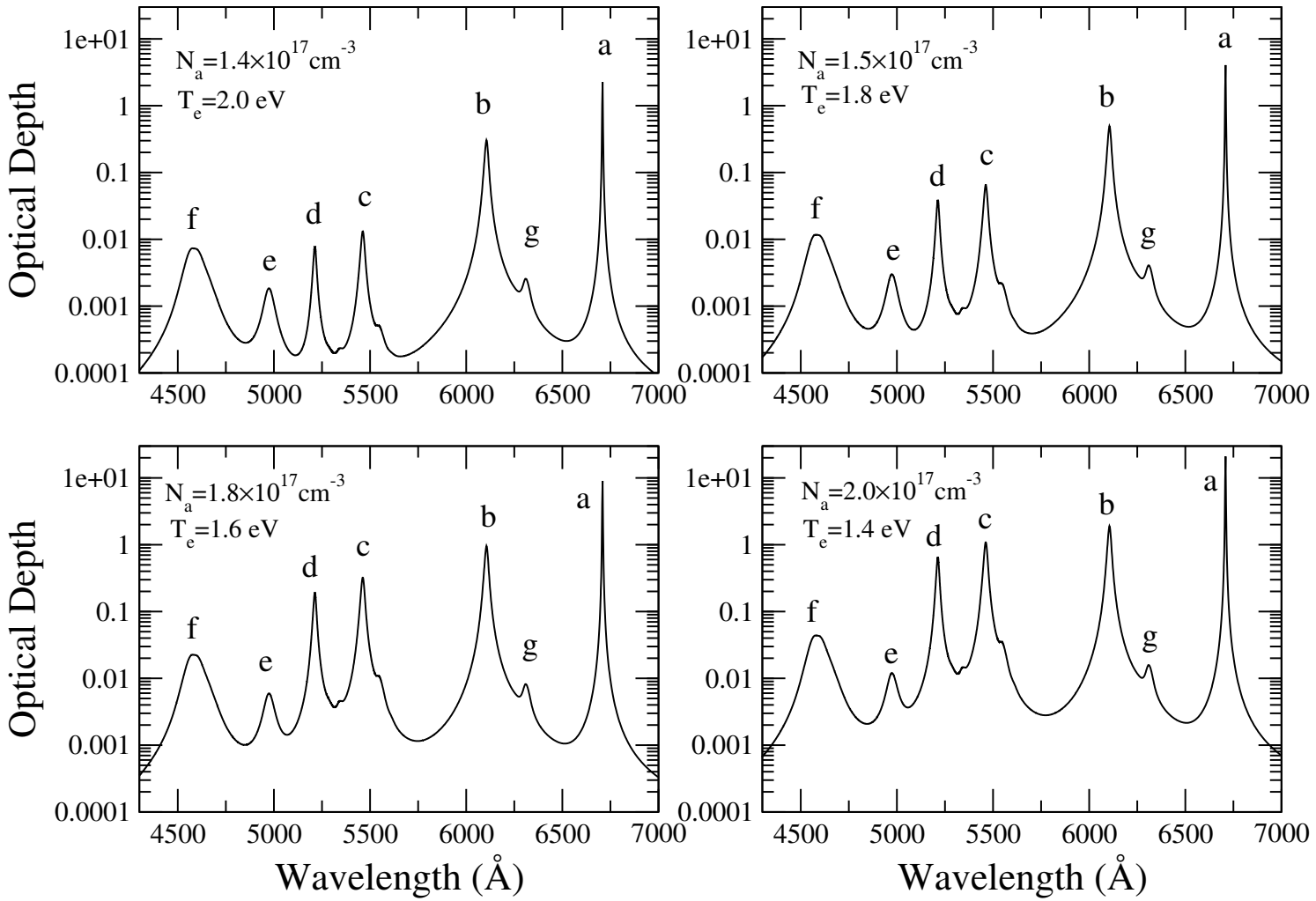

Figure 6.8: The corresponding optical depths for constant N_e series.

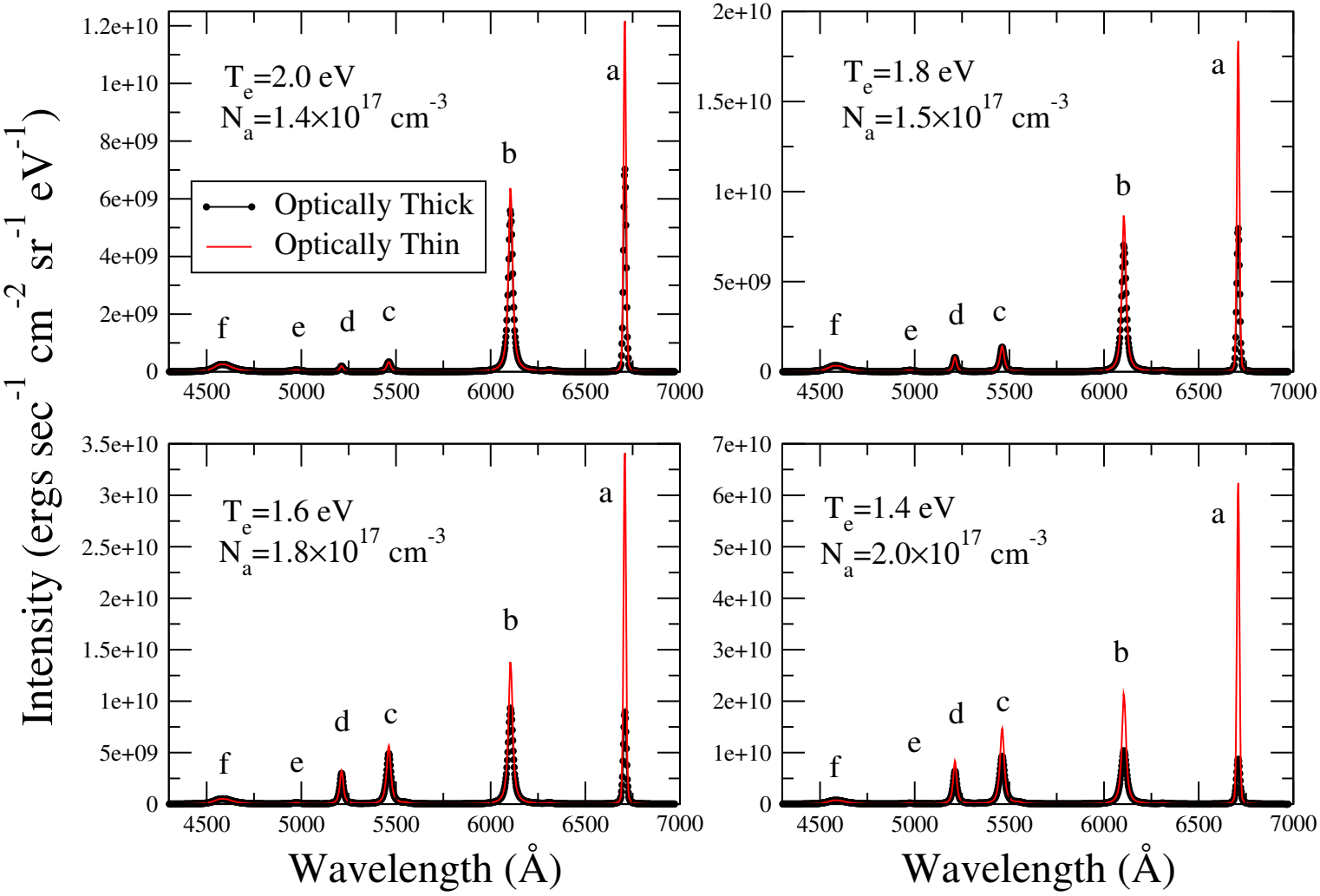

Figure 6.9: Superposition of optically thin and thick spectra for constant N_e series.

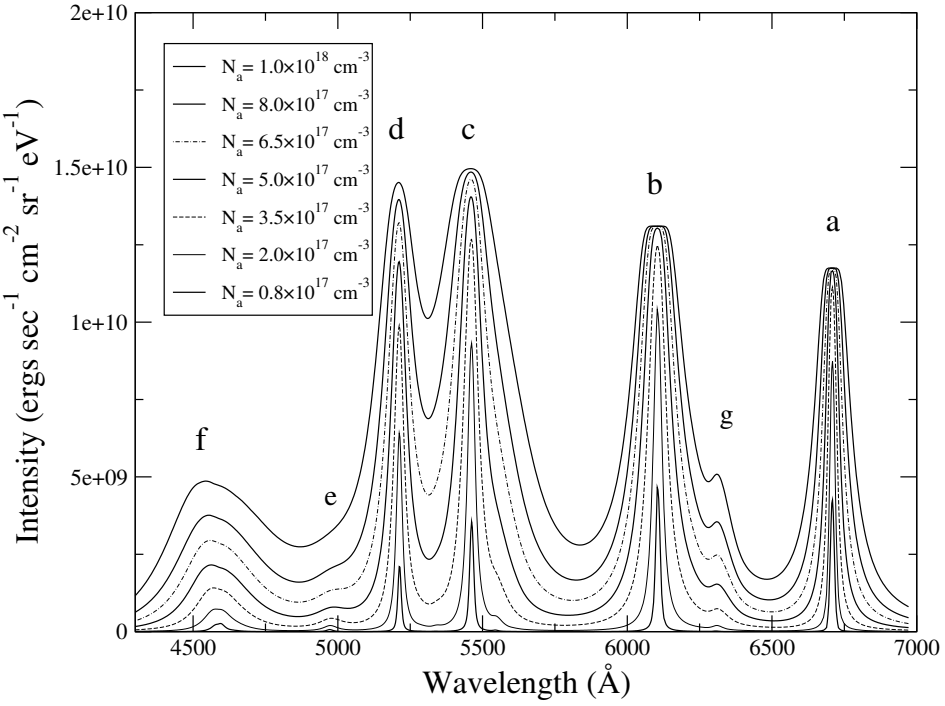

Figure 6.10: Synthetic spectra series produced under constant electron temperature: T_e=1.4 eV. The corresponding electron densities N_e are given in Table 6.1.

6.6.2 Spectral sensitivity under constant electron temperature.

Continuing with the study of spectral sensitivity, the emphasis now is on the effects of density. In Figure 6.10 a series of synthetic spectra was calculated over one decade of atom number density where the electron temperature was fixed at T_e=1.4 eV. See Table 6.1 for the associated values of the electron density. This figure displays the increase in spectral intensity for these neutral atomic lines associated with an increase in density. This effect follows from an increase of efficiency in three-body-recombination in returning population to the neutral species.

Unlike the previous study at constant N_e, the effect of opacity is clear, in particular for the spectra associated with the highest density. Besides the characteristic

Table 6.1: Corresponding electron densites for constant T_e spectral series.

N_a cm^{-3}	N_e cm^{-3}
8.0x10^{16}	8.54x10^{16}
2.0x10^{17}	2.05x10^{17}
3.5x10^{17}	3.51x10^{17}
5.0x10^{17}	4.95x10^{17}
6.5x10^{17}	6.36x10^{17}
8.0x10^{17}	7.76x10^{17}
1.0x10^{18}	9.59x10^{17}

self-absorption of the two lithium **a** and **b** lines, each individual spectral feature shows a characteristic reduction in the growth of the lines to an upper limit approximating the Planck function. The most optically thick lines reach this limit at lower densities.

Figure 6.11 displays the optical depth for the corresponding spectra in figure 6.10. For the strongest features, a one decade increase in the atom number density accompanied a one decade increase in the optical depth. In this figure, the clearest evidence of density dependent profiles, with progressively broader features as a function of density is seen. Interestingly, the increase in atom number density was sufficient to maintain a continual increase in the optical depth, even over the presence of the very sharp line profiles found in the lower densities.

The removal of effects of opacity is shown in Figure 6.12. Like the spectra study under constant density, the comparison with the optically thick plasma is striking. The degree of the atomic kinetic effects hidden by opacity becomes apparent: such as the growth of the lithium 2p-2s (**a**) and, to a lesser extent, of the 3d-2p (**b**) lines due to the migration of population from Li^{+1} to neutral lithium.

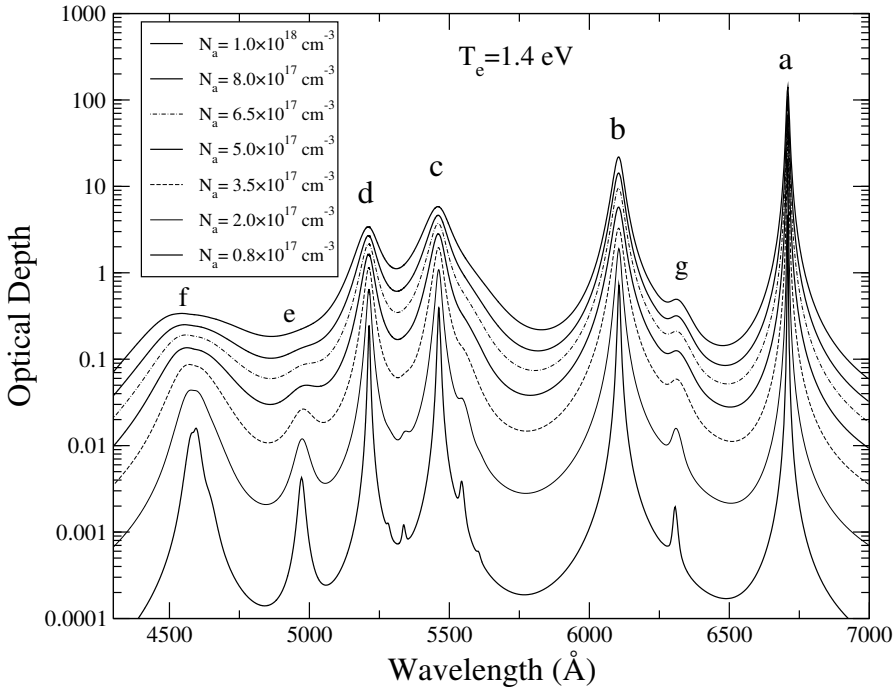

Figure 6.11: Optical depths corresponding to constant electron temperature series: T_e=1.4 eV. The corresponding electron densities are given in Table 6.1.

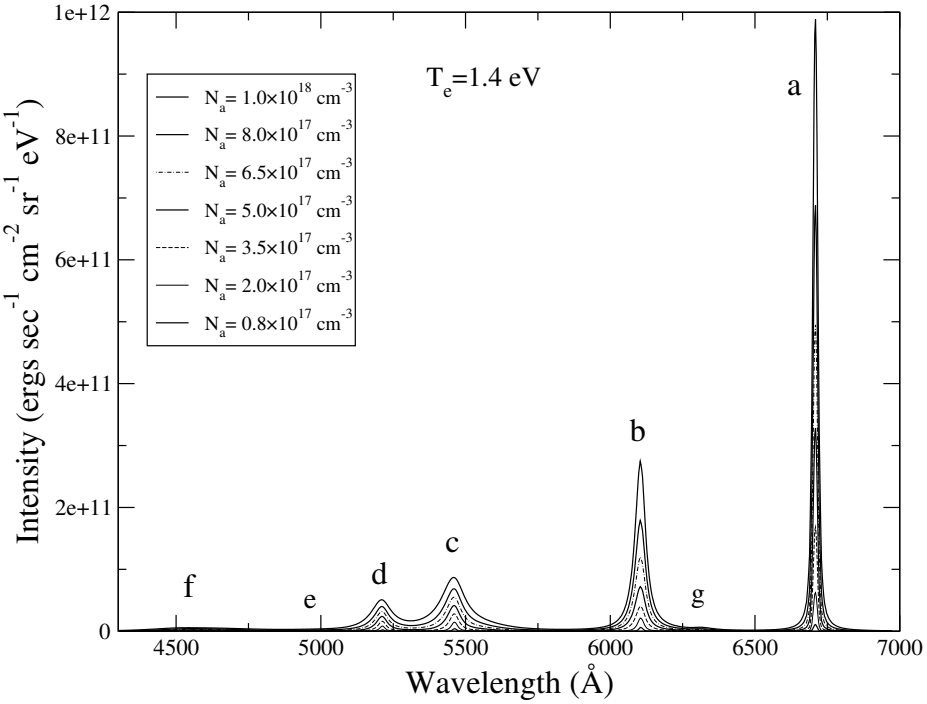

Figure 6.12: Optically thin spectra of constant electron temperature series: T_e=1.4 eV. The corresponding electron densities are given in Table 6.1.

Chapter 7

Theory-Experiment Comparison and Data Analysis

7.1 High Density Spectral Comparison with Experiment

In this section, four experimental lineouts are compared with synthetic spectra. These four lineouts constitute the earliest spectral data with distinct line emission, and in turn, depict the highest density and temperature plasma conditions of the series of experimental lineouts. Specifically, this data corresponds to the ablated plasma at t=20 and 30 nsecs and at distances from the target surface of 28.8 and 86.4 μm. This data was specifically selected for the comparison with our steady state spectral model. Its high density and correspondingly strong collisional rates have been assumed to be in a steady state regime. Issues associated with time-dependent atomic kinetics are discussed in the next section.

7.1.1 Self-reversal and the Justification of Plasma Non-uniformity.

Up until this point the synthetic spectral model has been employed under the uniform slab approximation. This simplest geometry is not burdened by spatial variations in temperature and density and provides a cleaner enviroment for the interpre-

tation and understanding of the synthetic spectral results. Unfortunately, as noted in Chapter 2, the self-reversal feature in the Li I: 3d-2p line supports the existence of a non-uniform plasma. Though a self-reversal feature may exist in a plasma of uniform density and temperature due to a non-uniformity in level populations arising from a position dependent radiation field, the plasma refered to in the four lineouts has been shown to be insensitive to the effects of the radiation field on the populations. The effect of the photon field on the populations can be approximated as an effective reduction of the spontaneous radiative decay rate (SRD). This approximation is the basis for the use of escape factors [28] to include the effects of radiation in atomic kinetic models. A test conducted with the atomic kinetic model for the relevant densities and temperatures predicted for the four early in time lineouts showed no variation in level populations when the SRD rate was eliminated.

7.1.2 Temperature and Density Profiles Generation.

To simulate a non-uniform plasma, a series of temperature and density profiles that define the search space must be generated. The process begins by selecting the only values available to every spatial zone for T_e and N_a, and then assumes that the profiles are symmetric with respect to the center and that the two center zones contain the maximum values. A further restriction on the profiles was impossed: a zone may take on values equal to or less than its neighbor who resides in the direction toward the center of the profile. Or in other words, profiles are either uniform or approximate a concave down function. Following these restrictions, an exhaustive generation of the profiles is performed. The requirement of spatial zones of uniform width was a further restriction placed on the model.

7.1.3 Trial Description

Each synthetic spectrum generated was compared with an experimental lineout to determine the best least-squares fit. Genetic alogrithms (GA) have been proven to be successful in the analysis of X-ray data [43]. An exhaustive search of parameter space was implemented after the use of a GA produced mixed results. Three trials were performed for the set of four experimental lineouts - they included a uniform, four- and six- spatial zone simulations. Due to the extensive increase in parameter space with the inclusion of more zones, an alternative computer program was produced for speed. This new program took advantage of the predefined temperature and density values found in the profiles. An exhaustive database of single zone opacity and emissivity curves was produced by the original parallel program for all permutations of T_e and N_a values. The new program only consisted of the parallel queue (PQ) and the radiation transport solver (RT) (see Chapter 5 for program details) and a small number of additional codes for manipulating the database. The new program produced a 15 times speed up over the original synthetic spectra solver. This modification exemplifies the importance of the coding architecture developed in Chapter 5.

The following are the three trial series for the comparison with t= +20 nsec and t= +30 nsec both at x= 28.8 μm lineouts. Results for the x= 86.4 μm lineouts follow in a similar manner and can be found in Appendix B.

In the comparison shown in Figure 7.1, both the t=20 nsec lineouts proved to be the most difficult to model. The existence of contamination along the wings of the main spectral features, in conjunction with an asymetry on the high energy side of the Li I: 3d-2p line feature, hindered the comparison. Interestingly, the single zone

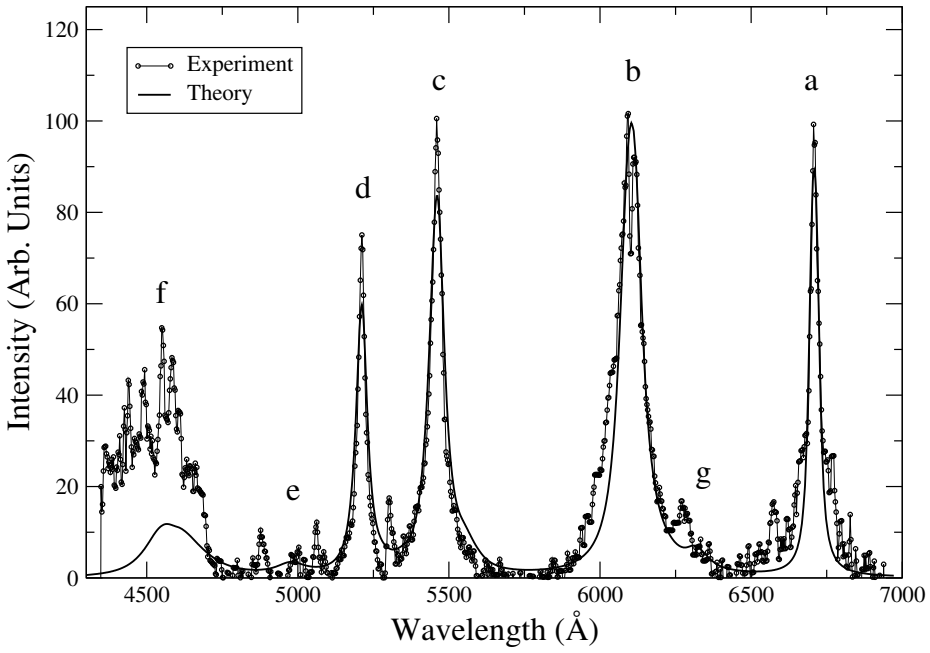

Figure 7.1: Experimental lineout at x=28.8μm and t=2 0 nsec with predicted T_e=1.5 eV and N_a=4.0x10^{17} cm^{-3} uniform synthetic spectra.

calculation obtains the main characteristics of the spectrum. Due to the uniform radiation transport calculation, the Li I:3d-2p self-reversal cannot be approximated nor can the slight asymetry about the self-reversal (see Figure 7.1).

Even with the difficulties mentioned above, the four-zone calculation shows improvement, as shown in Figure 7.2, consistent with an increase in the numerical fitness. The self-reversal and the slight asymetry have now become apparent in the synthetic spectrum with the inclusion of the gradient. Line profiles for the most part compare relatively well for the broadest portions of the spectral lines. Platinum contamination in the silver **c** and lithium **b** lines may partially explain the discrepancy between the spectra.

For the 6-zone calculation, shown in Figure 7.3, the improvement in the numerical fitness unfortunatly does not follow an obvious improvement in the spectral

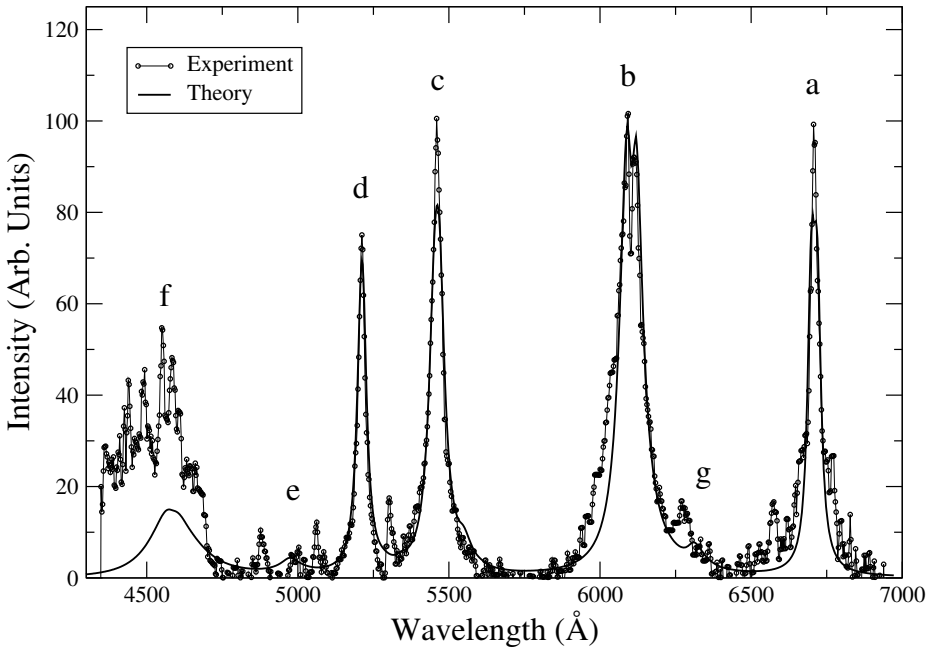

Figure 7.2: Experimental lineout at x=28.8μm and t=20 nsec with predicted T_e=[1.1, 1.9, 1.9, 1.1] eV and N_a=[2.5, 4.5, 4.5 , 2.5] x10^{17} cm^{-3} 4-zone synthetic spectra.

comparison. This lack of real improvement may be due to the limits of the use of a low number of uniform zones in the RT calculation. Unfortunately a large number of zones increases the search time exponentially: The addition of one more zone on either side of the profile increases the calculation time from a few days to a month. Another possible remedy to improve the comparison in the heights would be to employ a non-uniform grid for the inclusion of narrower zones at the perimeter, to contribute low density spectral emission without including their characteristic high opacity. Unfortunately, a scheme has not been devised to confidently search through such a large domain that a variable width spatial grid would entail.

As mentioned above, part of the difficulty in the comparison arises from an asymmetry in the high energy side of the LiI: 3d-2p line (**d**). The existence of this feature has several possible explanations. As mentioned in Chapter 2, oxidation of

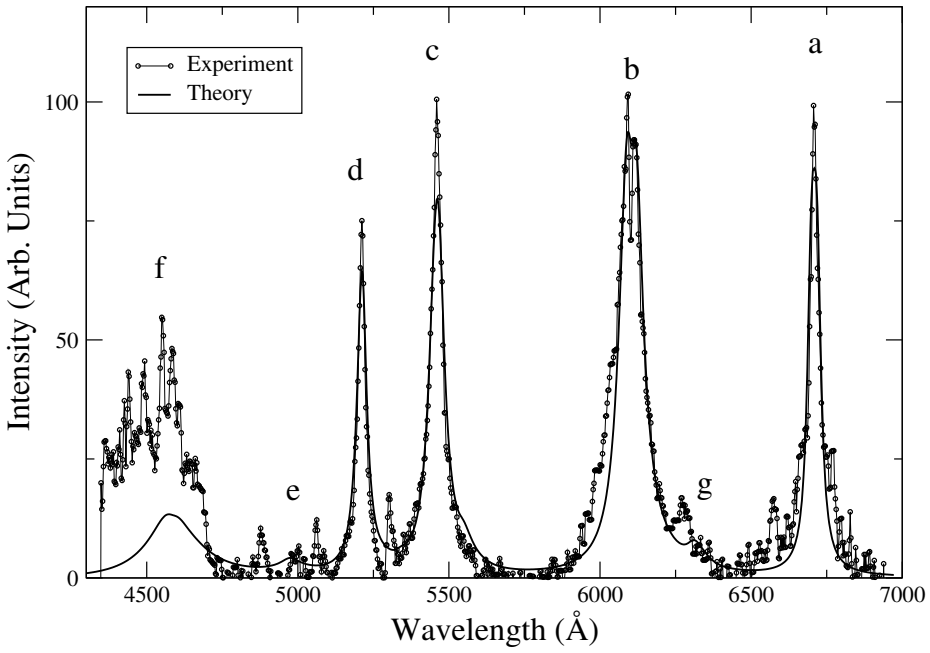

Figure 7.3: Experimental lineout at x=28.8μm and t=20 nsec with predicted T_e=[1.2, 1.2, 2.0, 2.0, 1.2, 1.2] eV and N_a=[2.0, 3.5, 6.0, 6.0, 3.5, 2.0] x10^{17} cm^{-3} 6-zone synthetic spectra.

the target, in particular with lithium atoms after fabrication was concluded to be the origin of Li_2O and LiOH molecules found in the target. The strong $2s^22p^33p$ ^{5}P - $2s^22p^34d$ ^{5}D and $2s^22p^33p$ ^{3}P - $2s^22p^36p$ ^{3}S transitions of neutral oxygen are found in this location, as well as other strong transitions on the high energy side of the Li (**a**) line where contamination is found.

Another possible explanation is the effects of Li^{+0}-Li^{+0}, Li^{+0}-Ag^{+0} and/or Li^{+0}-molecule interactions for the broadening of the spectral line. Estimates based on reference [44], for resonance (line broadening between levels of the same species connected by dipole a transition) and Van der Waals (more general atom-atom interaction) broadening were found to be small in comparison to Stark broadening. It should be kept in mind that limitations to these approxmations exist and in particular for Li^{+0}-Ag^{+0} broadening these estimates may not be appropriate.

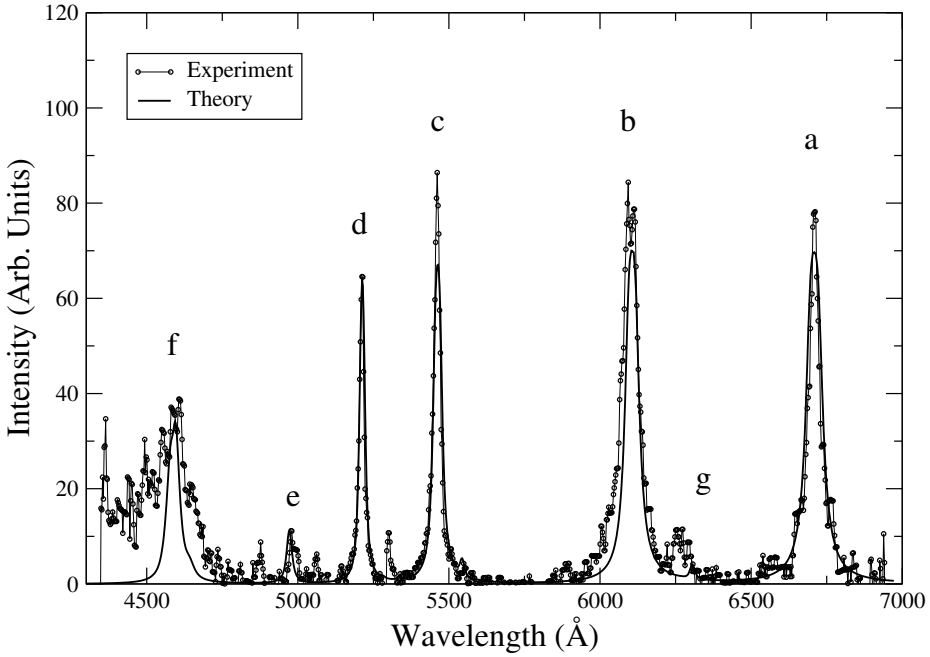

Figure 7.4: Experimental lineout at x=28.8μm and t=30 nsec with predicted T_e=0.8 eV and N_a=1.0x10^{17} cm^{-3} uniform synthetic spectra.

Due to the possibility of contamination and the plasma's high opacity, developing and performing more sophisticated profile calculations with the hopes of explaining the asymmetry would be impractical.

The comparison with the synthetic spectra for the t=+30 nsec, x=28.8 μm appears much better than the t=+20 nsec data. This is also substantiated by an order of magnitude increase in fitness. The asymmetry no longer dominates the high energy side of the 3d-2p line, and the existence of contaminating features appears to be weaker about the wings of the main features. The uniform calculation, Figure 7.4, captures most of the main features; however, the LiI:3d-2p line width is underestimated. As a confirmation of the quality of the comparison, the LiI: 4s-2p and 4d-2p lines found in the **f** complex of lines compares well with the experimental data though

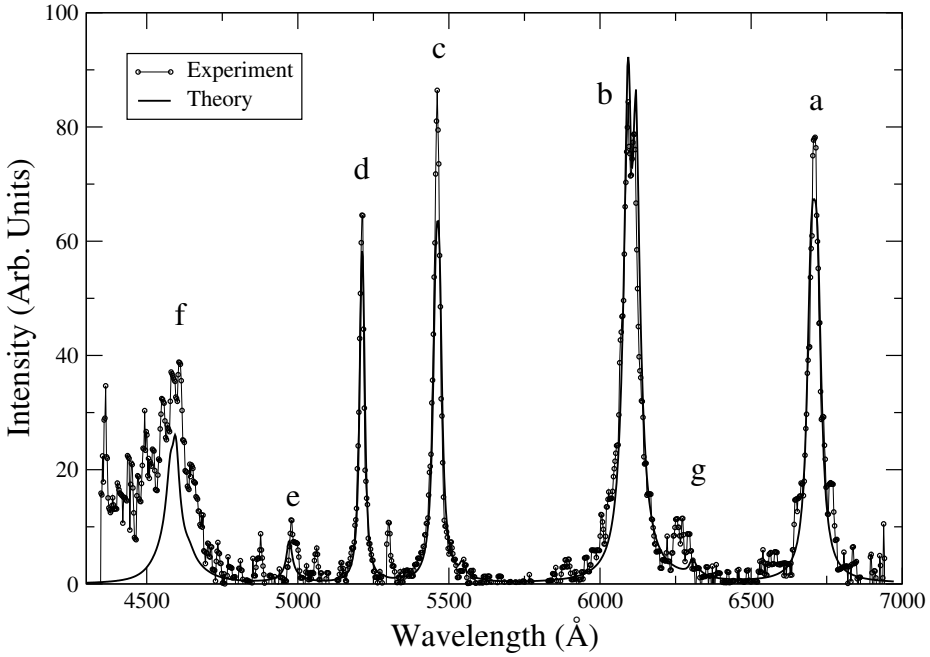

Figure 7.5: Experimental lineout at x=28.8μm and t=30 nsec with predicted T_e=[0.7, 1.8, 1.8, 0.7] eV and N_a=[1.0, 2.0, 2.0, 1.0] x10^{17} cm^{-3} 4-zone synthetic spectra.

they have not been included in the least-squares minimization procedure.

In the 4-zone calculation, Figure 7.5, the self-reversal on line **b** is clearly displayed, and also a much better agreement in the width of the Li I: 3d-2p line is observed. For the 6-zone case, Figure 7.6, the comparison is quite favorable. Again platinum lines in **c** and **a** contribute to the disparity.

Figure 7.7 describes the optical depth of 6-zone synthetic spectra. Notice that the optical depth is greater for the t=+30 nsec series. This is due to the existence of very sharp line profiles in the LiI: 2s-2p and 3d-2p lines that are associated with the low electron density. Also, the lower temperatures found in the t=+30 nsec spectra that place more population in the lower levels of the line transitions. Notice in this figure that the silver lines approach optical depths as high as τ=10, while the Li I:2s-2p has τ=400. Interestingly, the uniform and 4-zone optical depths are similar

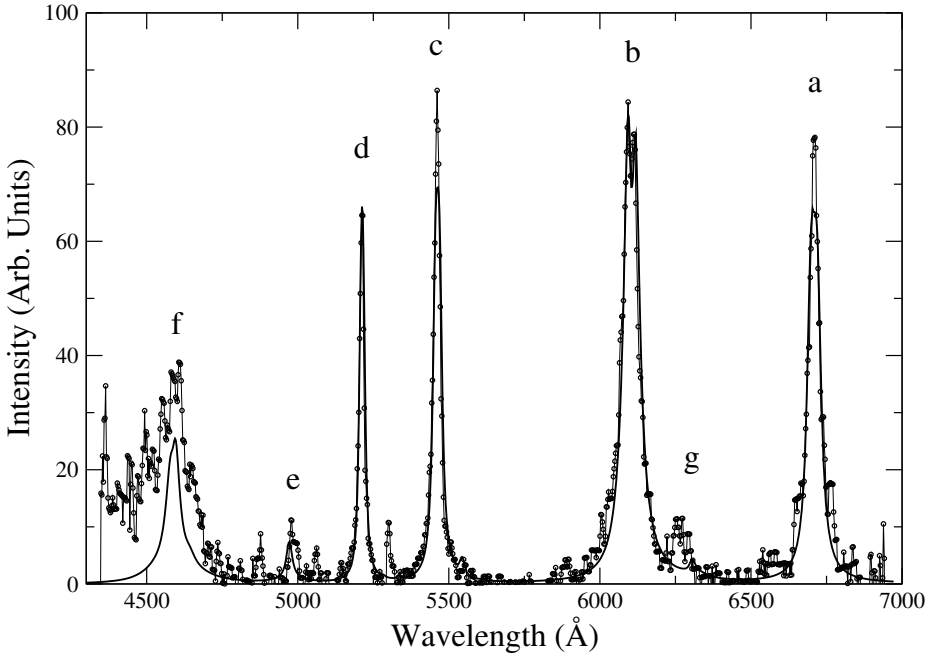

Figure 7.6: Experimental lineout at x=28.8μm and t=30 nsec with predicted T_e=[0.7, 0.8, 2.3, 2.3, 0.8, 0.7] eV and N_a=[1.0, 1.0, 2.5, 2.5, 1.0, 1.0] x10^{17} cm^{-3} 6-zone synthetic spectra.

to the 6-zone case; see Appendix B.

Figure 7.8 and 7.9 describe the 1, 4 and 6 zone resulting profiles for the t=+20 and +30 nsec calculations respectively. The t= +30 nsec results, show distinct differences in boundary and core values, where the single zone solution consistently approximates the boundary values for both T_e and N_a. These two boundary zones predominantly contribute the non-uniform opacity needed to reduce Li I **a** and **b** lines with respect to the Ag I **c** and **d** lines, while the higher density core provides the higher electron density needed to match the widths of the spectral lines. For the t=+20 nsec results, the single zone solution appears to approximate the average of the entire profile. This implies that all zones are strongly participating in the opacity and in the line broadening, thus spectral line widths are not primarily defined by any particular

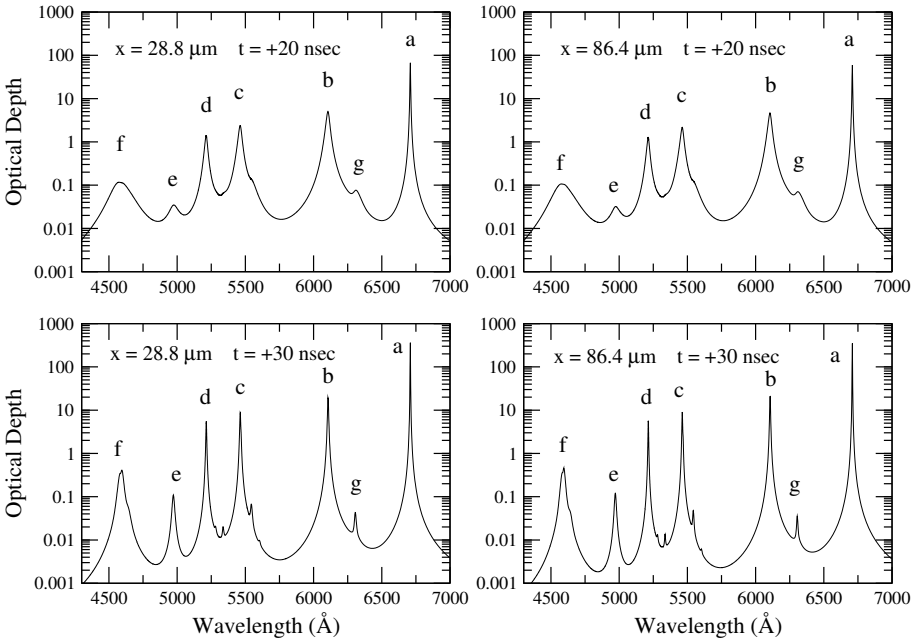

Figure 7.7: Optical depths for all four 6-zone synthetic spectra.

region of the plasma, unlike the previous results.

To obtain an understanding of the sensitivity of the synthetic spectra to the temperature and density profiles, Figure 7.10 contains the best, next best, 40th and 98th best solutions for the t= +20 and +30 nsec, x = 28.8 μm synthetic spectral results. For the t= +20 nsec solution, the boundaries of the plasma show very little variation, unlike the core spatial zones. As mentioned before, the boundary zones are predominantly defining the opacity need for the spectra, while the core adds the widths of the lines. For the t= +30 nsec spectra, though, the core temperature shows a simliar variation, however, the density shows none. In this plasma, the average ionization stage varies, from 1 to 1.5 through the total range of temperatures. Therefore, the only means to significantly raise the electron number density, and thereby the line profiles, is through a increase in atom number density. Due to the broad lines found in the t= +20 nsec lineouts, the core elements must maintain

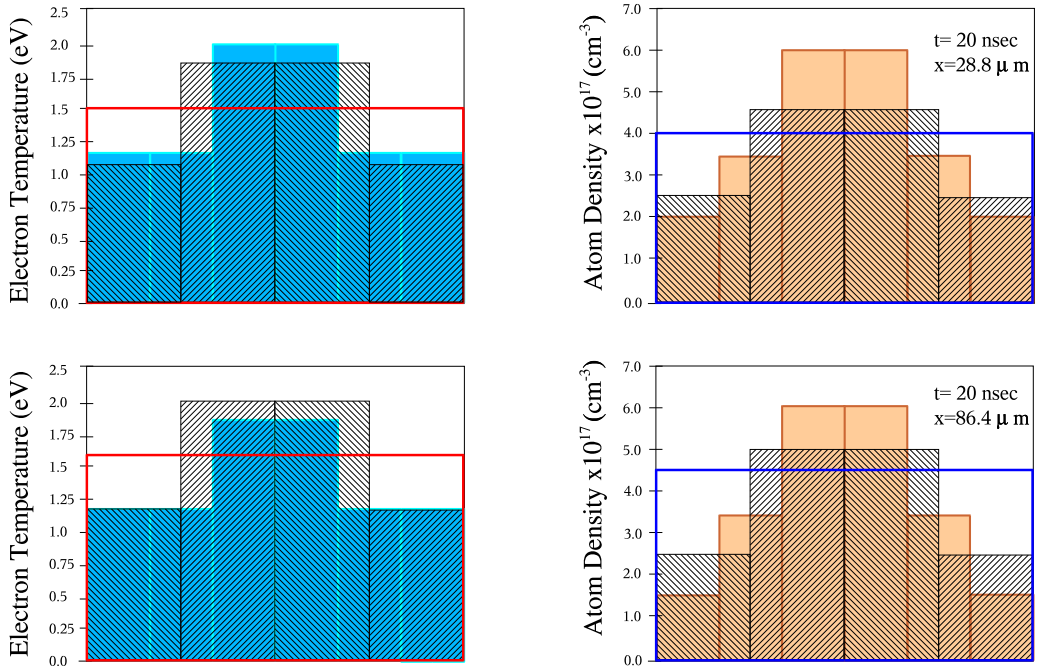

Figure 7.8: Uniform, 4 and 6 zone T_e and N_a profiles results for t= +20 nsec synthetic spectra.

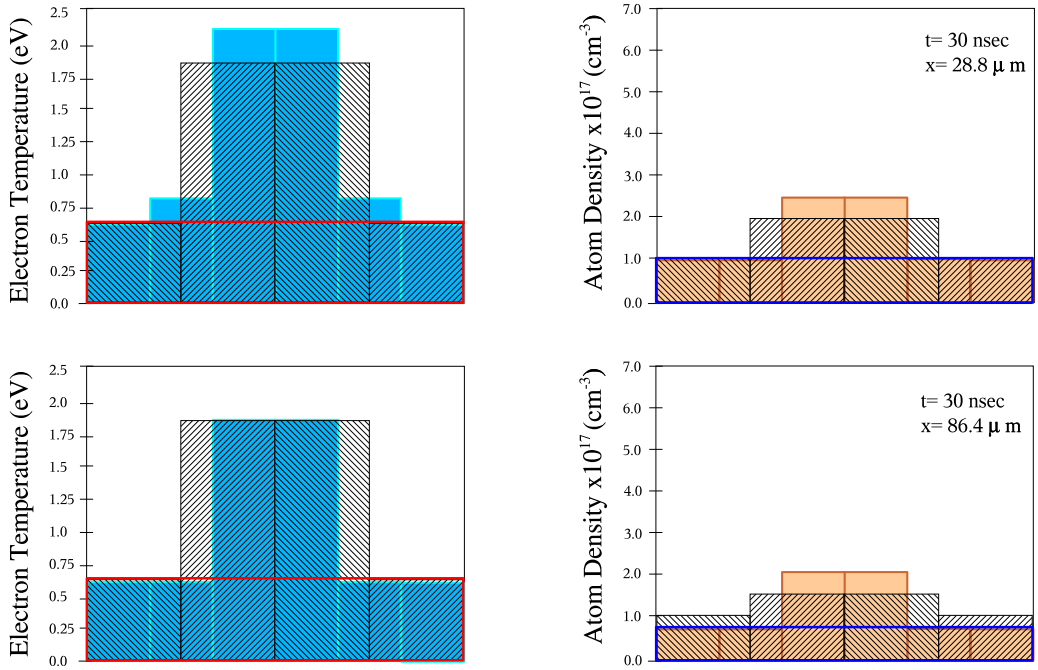

Figure 7.9: Uniform, 4 and 6 zone T_e and N_a profiles results for t= +30 nsec synthetic spectra.

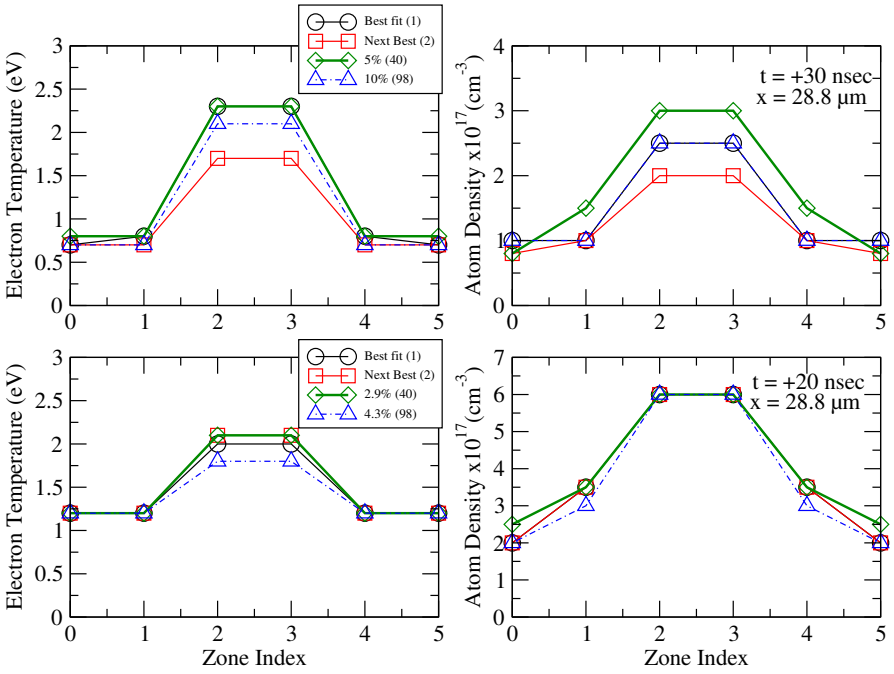

Figure 7.10: 6-zone temperature and density intermediate results associated with the 1st, 2nd, 40th and 98th best results for t= +20, +30 nsec at x = 28.8 μm synthetic spectra.

a high atom number density to obtain the proper line profiles. It should also be pointed out that the fitness varies slowly with the change in T_e and N_a profiles. This is undoubtibly an artifact of the high opacity lessening the sensitivity of the spectra. The variation in regards to the spectra, is seen in Figure 7.11.

7.1.4 Lithium Lines Behaviour Under High Opacity.

We conclude this section by describing the difference in behaviour of the Li I:3d-2p and 2p-2s lines. One critical question arises about the behaviour of these lines: If the Li I: 2s-2p line has the largest optical depth, then why is a large self-reversal not present in the line, such as is found in the Li I: 3d-2p line? The answer lies in the emissivity and opacity functions. From Figure 7.12 and Figure 7.13 we see that the Li I: 3d-2p **b** line is composed of contributions from different spatial regions of the

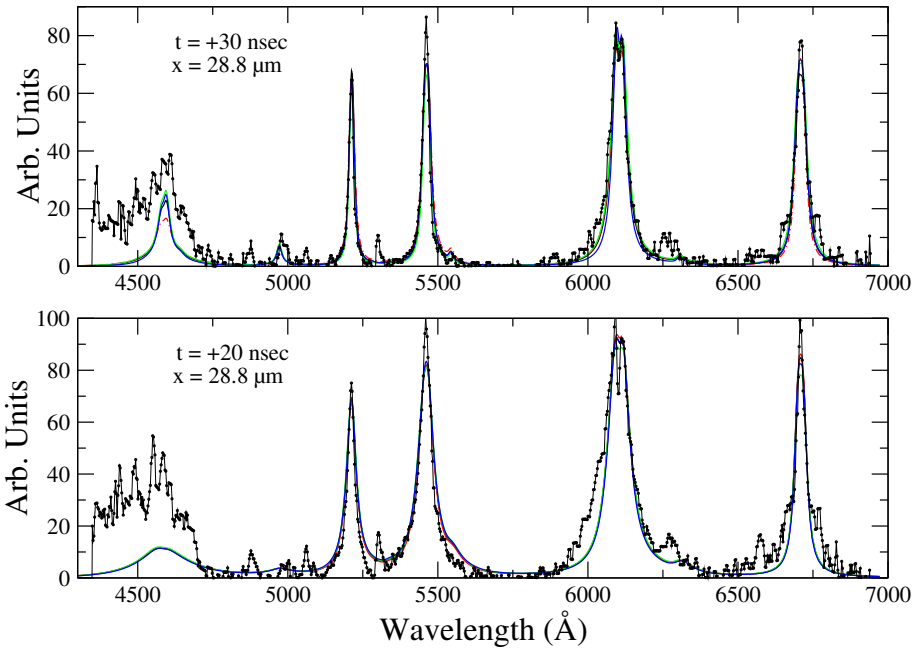

Figure 7.11: 6-zone spectral 1st, 2nd, 40th and 98th best results for t= +20, +30 nsec at x = 28.8 μm synthetic spectra with corresponding experimental lineouts. The individual curves are indistinguishable.

plasma: the wings of the line originate from the high density center region of the plasma, while the core of the line originates from the low density spatial region of the plume. This configuration is optimal for a self-reversal in particular for a plamsa large spatial extent. Or in other words, we may consider the core of the line approaching the Plankian function at a different temperature than that of the wings. On the other hand, the Li I: 2s-2p line is not dominated by contributions from different plasma regions: its line profile is dominated by emission and absorption from the boundaries of the plasma. Therefore, this line behaves as if it were produced from a uniform plasma simply undergoing self-absorption without significant self-reversal.

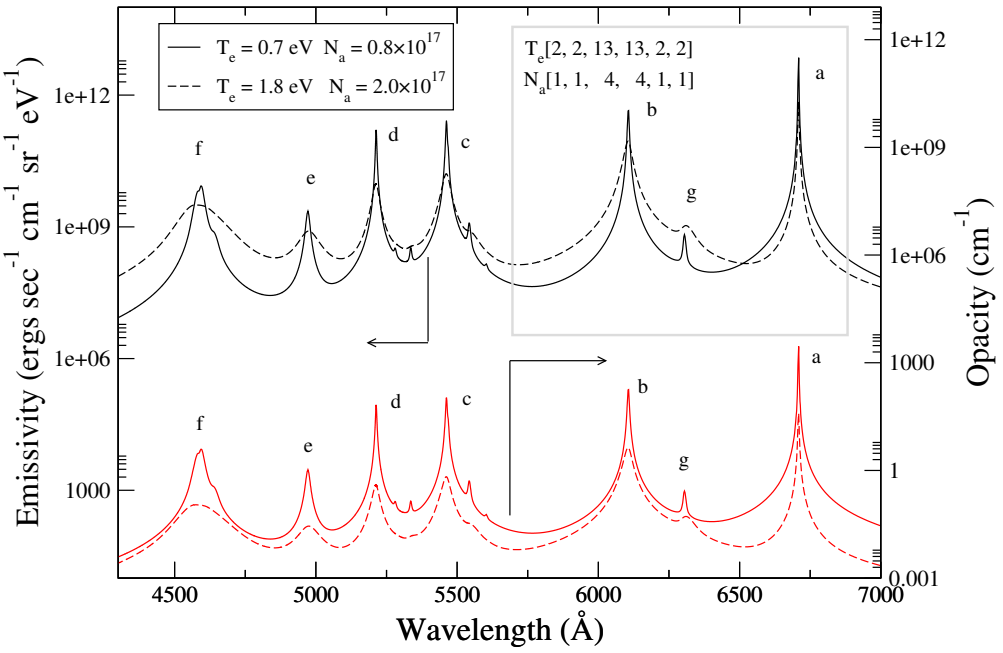

Figure 7.12: 6-zone emissivity (upper curves) and opacity (lower curves) from t= +30 nsec x= 86.4 μm synthetic spectra results from plasma core and boundary zones.

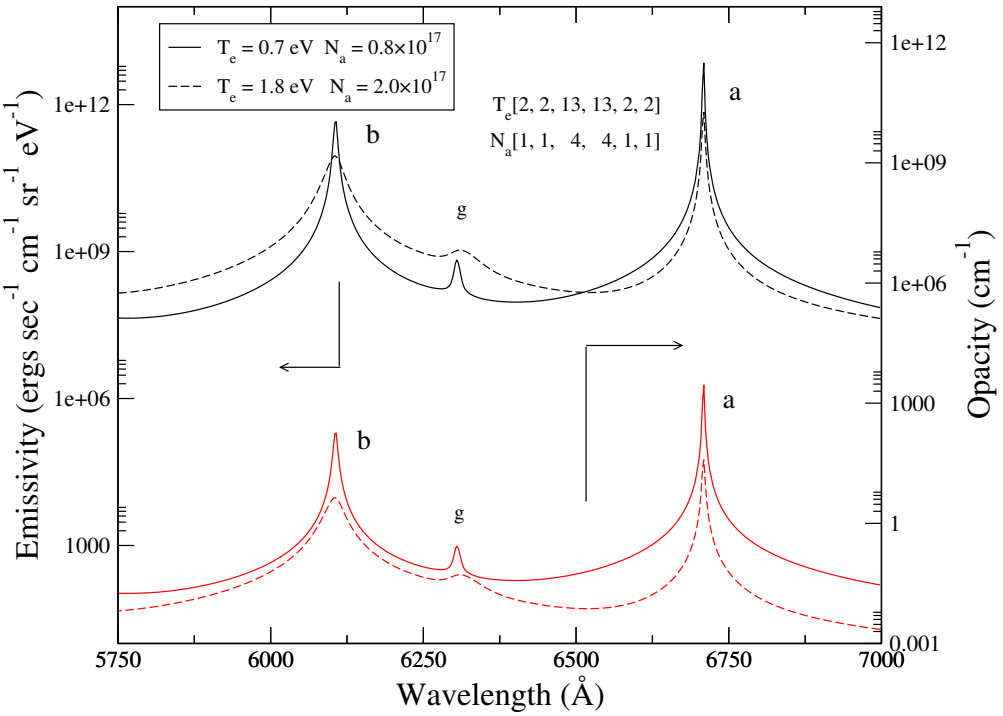

Figure 7.13: 6-zone emissivity and opacity from t= +30 nsec x= 86.4 μm synthetic spectra results from plasma core and boundary zones.

7.2 Modeling the Low Density Expansion and Time-Dependent Effects.

Before the data from the Sandia experiment became available, extensive work was performed to accurately model the 1-D hydrodynamic expansion of ablation plumes with the hydrodynamic code HYAT [45]. Due to the small amount of laser energy dispensed to the target, a careful accounting of the laser energy coupling to the target had to be performed. This involved the inclusion of a realistic equation-of-state (EoS)[46], and the tracking of phase transitions. Early work focused on carbon, where it was found that an expanding fluid element during ablation, could undergo a transition across all thermal phase boundaries, and not simply sublimation as was customarily assumed in gas dyanmic simulations. Furthermore, these hydrodynamic simulations went beyond the typical gas dynamic models used in modeling these systems [47]. This work supported the need for the inclusion of realistic EoS for modeling laser ablation hydrodynamics.

A custom LiAg equation-of-state was generously provided by J.D. Johnson of T-1 from Los Alamos National Laboratory to model the Sandia experiment. Though the expectation was that the LiAg 43-57% binary alloy EoS was of good quality due to the existence of a single solid phase from tabulated experimental data, an accurate EoS for the thin layer of lithium-oxide that it is expected to form on the target surface when the target was brought up to atmosphere was not found. An effort to measure the reflected laser radiation from the target led to results varing between 20-50% at the laser angle of incidence used in the experiment. This made difficult to perform hydrodynamic simulations of the Sandia experiment. Yet, these simulations did permit to extract qualitative features of this low fluence laser ablation, such as

the density and temperature time histories and the rate of fluid expansion. This qualitative description became important in describing the rarified expansion of the plasma.

From numerous runs of the hydrodynamic code, the density time history was characterized for a fluid element just leaving the surface at +20 ns after the laser pulse by an initial exponential followed by a slower linear decrease. This corresponded to the continuing rapid expansion from $5x10^{17}$ to $1x10^{15}$ cm^{-3}, followed by an almost non-expanding fluid element with a nearly constant transverse velocity. Temperature time histories for fluid elements just leaving the surface were found to fall linearly from 1 eV to 0.4 eV in time. Hydro-simulations predicted the transverse motion of the fluid elements between 10 - 15 μm/nsec depending on the degree of reflectivity. This corresonded well to measurements taken from the motion of bulk emission as seen in the Sandia CCD images ($\tilde{1}7$ μm/nsec). Though no guarantee exists that the brightest emmissions of the two consecutive temperal images corresponded to the same fluid element, the value is consistent with velocity measurements found in the literature ([48]) for this regime of laser irradiation.

In particular, the time scale change of the two decade drop in atom number density due to the initial hydrodynamic expansion corresponds to the nanosecond time scale of the collisional processes at these low densities. This condition requires time-dependent atomic kinetics instead of steady state atomic kinetics that were employed to model level populations of the high density plasma early in time and close to the surface. Therefore, a time-dependent version of the atomic kinetics model was created (see Chapter 4). It was driven by density and temperature time-histories that were patterned after the time evolution of fluid elements observed in 1D hydrodynamic simulations of the experiment.

Figure 7.14 shows the time evolution of neutral Li total fractional population (i.e. ground plus excited states) over a time interval of 80 nsec (t = +20 – 100 nsec). This figure also displays the results of the steady-state calculation driven by the same set of instantaneous temperature and density points. The results in Figure 7.14 clearly show that time-dependent effects on the atomic kinetics are indeed important, and that the time-dependent fractional population always lags behind the steady-state calculation. Initially, the sudden drop in density effectively drives ionization due to the weakening of three-body (collisional) recombination rates. Subsequently, the temperature drop dominates, and the system recombines. In the time-dependent calculation this recombination proceeds at a much slower rate as compared to the steady-state case that instantaneously adjusts to the local temperature and density conditions. The cascade of population fed into high n levels by 3-body recombination and driven downward toward the ground state by collisional de-excitation runs into a "bottle-neck" at the $1s^2 3d$ level which cannot depopulate fast enough as it would in the steady-state case. As a result, the **b** line intensity ($1s^2 3d$ - $1s^2 2p$) tends to overtake that of the **a** line ($1s^2 2p$ - $1s^2 2s$) which is not seen in the steady state case (see Figure 7.15). This "bottle-neck" results in a decreased efficiency of collisional de-excitation to remove population from the $1s^2 3d$ level due to the larger energy difference between $1s^2 3d$ and the $1s^2 2p$ levels compared to energy differences between high-n levels. After an extensive parameter study with temperatures and densities relevant to this region of the plasma plume, we found that a steady-state system would not produce a condition where line **b** was greater than **a** .

Indeed, this time-dependent effect is observed in the data (see Figures 7.16, 7.17). First, all the lines show narrow and very similar line profiles. This is indicative of the low density plasma in which plasma broading effects are no longer important

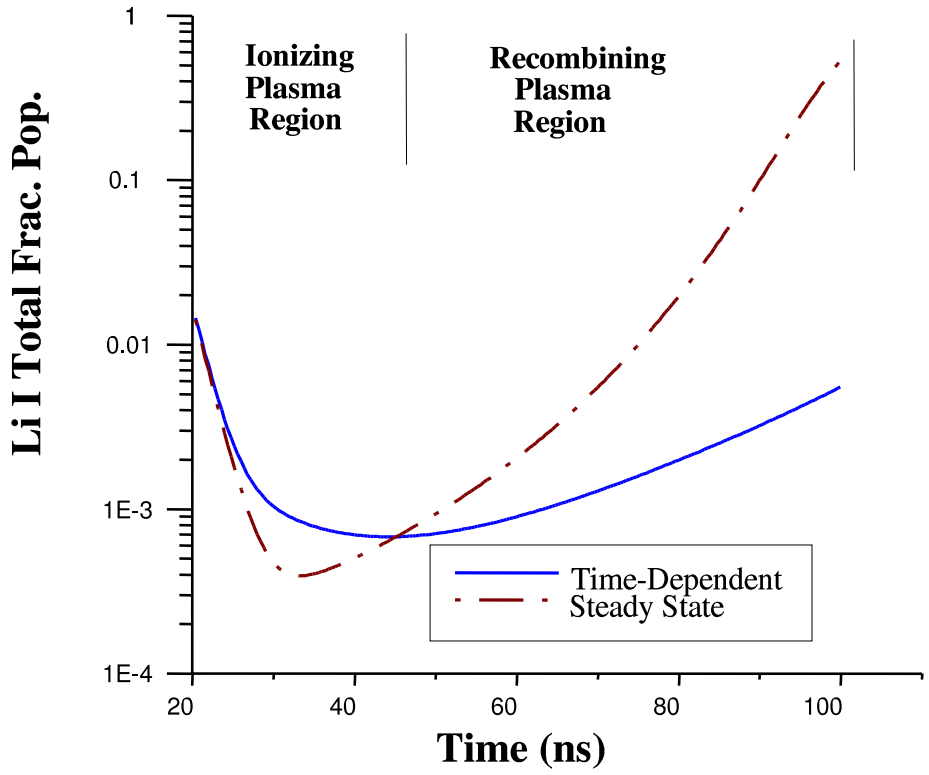

Figure 7.14: A comparison of the evolution of time-dependent and steady-state atomic kinetic models for the same time history. The total fractional population of Li atoms lags in the time-dependent as compared to the steady-state results.

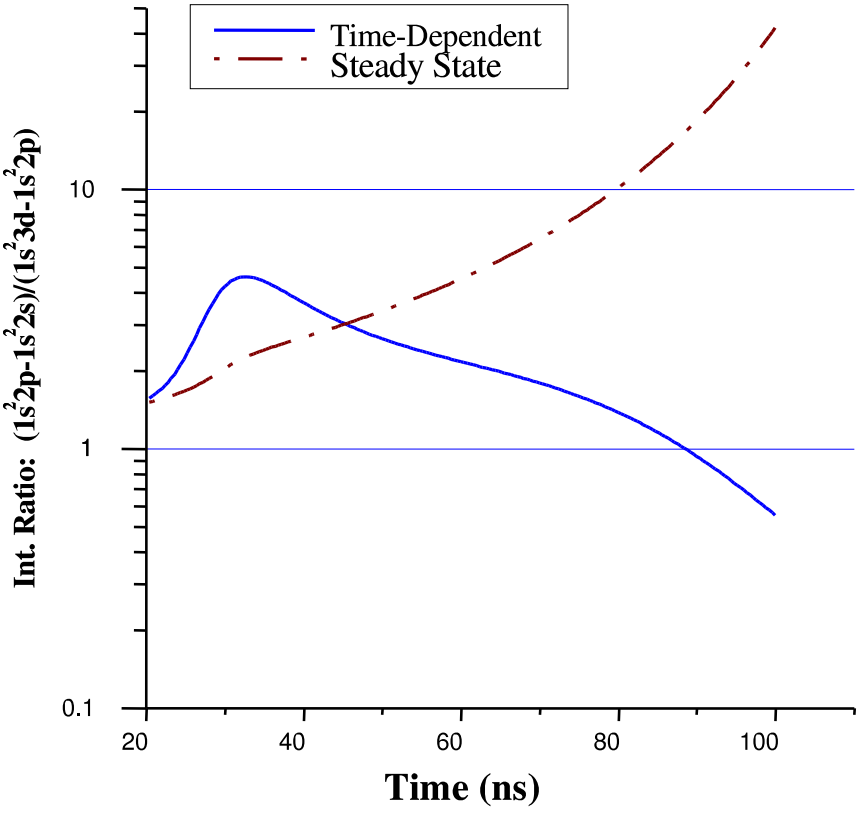

Figure 7.15: A comparison between time-dependent and steady-state evolution of the ratio of the lithium $1s^2 2p - 1s^2 2sto 1s^2 3d - 1s^2 2p$ line intensities. Cascading population from high n levels driven downward toward the ground state by collisional de-excitation runs into a "bottle-neck" at the $1s^2 3d$ level which cannot depopulate in the time-dependent case as fast as in the steady-state case.

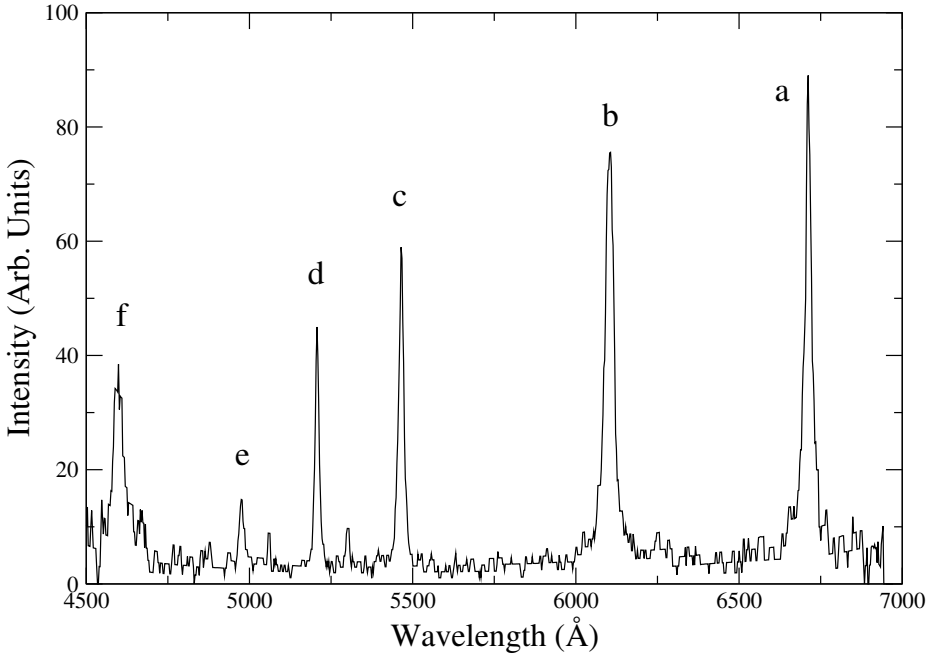

Figure 7.16: Experimental lineout at x=170.0 μm from the target surface, and t=+50 nsec after the end of the laser pulse.

and line shapes are essentially determined by the instrumental function. Second, the Li **b** line clearly overtakes the Li **a** line as times progresses. We note that these experimental lineouts were extracted at 50 and 75 nsec after the end of the laser pulse and at distances 170 and 450 μm from the target's surface, respectively. An expansion velocity of 10 - 20 μm/nsec was obtained from the experimental CCD images. Thus, the experimental spectra shown in figures 7.16,7.17 can be taken as produced by the same fluid element as it moves away from the target surface.

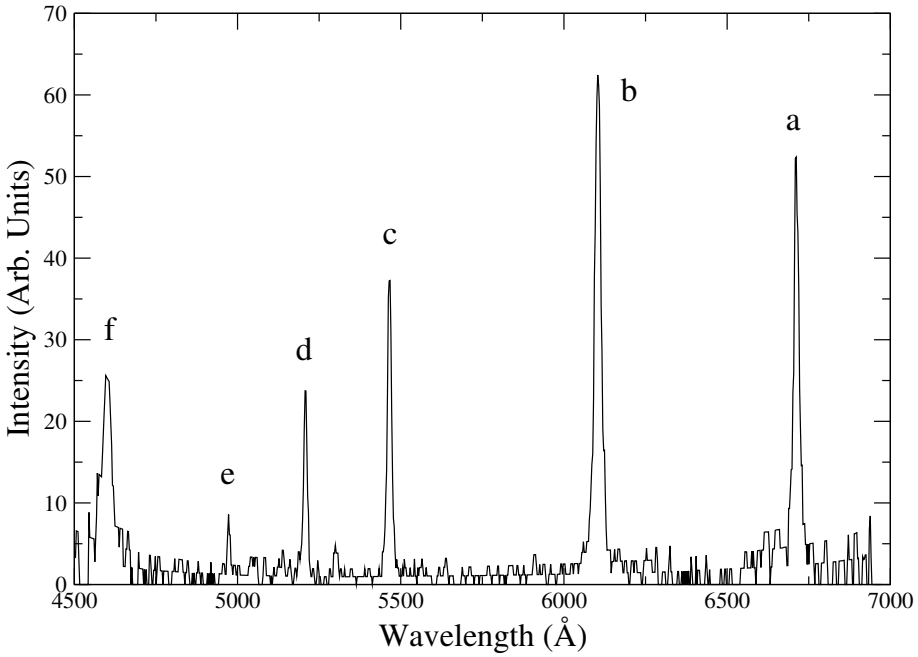

Figure 7.17: Experimental lineout at x=450.0 μm from the target surface, and t=+75 nsec after the end of the laser pulse.

Chapter 8

Conclusions

This work has addrssed the spectroscopic analysis of low fluence laser driven ablation plasmas of the kind found in typical laser-abaltion applications to material synthesis and thin film manufacturing. Efforts concentrated on developing techniques to quantitatively model this complex environment. In particular, modeling results were applied to the analysis of experimental spectral data. This point cannot be overemphasized, since time and spatially resolved, high quality line spectra in this low-fluence laser driven regime is extremely rare. From a developmental point of view, atomic structure codes commonly used in modeling highly charged ions in hot plasmas do not produce data of sufficient quality for the spectroscopic analysis for low temperature plasma plumes. To overcome this problem, a semi-empirical method to compute the necessary atomic structure data was implemented in a Hartree-Fock code.

From an analysis point of view, significant insight was obtained in both the early in time, high density regime where spectra is dominated by steady-state atomic kinetics and opacity effects and the later in time, rarefied plume characterized by time-dependent atomic kinetics. This fact, in particular, was not recognized by the laser ablation community as modeling in this regime was solely performed using Saha-Boltzmann equilibrium assumptions.

During the development of this model, difficulties were encountered that commonly arise in calculating the atomic structure for neutral transition-elements. To overcome this problem, corrections to the energy level structure through the use of the RCE semi-empirical procedure were employed, and included into the Los Alamos TAPS suite of atomic structure and collision codes. This approximation has increased the accuracy of wave functions and in turn collisional data. A further benefit of this work has been the use of improved wavefunctions for calculating detailed Stark-broadened line profiles of optical transitions in atoms. With the future plan of a web based access to this suite of codes, the possibility for more accurate data for neutral transition-elements will become realized.

To model the 43%Li and 57%Ag plasma plume produced at SNL, a fully self-consistent multi-element multi-spatial zone collisional-radiative atomic kinetic model had to be produced to account for the detailed interactions between the various species in the plasma. This model permits the calculation of composite line spectra where both Ag and Li line emission are self-consistently computed. Thus, Ag and Li line spectra can be used simultaneously for analysis. Both a time-dependent and a steady-state version were employed to analyze the Sandia experiment. This model has further applications in the calculation of the average ionization stage for stochiometrically complex materials, for the determination of various plasma parameters.

Along the way, while working on a parallel code for the multi-element atomic kinetic model, a programming methodology was developed to deal specifically with the demands of large scale software development in scientific research projects. This methodology deals with the primary problem of research codes: constant evolution. The typical monolithic code design employed in simulation codes is ironically quite inflexible to change. The developed methodology includes a set of user libraries to

link modular elements through well defined interfaces. These interfaces allow for an easy exchange of components, and the message passing utilities employed to connect the modules, found in the user libraries, allow for the easy parallel execution of the modules across a set of networked computers.

To compare with experimental data, synthetic spectra were computed. This required the production of detailed lines shapes that included Stark, Doppler, and natural broadening. These lineshapes provide information on the plasma environment of the radiators. Due to the lack of non-neutral lines within the experimental spectral range, these profiles provided us with valuable information on the degree of ionization of the plasma. To include the bulk plasma effects on the spectra, a radiation transport model was developed, and to deal with the large opacities found in the system, a semi-analytical radiation transport model was employed and tested. With the spectral model, a series of studies for a theoretical uniform plasma were undertaken to understand the specific contributions of atomic kinetics, lineshapes, and opacity to the spectra. This study revealed the high degree of opacity effecting the Li I 2s-2p and 3d-2p lines and the gradual loss in sensitivity of the Ag I 5d-5p lines.

For the early in time and high density case, detailed comparisons between experimental data and synthetic results were performed. 1-, 4- and 6- spatial zone profiles were used to simulate gradients in temperature and density in the plasma. Predicted profiles, along with the a description of the uniqueness of the results, were discussed. From these results, the spectral contributions from plasma boundary and core spatial zones revealed the importance of the lower density zones' contribution to the opacity, while the higher density core zones provided the environment for the broadening of lines. This analysis also revealed the unexpected behavior of the Li I: 2s-2p line in

regards to the Li I: 3d-2p line. The Li I: 3d-2p line was found to be a composite of low density contributions in the core of the line, and high density contributions in the wings of the line. This composite quality is not found in the Li I: 2s-2p line feature and therefore it behaves differently.

Finally, for the later in time, low density case, hydro-simulation results were used to approximate density and temperature time histories for the Li-Ag expanding plume. Time-dependent and steady state models computed with the same density and temperature time histories revealed diverging solutions. The evolution of a fluid element in this regime is characterized by two distinct phases. An ionization phase driven by the rapid decompression of the plasma near the surface, and a recombination phase that is characterized by a nearly constant density far away from the surface. During the evolution of the plasma, the time-dependent result always lags behind the steady state solution. Time-dependent effects are seen in the synthetic spectra, where cascading population from high-n states run in to a "bottle-neck" at the $1s^2 2s^2 2p$ energy level in Li I. This retardation of the cascading populations alter the line intensity distribution in the spectra. Such effects are also observed in the experimental spectra.

Appendix A

Neutral Li and Ag Atomic Structure

The following appendix contains the Grotrian diagrams based on experimental data for neutral lithium [49] and neutral silver [15], [16].

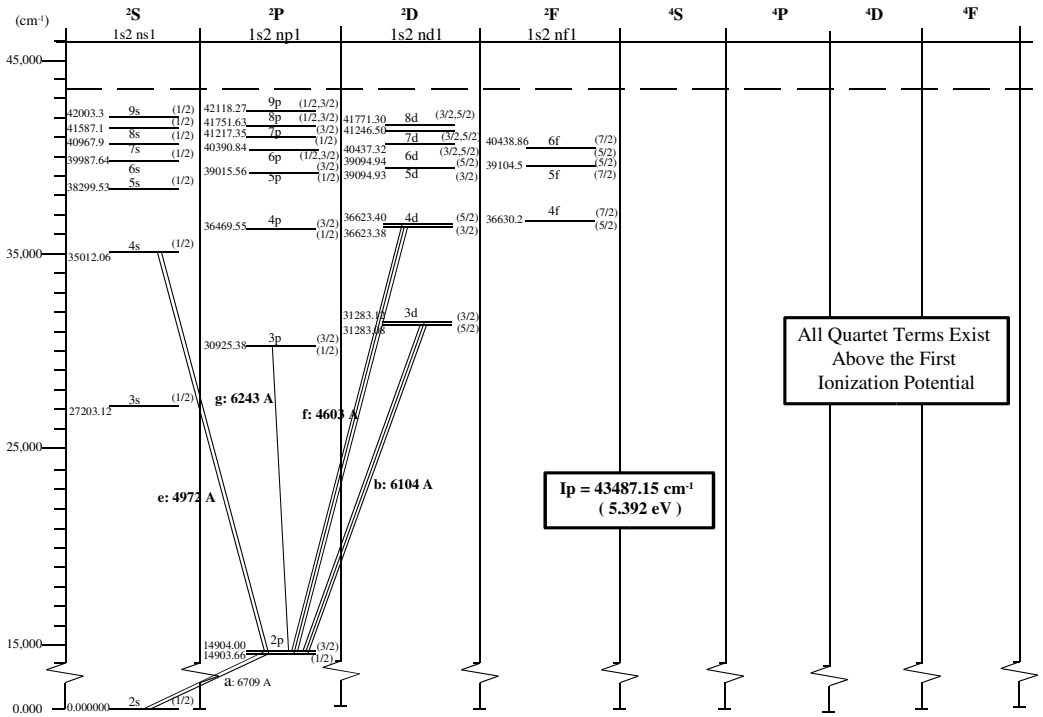

Figure A.1: Li I Grotrian diagram.

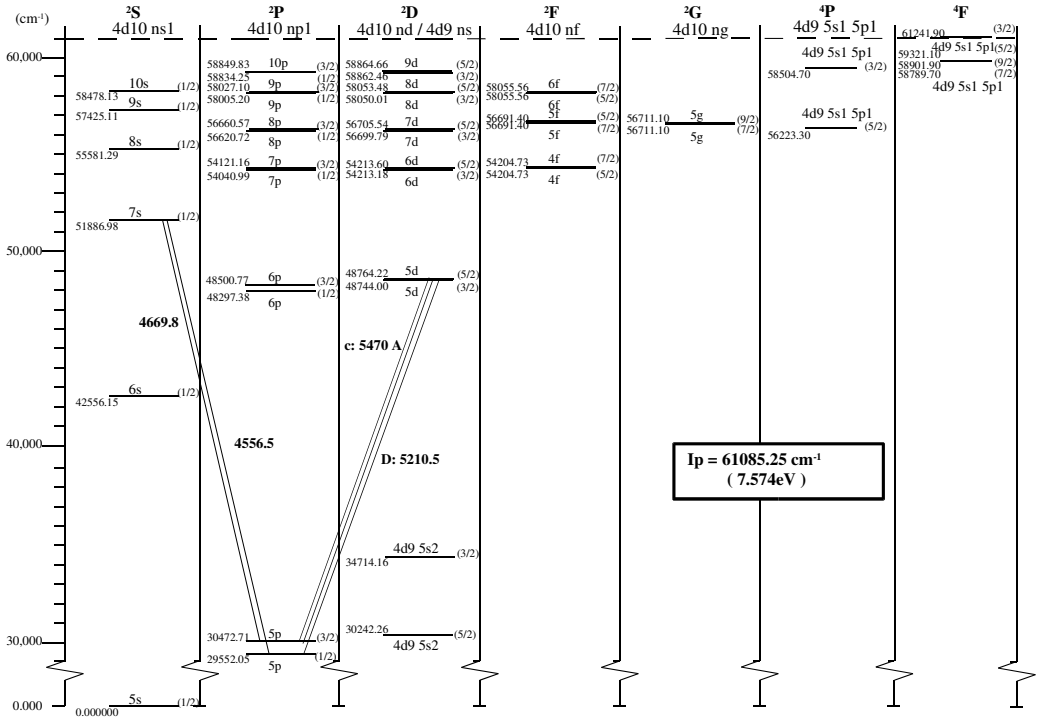

Figure A.2: Ag I Grotrian diagram.

Appendix B

Futher Results from Synthetic Spectra Comparison with Early in Time and Close to the Surface Lineouts

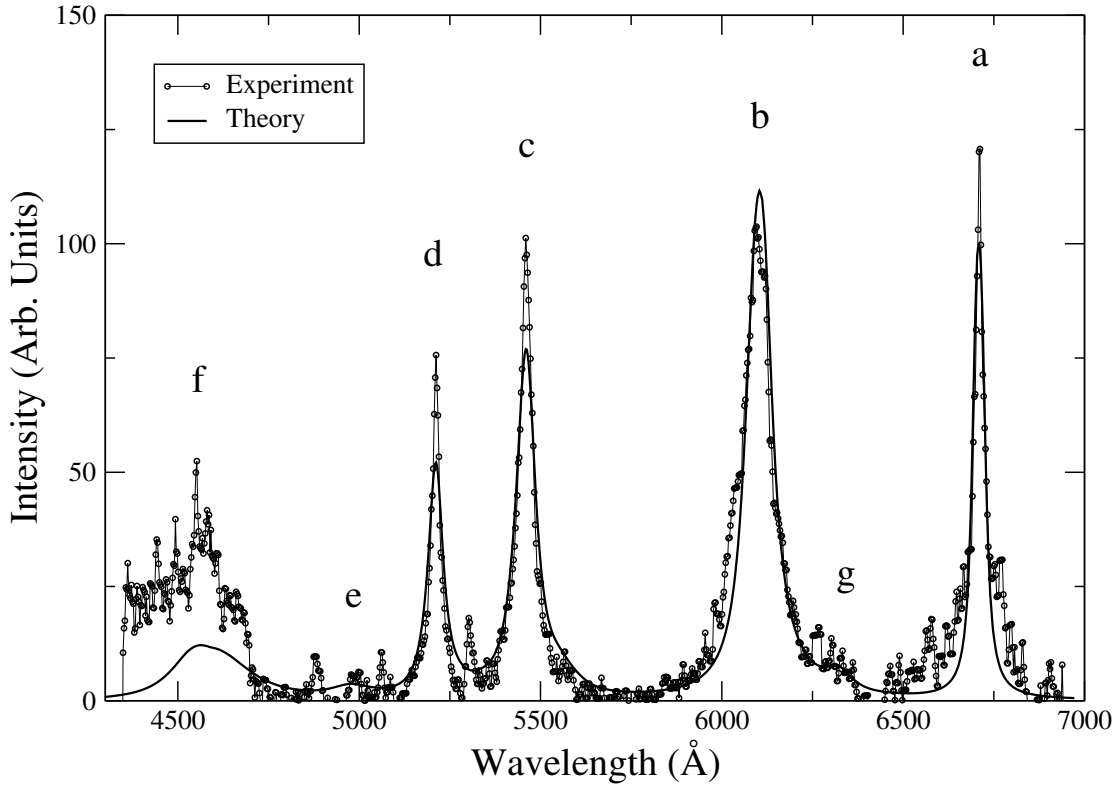

Figure B.1: Experimental lineout at x=86.4μm and t=20 nsec with predicted T_e=1.6 eV and N_a=4.5x10^{17} cm^{-3} uniform synthetic spectra.

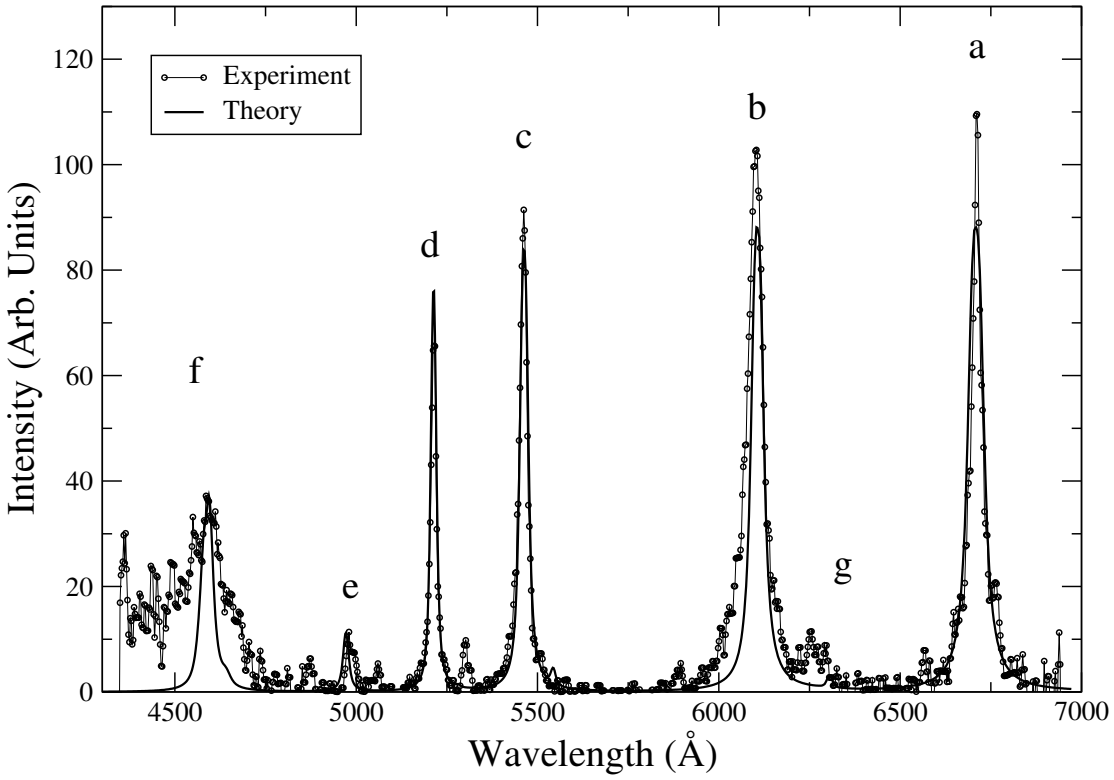

Figure B.2: Experimental lineout at x=86.4μm and t=30 nsec with predicted T_e=0.7 eV and N_a=0.8x10^{17} cm^{-3} uniform synthetic spectra.

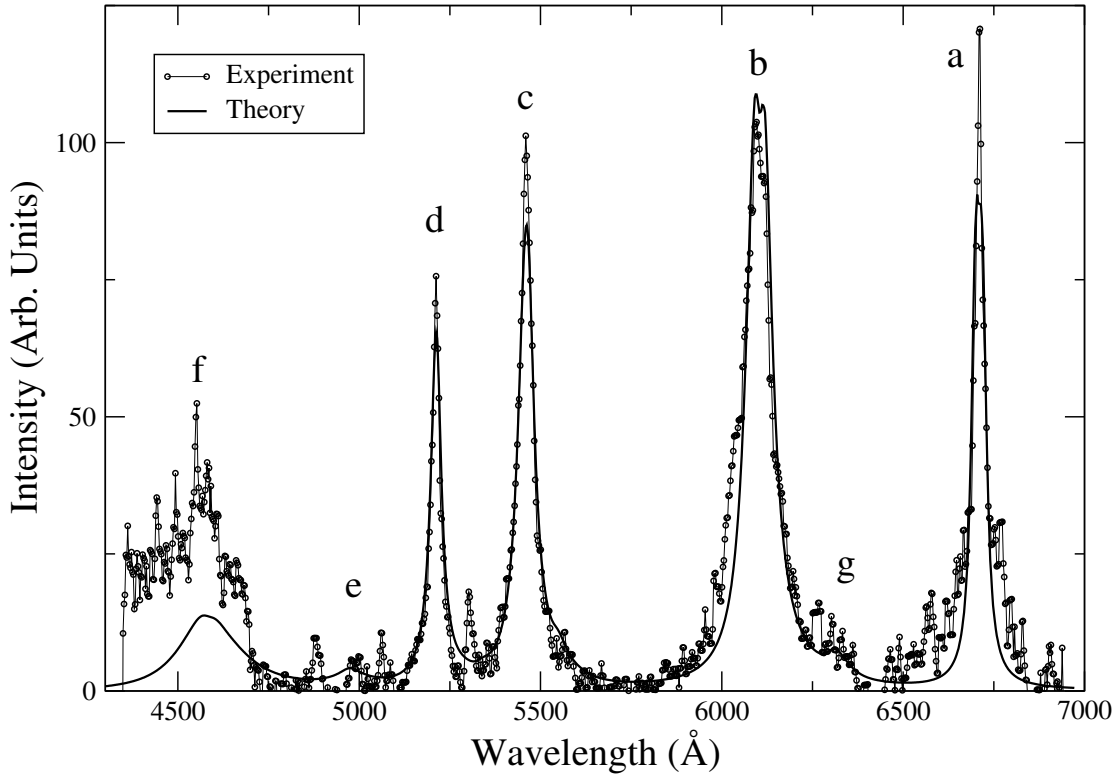

Figure B.3: Experimental lineout at x=86.4μm and t=20 nsec with predicted T_e=[1.2, 1.8, 1.8, 1.2] eV and N_a=[2.5, 5.0, 5.0, 2.5] x10^{17} cm^{-3} 4-zone synthetic spectra.

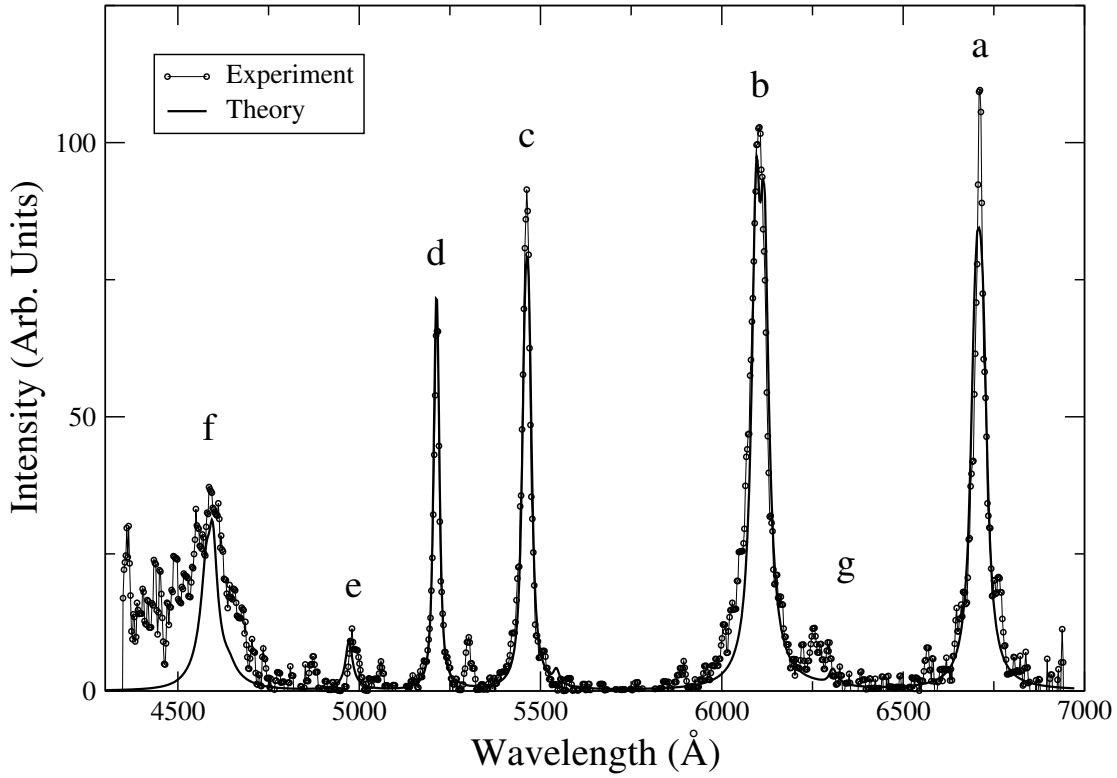

Figure B.4: Experimental lineout at x=86.4μm and t=30 nsec with predicted T_e=[0.7, 1.8, 1.8, 0.7] eV and N_a=[1.0, 1.5, 1.5 , 1.0] x10^{17} cm^{-3} 4-zone synthetic spectra.

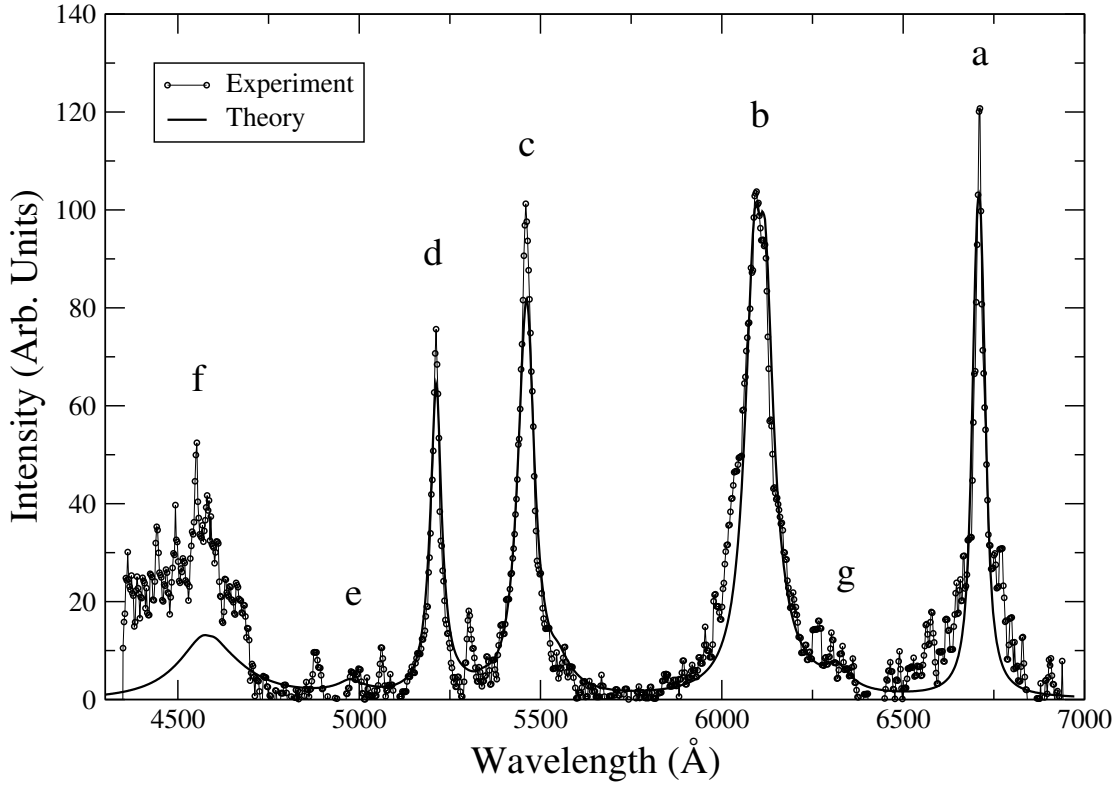

Figure B.5: Experimental lineout at x=86.4μm and t=20 nsec with predicted T_e=[1.2, 1.2, 2.0, 2.0, 1.2, 1.2] eV and N_a=[1.5, 3.5, 6.0, 6.0, 3.5, 1.5] x10^{17} cm^{-3} 6-zone synthetic spectra.

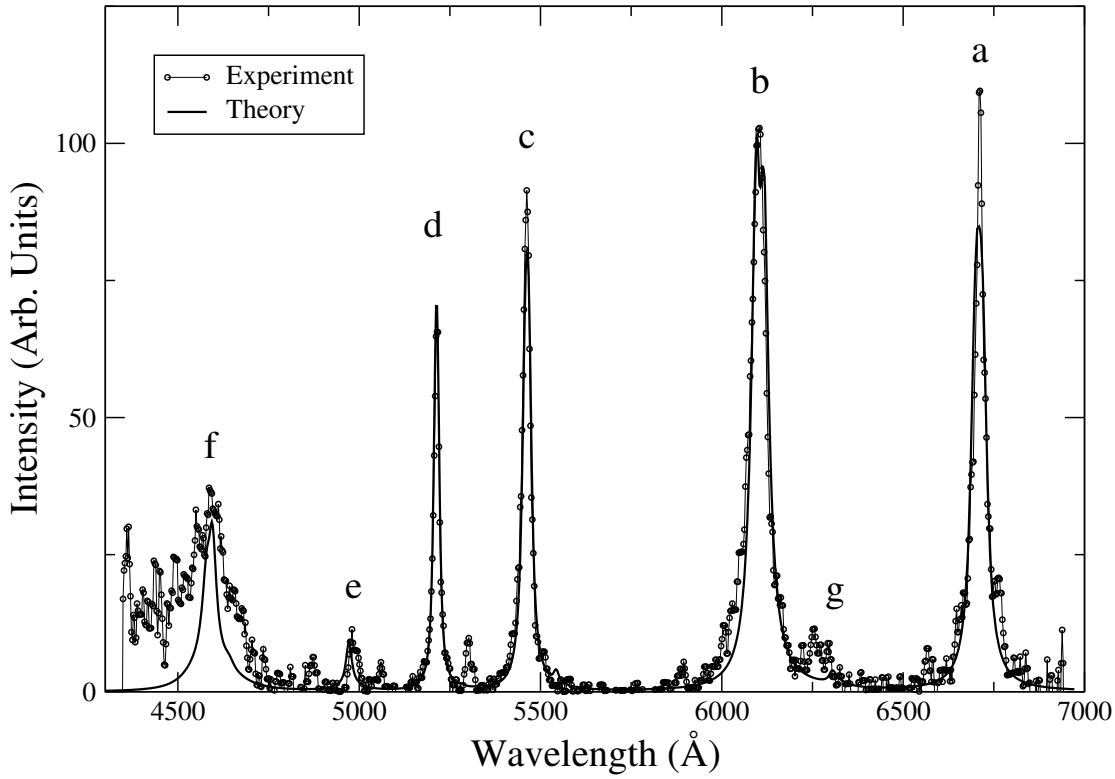

Figure B.6: Experimental lineout at x=86.4μm and t=30 nsec with predicted T_e=[0.7, 0.7, 1.8, 1.8, 0.7, 0.7] eV and N_a=[0.8, 0.8, 2.0, 2.0, 0.8, 0.8] x10^{17} cm^{-3} 6-zone synthetic spectra.

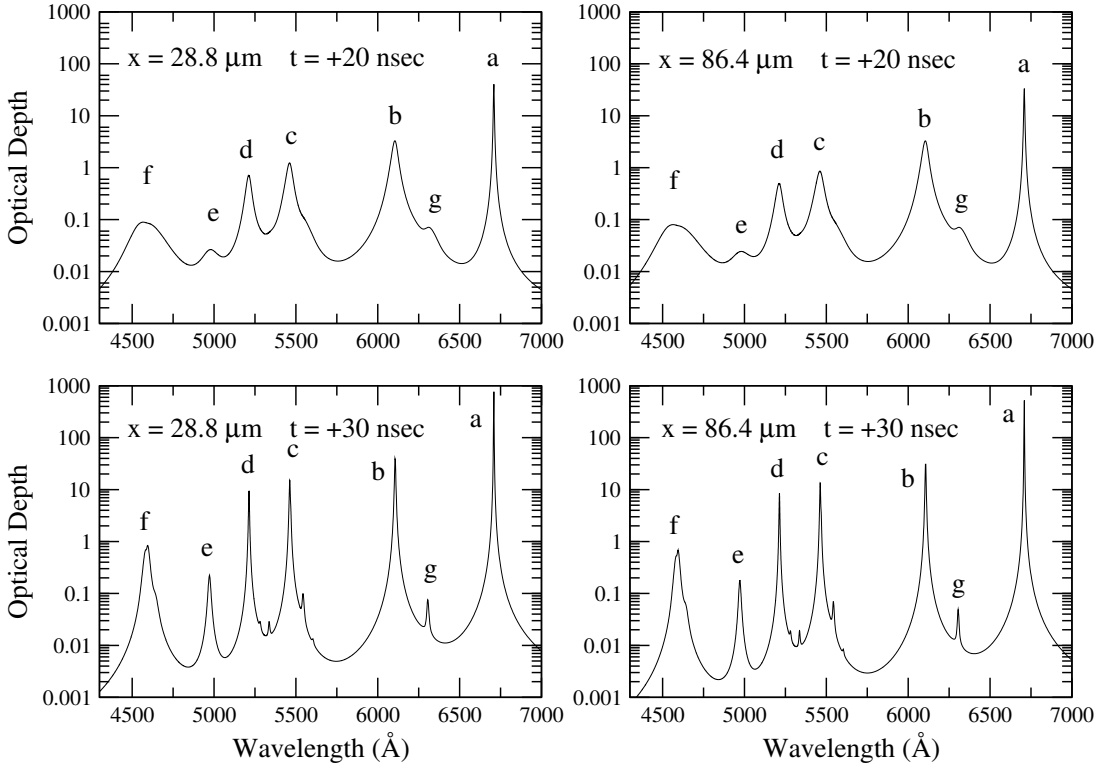

Figure B.7: Optical depth for uniform synthetic spectra.

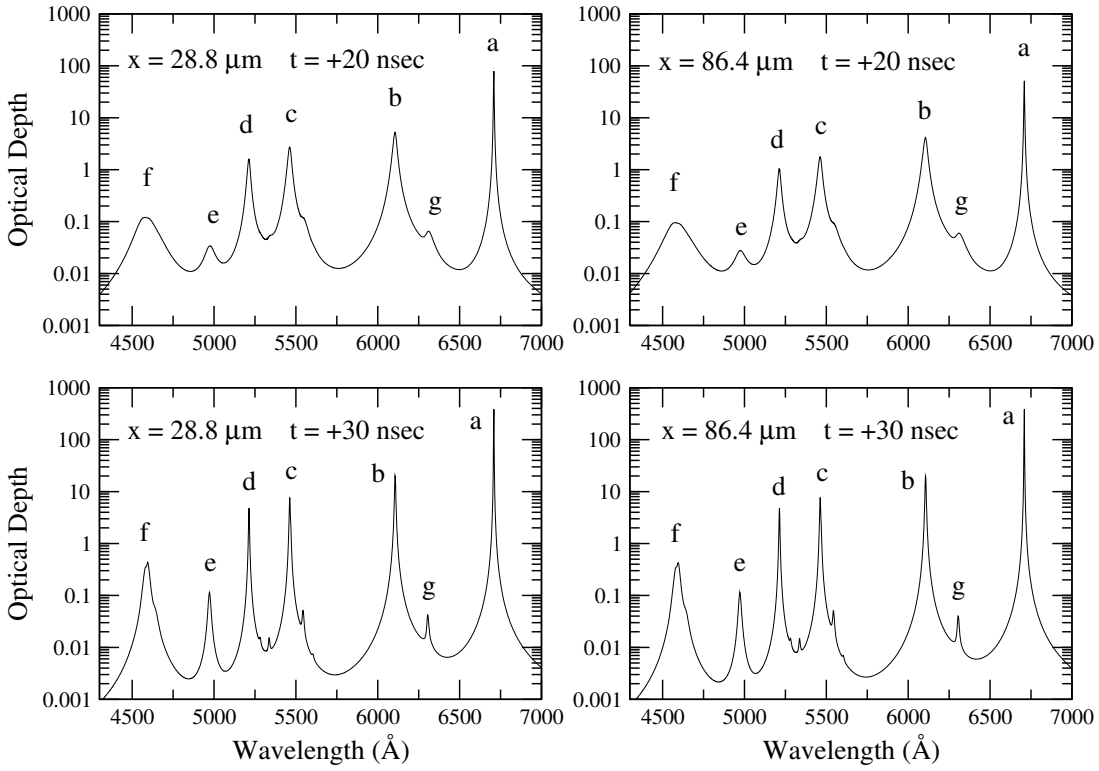

Figure B.8: Optical depth for 4-zone synthetic spectra.

Bibliography

[1] L. J. Radziemski and D. A. Cremers, editors. *Laser-Induced Plasmas and Applications*, pages 1–67. Marcel Dekker, 1989.

[2] D. B. Chrisey and G. K. Hubler. *Pulsed Laser Deposition of Thin Films*. Wiley-Interscience, 1994.

[3] A. A. Puretzky, Geohegan D. B., G. B. Hurst, and M. V. Buchanan. Imaging of vapor plumes produced by matrix assisted laser desorption: A plume sharpening effect. *Phys. Rev. Lett.*, 83:444–447, 1999.

[4] H. M. Smith and A. F. Turner. *J. Appl. Opt.*, 4:147–148, 1965.

[5] D. Dijkkamp and et al. *Appl. Phys. Lett.*, 51:619–621, 1987.

[6] A.A. Puretzky, H. Schittenhelm, Xudong Fan, M.J. Lance, L.F. Allard, and D.B. Geohegan. Investigations of single-wall carbon nanotube growth by time-restricted laser vaporization. *Phys. Rev. B*, 65:245425, 2002.

[7] P. Lorazo, L. J. Lewis, and M. Meunier. Simulation of picosecond pulsed laser ablation of silicon: The molecular-dynamics thermal-annealing model. *Proc. SPIE*, 4276:57–61, 2001.

[8] K. R. Chen, J. N. Leboeuf, R. F. Wood, Geohegan D. B., J. M. Donato, C. L. Liu, and A. A. Puretzky. Accelerated expansion of laser-ablated materials near a solid surface. *Phys. Rev. Lett.*, 75:4706–4709, 1995.

[9] R. F. Wood, K. R. Chen, J. N. Leboeuf, A. A. Puretzky, and D. B. Geohegan. Dynamics of plume propagation and splitting during pulsed-laser ablation. *Phys. Rev. Lett.*, 79(8):1571–1574, 1997.

[10] R. F. Wood, J. N. Leboeuf, A. A. Geohegan D. B., Puretzky, and K. R. Chen. Dynamics of plume propagation and splitting during pulsed-laser ablation of silicon in helium and argon. *Phys. Rev. B*, 58(3):1533–1543, 1998.

[11] R. F. Wood, J. N. Leboeuf, K. R. Chen, Geohegan D. B., and A. A. Puretzky. Dynamics of plume propagation, splitting, and nanoparticle formation during pulsed-laser ablation. *Applied Surface Science.*, 127-129:151–158, 1998.

[12] J. C. Miller and R. F. Haglund, editors. *Laser Ablation and Desorption*, pages 255–289. Academic Press, 1998.

[13] H. R. Griem. Plasma spectroscopy in inertial confinement fusion and soft x-ray laser research. *Phys. Fluids B*, 4(7):2346–2361, 1992. 33rd Annual Meeting of the Division of Plasma Physics of the American Physical Society.

[14] M. J. Herbst, P. G. Burkhalter, J. Grun, R. R. Whitlock, and M. Fink. Spot spectroscopy: Local spectroscopic measurements within laser-produced plasmas. *Rev. Sci. Instrum.*, 53(9):1418–1422, 1982.

[15] C. E. Moore. *Bibliography on the Analysies of Optical Atomic Spectra.* U.S. Natl. Bur. Stand. Special Publ. 306, 1968.

[16] J.C. Pickering and V. Zillio. New accurate data for the spectrum of neutral silver. *Eur. Phys. J. D*, 13:181–185, 2001.

[17] R. D. Cowan. *The Theory of Atomic Structure and Spectra.* University of California Press, 1981.

[18] G. Herzberg. *Atomic Spectra and Atomic Structure.* Dover Publications, 1944.

[19] J. Abdallah Jr., R. E. H. Clark, and R. D. Cowan. *Theoretical Atomic Physics Code Development I CATS: Cowan Atomic Structure Code*, 1988.

[20] R. D. Cowan. *The Theory of Atomic Structure and Spectra*, chapter 3. University of California Press, 1981.

[21] R. D. Cowan. *The Theory of Atomic Structure and Spectra*, chapter 5. University of California Press, 1981.

[22] R. D. Cowan. *The Theory of Atomic Structure and Spectra*, chapter 16. University of California Press, 1981.

[23] R. E. H. Clark, J. Jr. Abdallah, Csanak G., Mann J. B., and R. D. Cowan. *Theoretical Atomic Physics Code Development II ACE: Another Collisional Excitation Code*, 1988.

[24] R.E.H. Clark, D.H. Sampson, and S.J. Goett. Scaled collision strengths for δ n $>$ 1 transitions involving $<$ 5 in hydrogenic ions. *The Astrophysical Journal Supplement Series*, 49:545–554, 1982.

[25] W. H. Press, S. A. Teukolsky, W. T. Vetterling, and B. P. Flannery. *Numerical Recipes in Fortran.* Cambridge University Press, 1992.

[26] R. Epstein. Effects of non-maxwellian electron populations in non-lte simulations of laser-plasma thermal transport and implosion experiments. *J. Quant. Spectrosc. Radiat. Transfer*, 35:131–143, 1986.

[27] H. R. Griem. *Principles of Plasma Spectroscopy*, chapter 6. Cambridge University Press, 1997.

[28] H. R. Griem. *Principles of Plasma Spectroscopy*, chapter 7. Cambridge University Press, 1997.

[29] D. Mihalas. *Stellar Atmospheres*, chapter 5. W. H. Freeman and Company, 1978.

[30] A. Burgess. A general formula for the estimation of dielectronic recombination coefficients in low-density plasmas. *Astrophys. J*, 141:1588, 1965.

[31] Y. P. Raizer. *Soviet Physics Uspehki*, 8:650, 1966.

[32] J. C. Stewart and K. D. Pyatt. Lowering of ionization potentails in plasmas. *Astrophys. J.*, 144:1203–1211, 1966.

[33] R. M. More. *Average Ionization Stage using Thomas-Fermi Atomic Model*, 1981.

[34] R. C. Mancini and C. F. Fontan. Ionization state and bound level populations in hot, dense plasmas. *J. Quant. Spectrosc. Radiat. Transfer*, 34:115–122, 1985.

[35] A. S. Tanenbaum and A. S. Woodhull. *Operating Systems Design and Implementation.* Prentice Hall, 1997.

[36] S. A. Maxwell. *Linux Core Kernel Commentary.* Coriolis, 2001.

[37] D. P. Bovet and M. Cesati. *Understanding the Linux Kernel.* O'Reilly, 2001.

[38] L. A. Woltz and C. F. Jr. Hooper. Calculation of spectral line profiles of multi-electron emitters in plasmas. *Phys. Rev. A*, 38:4766, 1988.

[39] R. C. Mancini, D. P. Kilcrease, L.A. Woltz, and C. F. Jr. Hooper. Calculational aspects of the stark line broadening of multielectron ions in plasmas. *Comp. Phys. Comm.*, 63:314, 1991.

[40] C. A. Iglesias, H. E. DeWitt, J. L. Lebowitz, D. MacGowan, and W. B. Hubbard. Low-frequency electric microfield distributions in plasmas. *Phys. Rev. A*, 31:1698, 1985.

[41] R. J. Tighe and C. F. Jr. Hooper. Low-frequency electric microfield distributions in a plasma containing multiply-charged ions: Extended calculations. *Phys. Rev. A*, 15:1773, 1977.

[42] G. B Arfkin and H. J. Weber. *Mathematical Methods for Physicists.* Academic Press, fourth edition, 1995.

[43] I. E. Golovkin, R. C. Mancini, S. J. Louis, R. W. Lee, and L. Kline. Analysis of x-ray spectral data with genetic algorithms. *J. Quant. Spectrosc. Radiat. Transfer*, 75:625–636, 2002.

[44] H. R. Griem. *Principles of Plasma Spectroscopy*, chapter 4. Cambridge University Press, 1997.

[45] R. C. Mancini and C. F. Hooper, Jr. Hydrodynamics and k-shell radiation emission of laser compressed ar-filled glass microballoons. *J. Phys. D: Appl. Phys.*, 21:1099–1111, 1988.

[46] S. P. Lyon and J. D. Johnson. *Sesame: The Los Alamos National Laboratory Equation of State Database.*, 1992.

[47] S. H. Jeong, R. Greif, and R. E. Russo. Numerical modeling of pulsed laser evaporation of aluminum targes. *Applied Surface Science*, 127-129:177–129, 1997.

[48] L.A. Doyle, G.W. Martin, A. Al-Khateeb, I. Weaver, D. Diley, M.J. Lamb, T. Morrow, and C.L.S. Lewis. Electron number density measurements in magnesium laser prodiced plumes. *Appl. Surf. Sci.*, 127-129:716–720, 1998.

[49] S. Bashkin and J. Stoner. *Atomic Energy Levels and Grotrian Diagrams.* North-Holland Pub. Co., 1975.